

**LITHOSPHERIC DYNAMICS OF MARS:  
WATER, FLOW, AND FAILURE**

NASA PLANETARY GEOLOGY AND GEOPHYSICS PROGRAM

**NAG5-9491**

**FINAL REPORT**

For the period  
April 15, 2000 to December 31, 2003

January 6, 2004

Robert E. Grimm\*, Principal Investigator  
Laboratory for Atmospheric and Space Physics  
University of Colorado  
Boulder, CO

CU Project #1532662

\*Now At:  
Southwest Research Institute  
Boulder, CO  
grimm@boulder.swri.edu

## ABSTRACT

Some of the largest Martian erosive features were influenced by groundwater, and include valley networks, outflow channels, and possibly landslides.

We argue that hydrothermal systems attending crustal formation processes were able to drive sufficient groundwater to the surface to form the Noachian southern highlands valley networks, which show a spatial correlation to crustal magnetic anomalies, also results of crustal formation. Hydrothermal activity is quantified through numerical simulations of convection in a porous medium due to the presence of a hot intruded magma chamber. The parameter space includes magma chamber depth, volume, aspect ratio, and host rock permeability and porosity. For permeabilities as low as  $10^{-17} \text{ m}^2$  and intrusion volumes as low as  $50 \text{ km}^3$ , the total discharge due to intrusions building that part of the southern highlands crust associated with magnetic anomalies spans a comparable range as the inferred discharge from the overlying valley networks.

The Hesperian circum-Chryse outflow channels are further manifestations of groundwater discharge and Clifford and Parker (2001) suggest that the large volumes of water required for their formation flows beneath a confining cryosphere from the South Pole where meltwater beneath an ice cap recharges a global aquifer. We argue that recharge occurs instead over the nearby Tharsis aquifer at high obliquity, assisted by cryosphere melting due to volcanic activity. Numerical simulations quantify the strength and duration of outflow discharge given either South Polar or Tharsis recharge. The contribution of South Pole recharge given Clifford and Parker (2001) aquifer properties is negligible compared to that of the initial Tharsis inventory. Tharsis recharge, despite the restrictions of improved aquifer properties, makes a significant contribution and, unlike South Pole recharge under the same conditions, fulfills discharge requirements.

Groundwater may have influenced long run-out landslide formation in the Valles Marineris. We present simulations of Martian, terrestrial, and lunar landslides that gauge the role of pore fluid pressure in reproducing accurate geometries and run-out with frictional, Bingham, and fluidization rheologies. The results indicate that pore fluid is a necessary component of Martian landslide formation and we suggest scenarios that might explain its presence.

This report is the Ph.D. Thesis of Keith Harrison, who performed the work under the supervision of the PI, Dr. Robert Grimm.

## CONTENTS

CHAPTER		
1.	INTRODUCTION	1
	1.1 Observational History of Water on Mars	1
	1.2 Valley Networks	2
	1.3 Long Runout Landslides	2
	1.4 Outflow channels	3
	1.5 Tharsis	3
2.	HYDROTHERMAL SYSTEMS AND VALLEY NETWORKS	5
	2.1 Introduction	5
	2.2 Model	6
	2.3 Results	10
	2.3.1 Permeability	12
	2.3.2 Volume	17
	2.3.3 Depth	18
	2.3.4 Aspect Ratio	20
	2.3.5 Geothermal Gradient	21
	2.3.6 Ice	22
	2.3.7 Water Table	24
	2.4 Discussion	25
	2.4.1 Implications for Hydrothermal Circulation	25
	2.4.2 Relationship of Hydrothermal Circulation to Valley Networks and Magnetic Anomalies	28

	2.4.3	Conclusions	35
3.		LONG RUNOUT LANDSLIDES	37
	3.1	Introduction	37
	3.2	Model	39
	3.2.1	Numerical Simulations	39
	3.2.2	Landslide Geometry	44
	3.3	Results	48
	3.4	Discussion and Conclusions	66
	3.4.1	Best Overall Rheology	66
	3.4.2	Other Rheologies	70
	3.4.3	Gravity Effects	71
4.		OUTFLOW CHANNELS	75
	4.1	Introduction	75
	4.2	Model	79
	4.2.1	MODFLOW-2000	79
	4.2.2	Boundary Conditions	81
	4.2.3	Recharge and Thermal Properties	86
	4.3	Results	88
	4.3.1	Nominal South Pole Recharge Model	88
	4.3.2	Tharsis Recharge Model	94
	4.3.3	Alternative South Pole Recharge Model	95
	4.4	Discussion	100
	4.4.1	Problematic aspects of the Nominal South Pole Recharge Model	100
	4.4.2	Tharsis Recharge: Ice Sheet with Basal Melting	101

4.4.3	Tharsis Recharge: Local Cryosphere Melting	102
4.4.4	Other Outflow Channels	103
4.5	Conclusions	104
5.	CONCLUSIONS	106
5.1	Valley Networks	106
5.2	Long Runout Landslides	107
5.3	Outflow Channels	107
5.4	Historical Relationship Between Landforms and Environment	108
5.5	Future Improvements	111
	BIBLIOGRAPHY	112

## TABLES

Table		
2.1	Water/rock ratios (by mass) calculated for 8.5 km deep chambers of the indicated volumes and host rock permeabilities.	26
2.2	Statistical data for the correlation between valley networks and magnetic anomalies.	30
3.1	Landslide deposit dimensions.	47
3.2	Information inferred from vertical cross-sections.	48
3.3	Summary of DAN results.	53
4.1	Outflow sources used in MODFLOW models, and their associated valleys, with the approximate volume of material removed from each.	83

## FIGURES

Figure		
2.1	Surface discharge from the baseline model.	11
2.2	Effect of host rock permeability on discharge.	13
2.3	Discharge results from HYDROTHERM models of a similar geometry to those of Gulick (1998).	15
2.4	Effect of magma chamber volume on discharge.	16
2.5	Effect of magma chamber depth on discharge.	18
2.6	Summary of depth and permeability results.	19
2.7	Effect of magma chamber aspect ratio on discharge.	20
2.8	Effect of host rock ice on discharge.	23
2.9	Effect of water table on discharge.	25
2.10	Overlay of crustal magnetic anomalies and valley networks.	28
2.11	Summary of results.	34
3.1	Conceptual model of initial landslide shape.	45
3.2	Images of landslides modeled.	49
3.3	DAN results for Slide 1.	52
3.4	DAN results for Slide 2.	55
3.5	DAN results for Slide 3.	56
3.6	MOC images of Slide 4.	57
3.7	DAN results for Slide 4.	58
3.8	DAN results for Slide 5.	60
3.9	DAN results for Slide 6.	61

3.10	DAN results for Slide 7.	62
3.11	DAN results for Slide 8.	63
3.12	DAN results for Slide 9.	64
3.13	Observed trends in ratio $H / L_f$ vs. $V$ .	72
4.1	Model topography with recharge area and outflow sources.	85
4.2	Latitudinal dependence of cryosphere thickness for different hydrologic and thermal conditions.	87
4.3	Instantaneous discharges from model 1.	89
4.4	Hydraulic head distribution at 400 Myr in models 1 and 2.	90
4.5	Scaling of permeability, sediment-water ratio, and outflow activity duration.	92
4.6	Instantaneous discharges from model 2.	93
4.7	Variations in infiltration rate with area.	97
4.8	Instantaneous discharges from model 3.	98
4.9	Aquifer thickness determined by various porosities.	99
5.1	Timing of landform development with crustal heat fluxes and equatorial cryosphere thicknesses.	109

## CHAPTER 1

### INTRODUCTION

#### **1.1 Observational History of Water on Mars**

Introduction of the specific landforms studied in this work is best begun with a brief overview of the observational history of water on Mars. The first discovery of its presence was through ground-based, infra-red detection of atmospheric water vapor in 1963 (Spinrad *et al.*). Disappointing prospects for surface water followed two years later with dry, lunar-like images photographed from Mars orbit by Mariner 4, followed by much the same from subsequent Mariner 6 and 7 craft (Leighton *et al.*, 1965; Leighton *et al.*, 1969; Collins, 1971). Only with images from the first Mars orbiter (Mariner 9), and in the late 1970's with Viking, were fluvial landforms first observed, and more detailed questions concerning surface and groundwater raised. The Mars Global Surveyor Mission (1997 to the present), with its global capture of high-resolution photographic and topographic data, has not only improved our understanding of landforms discovered by Viking, but has brought to light another set of smaller, more subtle water-related features, including the geologically young spur-and-gully formations (Malin and Edgett, 2000). Finally, over the last two years, the Mars 2001 Odyssey Mission has detected (with its Gamma Ray Spectrometer) significant quantities of ice in the mid- to high-latitude regolith (Boynton *et al.*, 2002). Our initial impression of Mars as a dry, lunar-like planet has evolved to one of an environment affected over most of its history by the action of water. In particular, crustal groundwater has played an important erosive role, and We address questions regarding three of its manifestations: valley networks, landslides, and outflow

channels, which we now introduce individually in the order they appear in later chapters.

### **1.2 Valley Networks**

The valley networks are the most common drainage feature on Mars. Distributed mostly on ancient Southern Highlands terrain within  $65^\circ$  of the equator and at all longitudes, they embody the strongest evidence that a warm climate conducive to globally distributed flow of surface water once existed on Mars. Groundwater sapping is the predominant process responsible for valley network formation (favored over precipitation; Baker, 1992; and references therein) and gives rise to long, narrow “U” shaped valleys that often follow zones of weakness, such as fault lines. While local patterns of groundwater flow leading to sapping are fairly well understood (Dunne, 1980), it is not clear how Martian valleys were supplied with the necessary water, a question we address in this work.

### **1.3 Long Runout Landslides**

The Valles Marineris make up a 4000 km long system of equatorial grabens that appear to have formed in response to tectonic forces in the nearby Tharsis rise (Blasius *et al.*, 1977), although recent work suggests the influence of local volcanic intrusions (McKenzie and Nimmo, 1998). Failure of the canyon wall rock has produced numerous landslide events, the largest of which have left runout deposits on the canyon floor up to 80 km long. Long run-outs are not predicted by models of simple frictional sliding and on the earth usually involve the action of water pressure in the pore spaces of the failed material. The presence of groundwater in the Valles Marineris slides was first suggested by Lucchitta (1987), and agrees with evidence of water-related processes in the formation of other Valles Marineris landforms, such as

the interior layered deposits (e.g. McCauley, 1978; Nedell *et al.*, 1987). In this work, we attempt to constrain the requirements on pore fluid pressure in Martian long run-out landslide formation.

#### **1.4 Outflow channels**

While the valley networks reveal information concerning the global distribution of Noachian surface water on Mars, the outflow channels provide insight into the volume of the global water inventory later in Martian history, during the Hesperian. These large channels, unlike the valley networks, have distinct bedforms indicative of water flow (Mars Channel Working Group, 1983) and experienced higher, probably catastrophic, flow rates (Baker and Milton, 1974). They are thought to have expelled at least  $6 \times 10^6 \text{ km}^3$  of water into the low-lying northern plains (Carr, 1996). This water came from the crustal aquifer, probably reaching the surface through a disruption in an overlying icy permafrost zone, but details of the necessarily distal sourcing of such large quantities of water remain unanswered. Clifford and Parker (2001) put forward a sophisticated model involving sublimation from a northern lowlands ocean, deposition and accumulation of a South Polar ice cap, and the charging of a global aquifer by water melted at its base. we suggest an alternative, regional method of aquifer recharge through nearby high elevation Tharsis during periods of high planetary obliquity.

#### **1.5 Tharsis**

Valley networks, long run-out landslides, and outflow channels are related through the influence of the Tharsis rise. Trends in valley network orientation contribute to the recent consensus that Tharsis formed during the Noachian (Phillips *et al.*, 2001; Anderson *et al.*, 2001). The volcanically active nature of its

development suggests a strong effect on climate (Jakosky and Phillips, 2001), changing global surface stability and atmospheric content of water and therefore the conditions under which valley network erosion took place. The location, morphology, and orientation of the Valles Marineris suggest a strong correlation to tectonic forces (Blasius *et al.*, 1977) in Tharsis that may have been responsible for triggering landslides (Caruso, 2003). Likewise, Tharsis influenced the outflow channels, possibly disrupting the cryosphere with thermal perturbations, and providing water in necessary quantities with the required hydraulic head.

## CHAPTER 2

### HYDROTHERMAL SYSTEMS AND VALLEY NETWORKS – NOACHIAN GROUNDWATER FLOW

#### 2.1 Introduction

Valley networks in the ancient terrain of the Martian Southern Highlands represent some of the oldest and most widespread evidence of water-related erosional processes on Mars. They occur at most longitudes and at low to mid-latitudes, and their time of formation is mostly Noachian, suggesting that the early Martian climate might have been warm enough to ensure the stability of surface water. The morphology of some valleys indicates that they were fed by groundwater discharge (see Baker *et al.*, 1992, Baker, 2001, and Carr, 1996, for reviews; Malin and Carr, 1999; Malin and Edgett, 2000). A question that follows naturally from this discovery is what drove groundwater to the surface, especially on the large spatial scale observed. Hydrothermal activity may have played a primary role here.

Hydrothermal systems are important providers of energy in many terrestrial igneous, metamorphic, and sedimentary environments, and have profound geochemical and biological implications. They accelerate the cooling of magmatic bodies in systems ranging from divergent plate boundaries to individual volcanoes, and commonly produce substantial surface discharge of water and steam in the form of hot springs, geysers, and submarine vents (black smokers).

On Mars, evidence remains of past hydrothermal activity (see Farmer (1996), for a review). Wilhelms and Baldwin (1989) note the widespread presence of ancient volcanic structures in the southern highlands, as suggested by outcrop structures along the global crustal dichotomy and in crater floors and other depressions. Fluvial

channels are frequently associated with volcanic activity (Brakenridge, 1990; Baker *et al.*, 1992) and associated structures that include (but are not limited to) ancient volcanoes (Gulick, 1998). Hydrothermal circulation may also have altered the martian crust and further produced weathering products and soil (Griffith and Shock, 1997; Newsom *et al.*, 1999). The greatest consequence of hydrothermal activity on Mars may be its ability to sustain life (Shock, 1996; Farmer, 1996).

we present here numerical models of the thermal convection of groundwater in a porous host rock due to the presence of an intruded magma chamber. An extensive portion of the available parameter space is explored in order to quantify the effects that magma chamber volume, depth, aspect ratio, host rock permeability and porosity have on surface discharge. The results of this general approach are then applied to some specific issues. First, we use geochemical constraints to bound the permeability of the martian crust. Second, we test the hypothesis that hydrothermal circulation can explain the putative correlation observed between valley networks and magnetic anomalies (Jakosky and Phillips, 2001). we suggest that large amounts of water were circulated throughout the southern-highlands crust due to magmatic intrusion and that the portion of this water discharged to the surface can quantitatively account for the valley networks preserved since the end of crustal formation.

## 2.2 Model

Two-dimensional, axisymmetric representations of hydrothermal circulation in a magma chamber and its host rock are modeled with the USGS code HYDROTHERM (Hayba and Ingebritsen, 1994, 1997) and visualized with the help of its graphical user interface HTpost (P. S. Hsieh, USGS, unpublished material, 2000). HYDROTHERM can model temperatures from about 0 to 1200 °C and pressures from 0.5 to 10,000 bars, and keeps track of both liquid and gaseous phases of pure water. It solves mass,

momentum, and energy balance equations expressed in terms of dependent variables pressure and enthalpy. The choice of enthalpy over temperature allows the thermodynamic state of the fluid to be specified uniquely under two-phase conditions. In some circumstances, the combination of pressure and enthalpy is supercritical. The resulting fluid, which technically is neither a liquid nor a gas, is treated by HYDROTHERM as an equal mixture of each. In my models, supercritical conditions are found almost exclusively within the magma chamber, which at these high temperatures is ductile and thus impermeable, obviating the need for a detailed model of supercritical flow. Viscosity and density for a particular temperature and pressure (in any phase) are obtained from a look-up table.

The momentum balance equation is Darcy's Law, which for a single fluid phase  $i$  is

$$\mathbf{v}_i = -\frac{k_{rel}^i k}{\mu_i} (\nabla p + \rho_i g \nabla z) \quad (2.1)$$

where  $\mathbf{v}_i$  is the Darcy velocity,  $k$  is intrinsic permeability,  $\mu_i$  is dynamic viscosity,  $p$  is pressure,  $\rho_i$  is density,  $g$  is gravitational acceleration, and  $z$  is depth. The relative permeability  $k_{rel}^i$  quantifies the reduction of the flow of phase  $i$  due to the presence of the other phase. The mass-balance (continuity) equation for phase  $i$  is:

$$\frac{\partial}{\partial t} (n S_i \rho_i) + \nabla \cdot (\rho_i \mathbf{v}_i) = 0. \quad (2.2)$$

where  $n$  is porosity,  $t$  is time, and  $S_i$  is volumetric saturation ( $S_{water} + S_{steam} = 1$ , i.e. the medium is fully saturated). The continuity equation for the entire system is the sum of the equations for each phase. The energy-balance equation for the entire system is

$$\frac{\partial}{\partial t} \left[ (1-n)\rho_r h_r + n \sum_i S_i \rho_i h_i \right] + \nabla \cdot \left[ \sum_i k_n \rho_i h_i \mathbf{v}_i \right] - \nabla \cdot K_m \nabla T = 0 \quad (2.3)$$

where  $h$  is enthalpy,  $T$  is temperature,  $K_m$  is medium thermal conductivity, and subscript  $r$  refers to rock matrix properties. HYDROTHERM solves the equations by performing Newton-Raphson iterations on an equivalent finite difference system (with the horizontal dimension expressed in radial coordinates) until mass and energy residuals fall below specified maximum values.

The radial extent of the host rock is 20 times that of the magma chamber and the vertical extent is 20 km, both of which are sufficient to accommodate flow from all magma chambers studied. Fluid is allowed to cross the upper horizontal and right vertical boundaries, while temperature and pressure are fixed. The right vertical boundary is not intended to represent the limit of a horizontally bounded water source, but to provide enough space for a realistic response to a local temperature perturbation. As much fluid flows through this boundary as is necessary to balance the net flow through the top horizontal boundary. The suitability of the chosen radial extent was tested by a baseline model measuring 40 chamber radii across, which yielded almost the identical discharge to the original model. Recharge into the model is typically less than 10% of discharge, indicating that the strength of discharge is not offset significantly by infiltration of runoff. Adaptive boundary conditions preventing infiltration for a dry Mars could therefore be neglected.

The initial pressure distribution is hydrostatic, with a surface value of 1 bar. A small geothermal gradient (0.5 °C/km), applied to ensure stable decay of the surface discharge, does not otherwise affect the model (the effects of substantial geothermal gradients were explored and the results are described below). Numerically stable

solutions in this model were possible only with temperatures above 10 °C, and this was used for the surface boundary condition. Both the surface temperature and pressure were adopted for numerical convenience and do not affect the results, which are determined almost exclusively by hydrothermal driving forces, nor are they intended to represent Earth-like climatic conditions. The left vertical and lower horizontal boundaries are no-flow, and the temperature and pressure are free to vary. Grid spacing is approximately 100 m in both directions near the magma chamber and at greater horizontal distances increases logarithmically.

Present martian conditions may include a permafrost layer which must first be melted before discharge is produced. Gulick (1998) estimated that the time required to melt a 2 km thick layer of permafrost was much less than the lifetime of the hydrothermal system, making it unlikely that quantities integrated over the lifetime of the system, such as total discharge, should be significantly altered. During the late Noachian, when the hydrothermal systems proposed here were active, the permafrost layer was likely to be much thinner than 2 km, making melting times even shorter. A HYDROTHERM simulation that quantifies the role of ice in our models is described below. A more detailed explanation of cryosphere growth in the Hesperian appears in the second main section of this work (Chapter 3).

Our baseline model contains a 50 km<sup>3</sup> chamber emplaced at a depth of 2 km below the surface, into host rock of permeability 10<sup>-16</sup> m<sup>2</sup>. The dimensions of the chamber are most usefully expressed in terms of its aspect ratio, defined here as the ratio of diameter to height ( $D/H$ ), which in the baseline model has a value of 2. The volume of the chamber is taken after that modeled by Hayba and Ingebritsen (1997) and is of a similar size to magma chambers found under mid-oceanic ridges (Burnett *et al.*, 1989). Note that our baseline model is intended only as an example model

from which we later deviate extensively, and does not necessarily represent any sort of “ideal” martian parameter values.

The magma chamber is emplaced instantaneously at a temperature of 900 °C. Because this approach ignores discharge produced during the finite intrusion process and subsequent supersolidus cooling, it produces relatively conservative results. The chamber is initially impermeable, but as it cools through a brittle-ductile transition (BDT) between 400 °C and 360 °C, it is assumed to fracture and become as permeable as the surrounding host rock (Hayba and Ingebritsen, 1997). A semilog form is adopted for this transition, wherein the log of the permeability scales linearly with temperature. Note that the “permeability” BDT may differ somewhat from the classic “deformational” BDT (e.g., Kohlstedt *et al.*, 1995) brought on by overburden pressure. All models use a rock density of 2500 kg.m<sup>-3</sup>, a thermal conductivity of 2.0 W.m<sup>-1</sup>.K<sup>-1</sup>, and a porosity of 1%. Deviations from the baseline model include host rock permeabilities of 10<sup>-17</sup> and 10<sup>-15</sup> m<sup>2</sup>, a porosity of 25%, magma chamber aspect ratios of 0.2 and 20, depths of 8.5 and 15 km, and volumes of 100 and 2000 km<sup>3</sup>.

Steam and water fluxes, while fundamental to discharge calculations, may also be used to test hypotheses regarding the possible geochemical alteration in the system. For each time step, a measure of water-to-rock ratio for reactions above a particular temperature threshold may be calculated by measuring the total mass of water that passes through the region warmer than the threshold value, and dividing by the volume of the region.

### 2.3 Results

In the baseline model (Figure 2.1) an initial peak in the surface discharge occurring a few hundred years following magma emplacement is due to thermal pressurization (Delaney, 1982). Its peak value is not significantly greater than

discharges that occur later in the model, and the short-lived nature of this effect, which is less extreme for higher host rock permeabilities, contributes negligibly to the total, time-integrated mass of water produced by the system (total discharge), which we assume to be of primary importance in valley erosion. Additionally, thermal pressurization may be weaker in the more realistic case of a finite duration intrusion process.

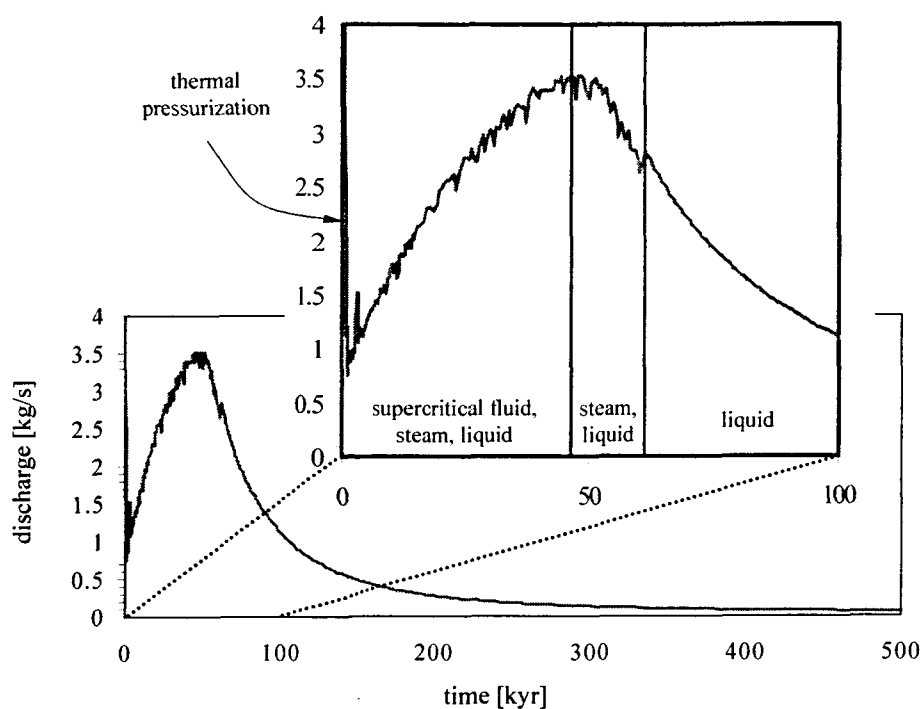


**Figure 2.1** Surface discharge from the baseline model (magma chamber depth 2 km, volume 50 km<sup>3</sup>, aspect ratio 2, host rock permeability  $10^{-16}$  m<sup>2</sup>). The regions separated by solid vertical lines in the enlarged portion of the figure denote the different phases present within in the model. The magma chamber becomes permeable over the interval 0.7 to 57 kyr. The noise on the curve is due mainly to discretization effects in the presence of steam, which has much greater velocity than the liquid phase.

The broad peak at 45 kyr (1 ky = 1,000 yr) is due to thermal convection of groundwater. At first, the chamber is supercritical and impermeable, allowing

convection in the surrounding host rock only. Surface discharge peaks when the magma chamber has cooled sufficiently to become permeable and admit advection. When only the liquid phase remains, discharge becomes smoother, decaying exponentially and ceasing at 2.8 Myr.

### 2.3.1 Permeability

For simplicity, permeability was homogeneous in all models. Gulick (1998) used a value of  $10^{-11} \text{ m}^2$  for martian hydrothermal systems in analogy with young, near-surface Hawaiian volcanics. However, Ingebritsen and Sanford (1998) report that permeabilities in the east rift zone at Kilauea, while high near the surface ( $10^{-10}$  to  $10^{-9} \text{ m}^2$ ), are much lower at depths of just 1 to 2 km ( $10^{-16}$  to  $10^{-15} \text{ m}^2$ ) in rock of the same composition. Manning and Ingebritsen (1999) estimate values of between  $10^{-17}$  and  $10^{-14} \text{ m}^2$  for the mean continental permeability between 1 and 10 km depth, and we therefore use values from  $10^{-17}$  to  $10^{-15} \text{ m}^2$  (Figure 2.2). The upper limit is for computational convenience; we demonstrate below that results for higher permeabilities can be extrapolated from this range. In simulations involving outflow channels (Chapter 3) we exploit the full depth dependence of the Manning and Ingebritsen (1999) permeability since the flow in these models responds to more subtle topographic driving forces.

Discharge from the low ( $10^{-17} \text{ m}^2$ ) permeability model has a characteristically large thermal pressurization peak followed by a weak main peak. Conduction is the dominant mode of heat transfer in this model and the spatially integrated surface discharge at any given time (instantaneous discharge) is approximately a tenth that of the baseline model. While convection is dominant in the high ( $10^{-15} \text{ m}^2$ ) permeability model, convection and conduction play comparative roles in the baseline model. Discharge in all three models lasts between 2.5 and 3.0 Myr, but the rate of decay is,

in general, proportional to permeability, with the  $10^{-17} \text{ m}^2$  model falling to a tenth of its peak value in 0.20 Myr, the baseline model in 0.18 Myr, and the  $10^{-15} \text{ m}^2$  model in 0.14 Myr.

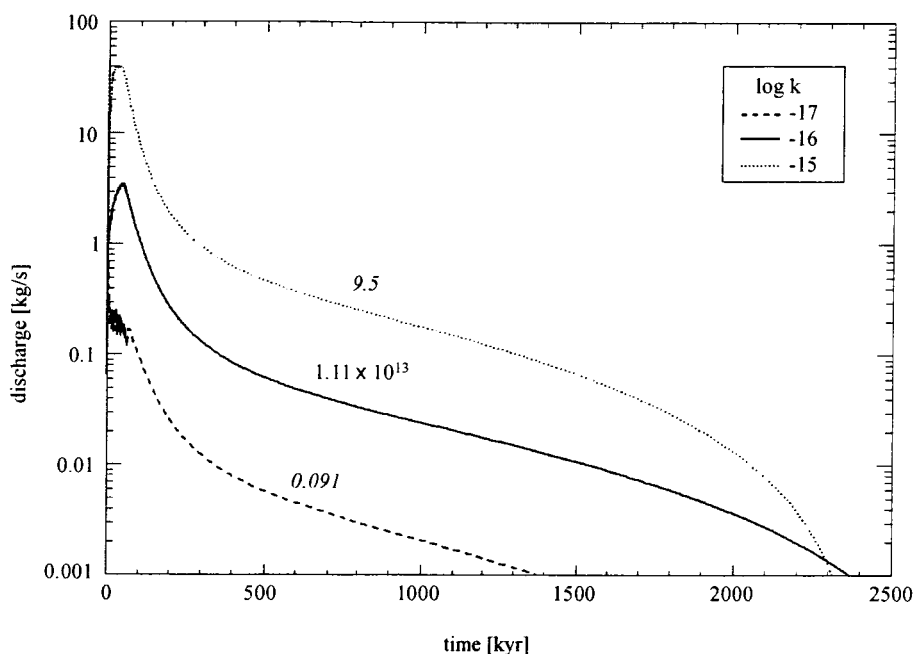


**Figure 2.2** Surface discharge from a 2 km deep magma chamber of volume  $50 \text{ km}^3$  for host rock permeabilities of  $10^{-17}$ ,  $10^{-16}$ , and  $10^{-15} \text{ m}^2$ . The total discharge of the  $k = 10^{-16} \text{ m}^2$  model, in kg, appears above its curve. The numbers above the other curves denote the fraction of this discharge that their corresponding models produced.

An important feature of the high permeability model is the presence of a steam-dominated zone above the magma chamber during the first several thousand years. This phenomenon may have implications for chemical alteration, as described below.

The relationship between discharge and permeability was investigated using the high permeability results of Gulick (1998) as a starting point. She modeled a  $10^{-11} \text{ m}^2$  hydrothermal system which included the magma chamber implicitly through a heat flux boundary condition based on the analytical solution to the conductive heat flow through the wall of an infinitely long cylinder. Consequently, heat loss through the

roof and floor of the chamber was not simulated, and no BDT was encountered on cooling. Adopting these limitations in HYDROTHERM by removing the host rock above and below the magma chamber affords direct comparison with the results of Gulick (1998), including her high permeabilities (Figure 2.3) which are more easily simulated with this simplified geometry. Agreement is good, although small differences result due to our more realistic magma chamber heat flux, and possibly other factors such as numerical solution. Overall, we find that the relationship between total discharge and permeability can be represented approximately by

$$D = a - be^{-cK} \quad (2.4)$$

where  $D$  and  $K$  are the base 10 logarithms of total discharge and permeability respectively, and  $a$ ,  $b$ , and  $c$  are positive constants (with best-fit values of 38, 0.089, and 0.12 respectively). As permeability increases, discharge approaches asymptotically a maximum value of  $a$ , a trend explained by the fixed initial supply of heat in the magma chamber of which a growing, yet ultimately limited fraction energizes groundwater convection. For the range of permeabilities covered with our own, more complete geometry,  $D$  is approximately linear in  $K$ . Note that the total discharges (whose relative magnitudes are given above each non-baseline model curve in Figure 2.2) reflect this linear behavior.

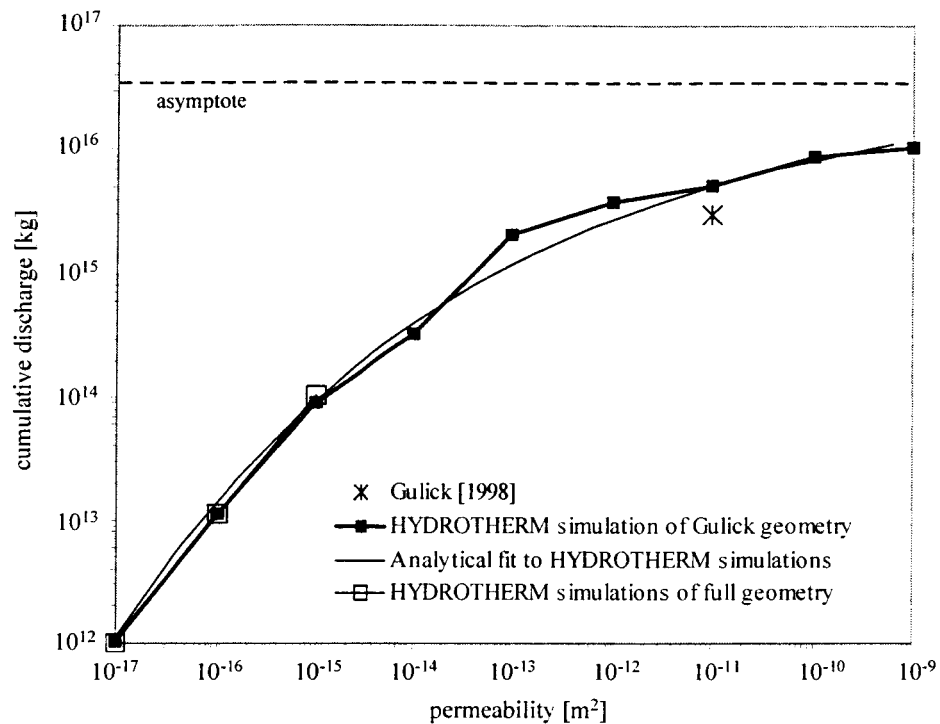


**Figure 2.3** Discharge results from HYDROTHERM models of a similar geometry to those of Gulick (1998). An analytic fit to these data, with its large permeability asymptote, is shown. The discharge obtained by the single permeability modeled by Gulick is provided for comparison, as are the total discharges of our three full geometry models (from Figure 2). The value obtained by Gulick was converted from volume to mass for the purpose of this figure, with an assumed water density of  $1000 \text{ kg.m}^{-3}$ .

For magma chambers with aspect ratios greater than the baseline model, it is no longer reasonable to assume that heat is lost through the chamber walls alone, and the total discharges for our geometry and that of Gulick (1998) are expected to diverge. Instantaneous discharge diverges even at the baseline aspect ratio, with a maximum value about 1.8 times higher for our geometry, and a steeper subsequent decay.

Magma chamber cooling times are of interest in these models and they are defined for our finite difference model as the average time taken for chamber cells to cool below a specified threshold temperature. For all three models, the cooling time

for a threshold of 450 °C (i.e. half the emplacement temperature) is approximately 30 kyr. While the magma chamber is impermeable, the groundwater flow past its walls does not significantly enhance cooling (see Norton and Knight, 1977). Once the chamber becomes permeable, however, cooling progresses at different rates in each model. The time taken for the chamber to cool to 250 °C is 67, 61, and 40 kyrs for permeabilities of  $10^{-17}$ ,  $10^{-16}$ , and  $10^{-15}$  m<sup>2</sup> respectively.

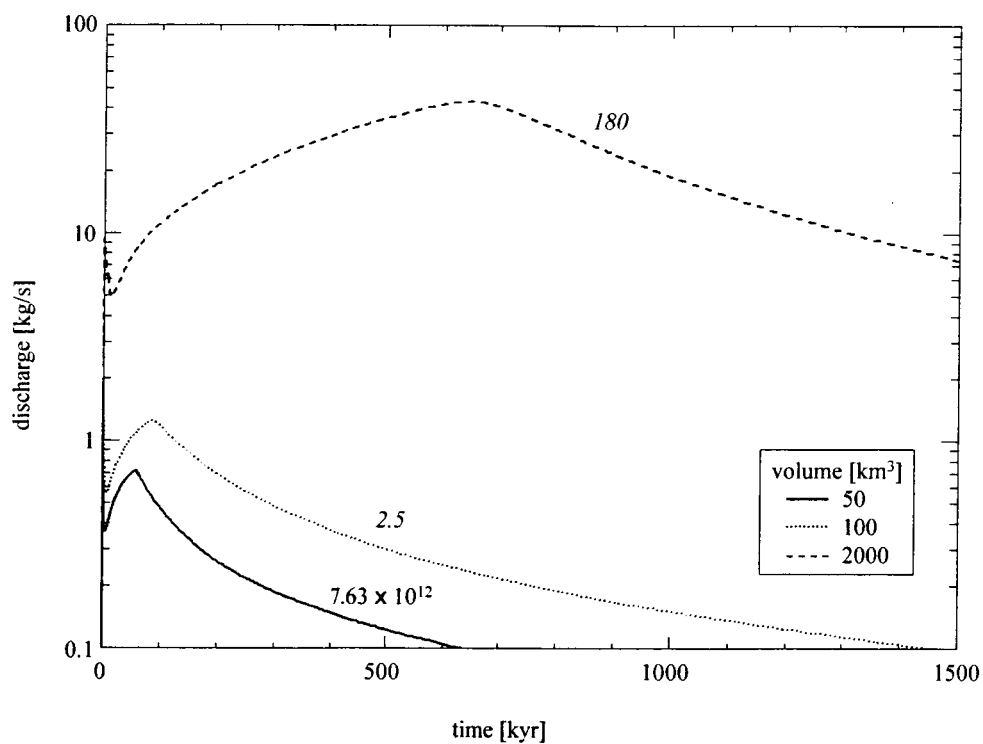


**Figure 2.4** Surface discharge from magma chambers of volume 50, 100, and 2000 km<sup>3</sup>, all at a depth of 8.5 km, an aspect ratio of 2, and with host rock permeability of  $10^{-16}$  m<sup>2</sup>. The total discharge of the 50 km<sup>3</sup> model appears above its curve. The numbers above the other curves denote the fraction of this discharge that their corresponding models produced.

### 2.3.2 Volume

Head and Wilson (1994) suggest that martian magma reservoir volumes could be as great as  $2000 \text{ km}^3$ , and that chamber depths are most likely to range from 8 to 12 km. we ran models of  $D/H = 2$  magma chambers with volumes of 100 and  $2000 \text{ km}^3$  at a depth of 8.5 km, in host rock with a permeability of  $10^{-16} \text{ m}^2$  (Figure 2.4). The  $100 \text{ km}^3$  chamber produced about 2.5 times as much discharge as the  $50 \text{ km}^3$  chamber, while the jump from 50 to  $2000 \text{ km}^3$  resulted in a factor of 180 increase. This approximately linear relationship is reflected in the magnitude of the instantaneous discharge, whose peak has proportional increases.

The total (cumulative) discharge from the system scales with three independent factors: chamber volume, surface area-volume ratio  $A/V$  (1.59, 1.26, 0.46, with increasing volume), and the average background host rock temperature into which the chamber is emplaced. Chamber volume is a measure of the total energy available to drive hydrothermal circulation;  $A/V$  is a measure of the relative duration of cooling (and varies with volume despite the conservation of aspect ratio); and average background host rock temperature is a measure of small differences in cooling time due to the low geothermal gradient. The deeper the chamber floor, and therefore the higher the average ambient temperature, the smaller the initial temperature gradient across the chamber surface. This slows the flux of heat into the country rock, producing greater cooling times and discharge longevity. Volume,  $A/V$ , and temperature together predict cumulative discharge  $s$  (relative to the baseline model) of 2.5 and 150 for volumes of 100 and  $2000 \text{ km}^3$  respectively, close to the modeled values.

Although not readily apparent on the semi-log plot of Figure 2.4, the discharge produced by the  $2000 \text{ km}^3$  chamber drops off at about 0.8 Myr, in agreement with

values obtained by Cathles *et al.* (1997) for a  $2500 \text{ km}^3$  chamber with host rock permeabilities ranging from  $4 \times 10^{-17}$  to  $10^{-16} \text{ m}^2$ .

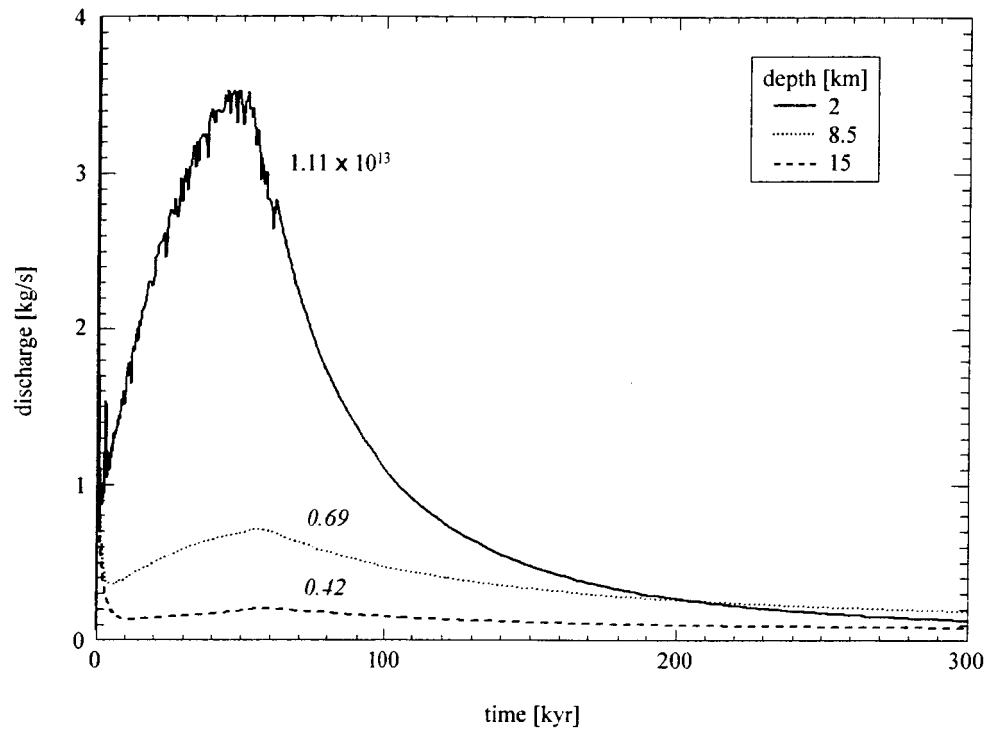


**Figure 2.5** Surface discharge from  $50 \text{ km}^3$  magma chambers at depths of 2, 8.5, and 15 km, all with aspect ratio 2, and with host rock permeability of  $10^{-16} \text{ m}^2$ . The total discharge of the 2 km deep chamber appears above its curve. The numbers above the other curves denote the fraction of this discharge that their corresponding models produced.

### 2.3.3 Depth

Models with  $50 \text{ km}^3$  magma chambers at depths of 8.5 and 15 km and with a host rock permeability of  $10^{-16} \text{ m}^2$  were run (Figure 2.5). Total discharge (relative to the baseline value) is 0.69 and 0.42 for chamber depths of 8.5 and 15 km respectively. Similar depth dependence exists for the same three chamber depths at host rock permeabilities of  $10^{-17}$  and  $10^{-15} \text{ m}^2$ .

An approximate prediction of the change in total discharge can be made by accounting for changes in chamber depth and the average background host rock temperature into which the chamber is emplaced. The depth of the chamber floor (which therefore also accounts for chamber height) and the average background host rock temperature together predict total discharge (relative to the baseline value) of 0.52 and 0.40 for chamber roof depths of 8.5 and 15 km respectively, similar to modeled values.

All three chambers cool to half their emplacement temperature in approximately 30 kyr and further cooling is required to demonstrate the effect of the small geothermal gradient: the 2 km deep chamber cools to 250 °C in 61 kyr, and the 15 km chamber takes 71 kyr. A summary of the total discharge of all nine depth and permeability combinations is depicted in Figure 2.6.

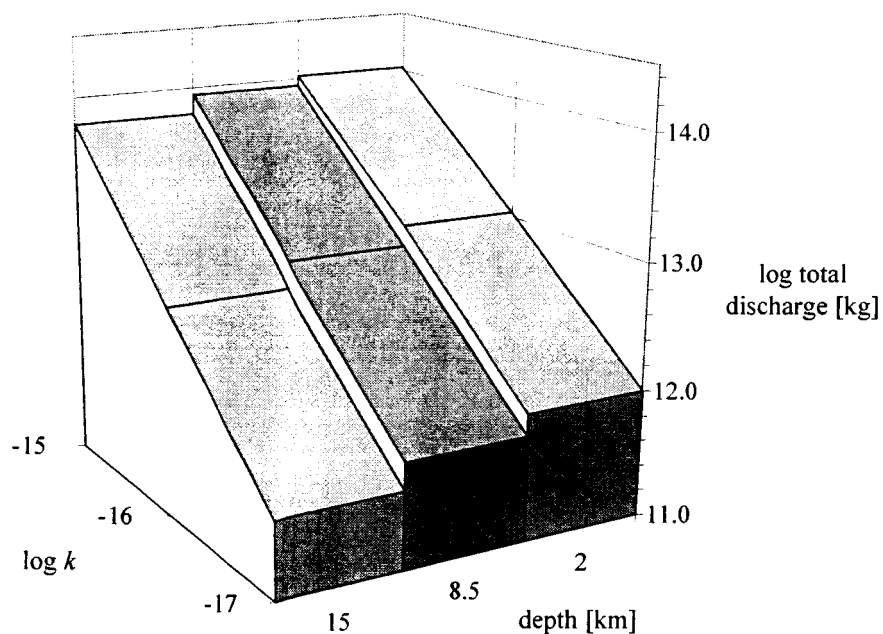


**Figure 2.6** Total discharge from 50 km<sup>3</sup> magma chambers of aspect ratio 2, at depths of 2, 8.5, and 15 km, and host rock permeabilities of 10<sup>-17</sup>, 10<sup>-16</sup>, and 10<sup>-15</sup> m<sup>2</sup>.

### 2.3.4 Aspect Ratio

Magma chambers with  $D/H = 0.2$ ,  $2$ , and  $20$  were modeled (Figure 2.7). These correspond to chamber radii of 1.2, 2.5, and 5.4 km, and chamber heights of 12, 2.5, and 0.54 km respectively. Chamber depth in all cases is 2 km, and chamber volume is  $50 \text{ km}^3$ . The radial extent of the host rock was fixed at 50 km for all three models in order to observe and compare the scale of flow produced by each magma chamber. In all three models the flow pattern consists of a single, clockwise rotating convection cell alongside the chamber. For  $D/H = 20$ , this pattern does not give way to a series of cells above the chamber roof, as one might expect for flow between two infinite horizontal surfaces at different temperatures.

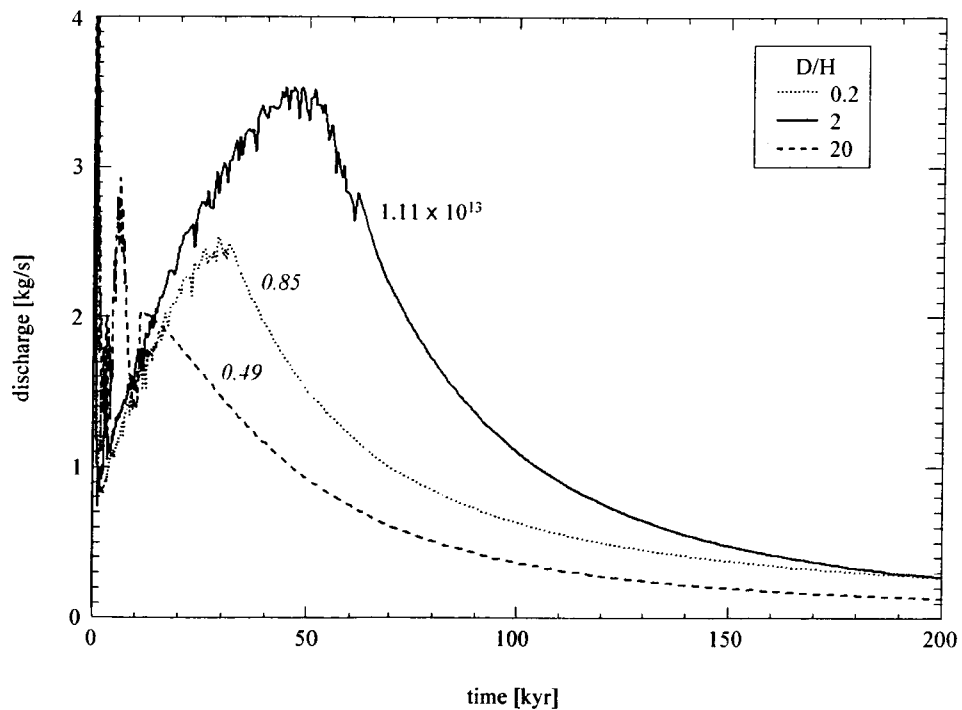


**Figure 2.7** Surface discharge from  $50 \text{ km}^3$  magma chambers with  $D/H = 0.2$ ,  $2$ , and  $20$ , all at a depth of 2 km, and with host rock permeability of  $10^{-16} \text{ m}^2$ . The total discharge at  $D/H = 2$  appears above its curve. The numbers above the other curves denote the fraction of this discharge that their corresponding models produced.

The discharge of these models is controlled primarily by the cooling time of the magma chamber and therefore its surface area-to-volume ratio  $A/V$  (1.89, 1.59, and  $4.06 \text{ km}^{-1}$  with increasing aspect ratio). Ratios of  $A/V$  predict cumulative discharges (relative to the baseline value) of 0.84 and 0.39 for aspect ratios of 0.2 and 20, again close to modeled values. The effects of aspect ratio are complicated by the presence of a substantial geothermal gradient, as discussed below.

### 2.3.5 Geothermal Gradient

Models with magma chamber aspect ratios of 0.2, 2, and 20 were run with an initial host rock geothermal gradient of  $20 \text{ }^\circ\text{C}/\text{km}$ , perhaps representative of early Mars (Schubert *et al.*, 1992). The flat, sill-like chamber ( $D/H = 20$ ) produces the greatest peak discharge because of its large horizontal exposure. The position of this chamber in relatively cool, high elevation host rock results in a greater temperature gradient across its surface and therefore more rapid cooling. Conversely, the tall, pipe-like chamber ( $D/H = 0.2$ ), being immersed in warmer temperatures at depth, cools more gradually. Its geometry produces the largest convection cell and offers minimum obstruction to flow, resulting in the greatest total discharge despite its low peak value. Overall, tenfold variations in aspect ratio produce changes in discharge of less than a factor of 3.

The times taken for magma chambers to cool to half their emplacement temperature are also affected by geothermal gradient and are, in order of increasing aspect ratio, 25, 45, and 4.0 kyr respectively. (In the absence of a significant geothermal gradient, the same chambers cool in 16, 28, and 3.5 kyr respectively.) An 8.5 km deep chamber cools to half its initial temperature in 52 kyr (as opposed to 30 kyr with a negligible geotherm), and produces about 7 times as much discharge with a peak 3.5 times higher.

It should be noted that for permeabilities greater than  $10^{-16} \text{ m}^2$ , the Rayleigh number of a plane porous medium (e.g., Turcotte and Schubert, 1982) at  $20 \text{ }^\circ\text{C}/\text{km}$  indicates that weak “free” convection may occur in the absence of a magma chamber. This phenomenon is indeed observed in high geothermal gradient models with no magma chamber. It has also been invoked by Raffensperger and Garven (1995) to explain the location of uranium ore deposits in sedimentary basins in Canada and Australia, and Travis *et al.* (2001) showed that it may be capable of melting significant volumes of subsurface ice in the martian crust. However, all of these models, including our own, have homogeneous permeability in the convecting zone: realistic vertical heterogeneity in planetary crusts will probably inhibit the development of large-scale free convection. While background geothermal gradients may have some affect on intrusion cooling times, we view their contribution to hydrothermal circulation as marginal.

### 2.3.6 Ice

Gulick (1998) suggested that a 2 km thick subsurface permafrost layer above a  $50 \text{ km}^3$  magma chamber would melt in a few tens of thousands of years. This is of the same order as the time taken for discharge to peak in our own models, indicating that ice could significantly reduce total discharge. we thus ran the baseline model with a 1 km thick layer of subsurface ice (Figure 2.8), modeled after Bonacina *et al.* (1973) who approximated melting by augmenting the specific heat over a small temperature interval  $\Delta T$ . The augmented value is given by

$$c_s = c_L + \frac{L}{\Delta T}$$

where subscripts  $S$  and  $L$  refer to the solid and liquid phases respectively, and  $L$  is the latent heat of fusion. we used  $c_L = 1000 \text{ J.kg}^{-1}.\text{K}^{-1}$ ,  $L = 3.34 \times 10^5 \text{ J.kg}^{-1}$ , and  $T = 5^\circ\text{C}$ , giving  $c_L = 6.78 \times 10^4 \text{ J.kg}^{-1}.\text{K}^{-1}$ .

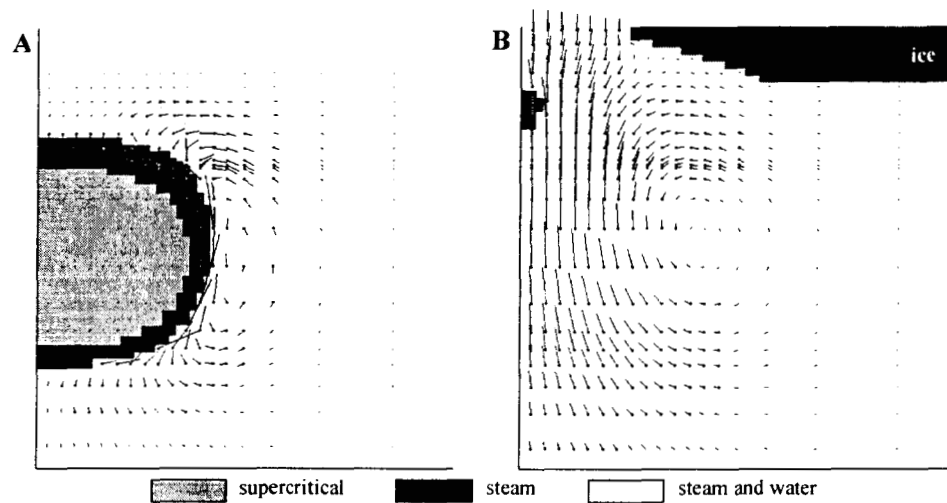


**Figure 2.8** Baseline model with an initially 1 km thick subsurface ice layer shown at 15 kyr (A) and 59 kyr (B). The scale in each image is about 5 by 5 km. Water and steam velocities are shown by black and gray streamers respectively. Only every other row and column are shown. Shaded regions (apart from the ice) represent different fluid phases as described in the key. At 59 kyr, only a small remnant of steam remains and the magma chamber has become as permeable as the host rock.

The hydrothermal system took 52 kyr to melt a hole in the ice. The total discharge was  $2.95 \times 10^{11} \text{ kg}$ , about a quarter that of the baseline model. This reduction (which is expected to be worse for deeper chambers and lower host rock permeabilities) may be useful for constraining an upper bound on permafrost thickness during valley formation on Mars, if indeed any permafrost is present during the Noachian. For valleys to form through sapping processes alone, the permafrost must be melted through, or aquifers carrying groundwater beneath the permafrost must intersect the surface. In either case, the permafrost can be no thicker than a few hundred meters.

### *2.3.7 Water Table*

Until now we have assumed a completely saturated host rock. If an unsaturated zone is present, part of the energy in the system must go toward elevating water to the surface, with the result that discharge is diminished. We compare with hydrostatic conditions the vertically integrated product of density, gravitational acceleration and depth in order to estimate the height a water table may attain through thermal-convective expansion. Integrations are performed over all vertical columns of finite difference blocks at all times, and for a range of water table depths. The discharge is calculated from those parts of the water table that intersected the surface, and compared to zero depth water table models. The results (Figure 2.9) show that models with a water table 50 m deep produce only 10% of their zero depth water table equivalents, while models with a 100 m deep table produce only 2%.

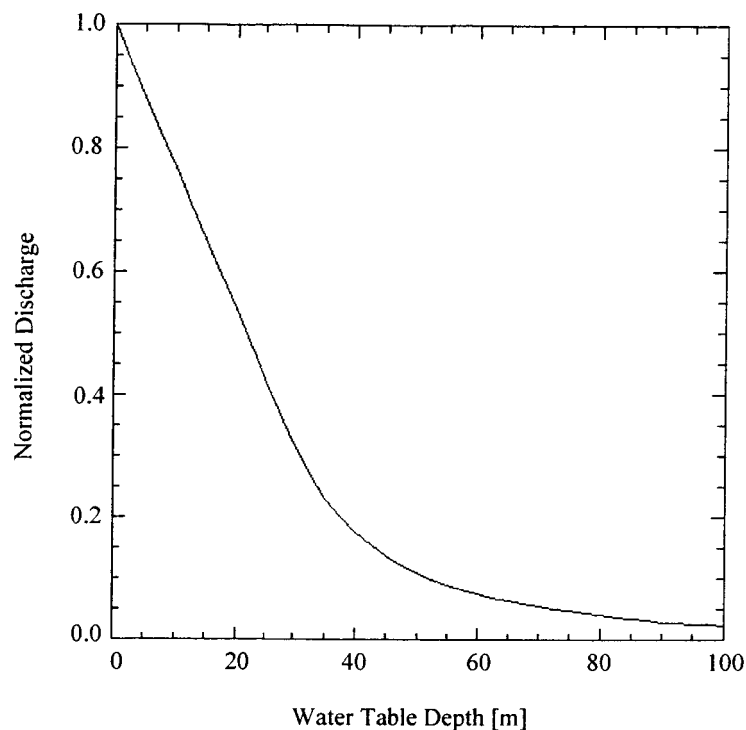


**Figure 2.9** Discharge as a function of water table depth, normalized to the zero depth water table value.

## 2.4 Discussion

### 2.4.1 Implications for Hydrothermal Alteration

Water/rock ratio (W/R) can be an important influence on the mineralogy of alteration products in hydrothermal systems. Martian hydrothermal alteration is thought to occur at low W/R (< 10 by mass) (Griffith and Shock, 1997, and Newsom *et al.*, 1999), in which case its effect is small, and the initial mineral composition is the primary influence on the alteration assemblage (Griffith and Shock, 1997).

HYDROTHERM mass flux results allow the W/R of a hydrothermal model to be calculated. The total flux of water through regions of the model above a specific threshold temperature are integrated over time. In this way, the W/R, or the total water mass that makes contact with the reacting rock, can be calculated for individual

finite difference cells. The W/R value averaged over all cells is a suitable representative of the system W/R, and is shown for the three reaction temperatures modeled by Griffith and Shock (1997), and for various model dimensions, in Table 2.1.

<i>Threshold temperature</i> ( °C)	$k = 10^{-15} \text{ m}^2$ volume = 50 km <sup>3</sup>	$k = 10^{-16} \text{ m}^2$ volume = 50 km <sup>3</sup>	$k = 10^{-16} \text{ m}^2$ volume = 2000 km <sup>3</sup>
150	0.12	0.025	0.067
200	0.18	0.037	0.10
250	0.28	0.054	0.15

**Table 2.1** Water/rock ratios (by mass) calculated for 8.5 km deep chambers of the indicated volumes and host rock permeabilities  $k$ .

The large velocities in the  $k = 10^{-15} \text{ m}^2$  model give the highest W/R for all threshold temperatures, approximately 5 times that of the  $k = 10^{-16} \text{ m}^2$  model with a chamber of the same volume. Negligible geothermal gradient and low host rock permeability in our models are both factors that contribute to small W/R. Typical martian geotherms ( $\sim 20 \text{ }^\circ\text{C/km}$ ) will lead to larger W/R, so these estimates can be viewed as lower bounds. The presence of a significant geotherm may be expected to increase discharge by a factor of about 3 or 4 (as observed in the model with an 8.5 km deep chamber with geothermal gradient), and since W/R is directly proportional to the discharge flowing through the alteration area, it may experience a similar increase. This would still leave most values listed in Table 2.1 below unity.

A primary goal of the work by Griffith and Shock (1997) was to model the amount of water bound to the rock during alteration. In a model based on the Shergotty SNC meteorite, about 8% of the final mineral assemblage (by weight) was water. It follows that in reactions with a W/R of 0.08, all of the water coming into contact with the rock would be sequestered in the final mineral assemblage – additional water for surface discharge would require W/R's in excess of 0.08. Assuming the Shergotty composition is sufficiently generic to be applied to our own

models, a W/R limit of 0.08 implies a minimum permeability of  $10^{-16} \text{ m}^2$  for a  $150 \text{ }^\circ\text{C}$  reaction in host rock surrounding a  $2000 \text{ km}^3$  chamber (Table 2.1). A caveat to this conclusion is that some water driven to the surface by hydrothermal convection will not pass through zones of chemical alteration, and will thus avoid being sequestered in the host rock.

Newsom *et al.* (1999) suggest that the relative abundances of mobile elements such as sulfur, chlorine, sodium, and potassium may be explained by the presence of a mixture of neutral-chloride and acid-sulfate fluids during soil formation. Production of the latter fluid requires vapor transport (Rye *et al.*, 1992), and Ingebritsen and Sorey (1988) discuss situations in which vapor-dominated zones may occur. Their models require combinations of low-permeability barriers and in some instances topographic gradients to sustain vapor-dominated zones, which develop in the shallow subsurface only. These specialized structures have not been included in our generalized models; nonetheless, our highest permeability model ( $10^{-15} \text{ m}^2$ ) with the shallowest chamber (2 km) does produce a short-lived (few thousand years) two-phase zone between magma chamber and surface. Steam develops here because of a combination of low pressures (which drop to a minimum of about two thirds hydrostatic pressure) and high temperatures. At lower permeabilities, fluid rising from the chamber does not transport enough heat upwards to elevate temperatures to the required levels for steam production.

If substantial quantities of vapor are required for soil alteration, then the abundance of steam in our high-permeability model may point to  $10^{-15} \text{ m}^2$  as a lower bound to permeability, a somewhat tighter constraint than that imposed by W/R ratio alone. Alternatively, if volcanic aerosols (Newsom *et al.*, 1999) or basalt palagonitization (McSween and Keil, 2000) produce sufficient soil alteration, then no such limit is necessary.

### 2.4.2 Relationship of Hydrothermal Circulation to Valley Networks and Magnetic Anomalies

The apparent spatial correlation between valley networks and magnetic anomalies suggests a link between processes involving the acquisition of thermoremnance in a cooling intrusion and processes involving the production of surface water for the creation of fluvial channels, i.e. hydrothermal circulation. An overlay of maps (Figure 2.10) showing the valley networks (Kieffer, 1981) and the vertical component of the magnetic anomalies as measured by the Mars Global Surveyor magnetometer (Acuña *et al.*, 1999) inferred at a constant altitude of about 200 km (Purucker *et al.*, 2000) visually suggests that the two are correlated (Jakosky and Phillips, 2001).

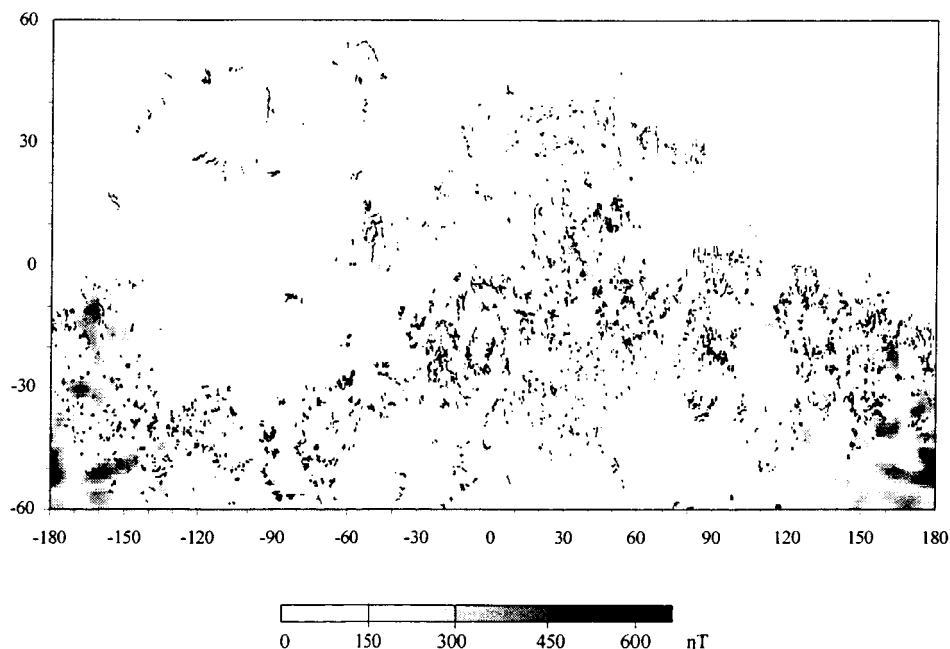


**Figure 2.10** Overlay of the absolute values of the 200 km vertical magnetic anomalies (Purucker *et al.*, 2000) and the valley networks (Kieffer, 1981) (cylindrical projection). Valleys were not mapped for latitudes below 60°S. The anomalies range from 0 to 670 nT.

A statistical analysis of the relative positions of valley networks and magnetic anomalies quantifies the correlation. A binomial test was performed, with success defined as the occurrence of a valley network and a magnetic anomaly (with vertical component above a specified threshold) in the same data bin. we consider only the southern highlands in these calculations. The valley network map (Kieffer, 1981) contains the coordinates of the 0.25 by 0.25 degree bins that contain valleys; the number and length of the valleys are not quantified. The magnetic anomaly map (Purucker *et al.*, 2000) is binned at 1 by 1 degree and was regridded at 0.25 degrees to match the valley grid. The number of degrees of freedom must, however, be adjusted to match the true spatial resolution, which is limited by the magnetic data. The total number of 0.25 degree bins is therefore multiplied by the quantity

$$\varepsilon = \left( \frac{0.25}{d_m} \right)^2$$

where  $d_m$  is the length scale in degrees for magnetic resolution. we determined that the variogram for the 200 km magnetic field reaches half of its sill (asymptotic) value in 200 km and 90% of the sill value in 400 km, in agreement with the rule of thumb for potential fields that the spatial resolution is approximately equal to measurement altitude. Therefore  $d_m \approx 200$  km ( $\approx 3$  degrees) may be most appropriate, but we consider a range from 2 to 6 degrees.

Relevant probabilities may be obtained using the total number  $N$  of 0.25 by 0.25 degree bins in the region of interest, the number  $n$  of these bins containing valleys, the number  $m$  of bins with magnetic anomalies above a specified threshold, and the

number  $C$  of correlations. The observed correlation probability is then  $p = C / n$ , while the expected correlation probability for a valley placed randomly in the region of interest is  $p_0 = m / N$ . The probability  $q$  of obtaining  $C$  or more correlations if the  $n$  valleys are placed randomly in the region of interest, can be obtained using the cumulative binomial distribution with  $\varepsilon C$ ,  $\varepsilon n$ , and  $p_0$  as the minimum number of successes, the number of independent trials, and the probability of a single success, respectively. A low value of  $q$  implies that the relative distribution of valleys and magnetic anomalies on Mars is not what one would expect from chance.

The results for a range of magnetic anomaly thresholds (Table 2.2) indicate that minimum chance probabilities occur near a 10 nT threshold for the vertical magnetic field at 200 km altitude. The area containing magnetic anomalies falls off sharply at higher thresholds, allowing a greater probability of chance correlation. At lower thresholds, the entire map is considered anomalous and so again it is easier to produce randomly the observed correlation. Over length scales at which the magnetic anomalies can be described as strongly coherent ( $d_m < 4$  degrees), the probability of a chance correlation is relatively small ( $q < 0.16$ ).

magnetic threshold [nT]	$p_0$	$p$	$(p - p_0)/p$	$q$			
				$d_m = 2^\circ$	$d_m = 3^\circ$	$d_m = 4^\circ$	$d_m = 6^\circ$
1	0.896	0.962	0.069	0.0785	0.182	0.494	0.464
2	0.827	0.928	0.109	0.0204	0.102	0.210	0.654
5	0.669	0.827	0.191	0.00228	0.0480	0.172	0.268
10	0.469	0.658	0.287	0.00223	0.0345	0.160	0.434
20	0.295	0.465	0.366	0.00459	0.0590	0.166	0.343
50	0.126	0.201	0.373	0.0686	0.303	0.330	0.612
100	0.0521	0.0818	0.363	0.260	0.450	0.575	1

**Table 2.2** Statistical data for the correlation between valley networks and magnetic anomalies.

A genetic correlation requires that the valley networks and magnetic anomalies are the same age. A significant majority of valleys are Noachian (70-92%; Scott and

Dohm, 1992; Carr, 1996); many of those that are younger are not in the southern highlands and so are excluded from our survey. The magnetic anomalies, because of their inferred deep-crustal origin (see Proposition 1 below) without surface manifestation, must also be very old. However, even the oldest valley networks individually preserve only some part of the Noachian that was not subsequently locally erased, whereas the magnetic anomalies probably reflect a greater span of crustal history. In other words, some valley networks that were associated with magnetic anomalies may have been resurfaced, whereas other valley networks may have formed subsequent to emplacement of the magnetic anomalies by hydrothermal or other processes. The normalized excess of correlated valleys and magnetic anomalies  $(p-p_0)/p_0$  (Table 2.2) may be taken as representative of the fraction of valleys for which a genetic correlation may be inferred, between about one-quarter and one-third.

The role of hydrothermal circulation in the relationship between valley networks and magnetic anomalies may now be described in terms of a central hypothesis composed of two main propositions, defined and discussed in the following sections.

*Proposition 1.* The first proposition is that the magnetic anomalies formed as intruded crust and that the acquisition of thermal remnant magnetization (TRM) occurred at relatively great depth. The strong observed magnetizations in the martian crust of 20 to 40 A.m<sup>2</sup> (Connerney *et al.*, 1999; Grimm, 2000) imply magnetization depths of up to a few tens of kilometers. The presence of magnetic anomalies in Arabia Terra, which has been strongly resurfaced (McGill, 2000; Hynek and Phillips, 2001) also points to a deep origin. On Earth, Layer 3 gabbros of the oceanic crust are magnetized to the extent that they contribute between 25% and 75% of the observed marine anomalies (Pariso and Johnson, 1993), while the underlying mantle is

unmagnetized (Wasilewski *et al.*, 1979). Therefore deep crustal magnetization of Mars is reasonable.

The mineral composition of the magnetized material producing the magnetic anomalies is likely to contain magnetite or hematite as the primary magnetic carrier. Although magnetite is generally favored, there is much support for hematite (e.g., Connerney *et al.*, 1999). Kletetschka *et al.* (2000) show that for an applied magnetic field of 0.1 mT (about twice the strength of the earth's present geomagnetic field), multidomain hematite reaches maximum TRM saturation, whereas magnetite only reaches only a few percent thereof.

*Proposition 2.* The second proposition is that hydrothermal discharge attending crustal formation processes in the southern hemisphere of Mars was sufficient to provide the water necessary to carve the valley networks. Hydrothermal systems on earth exhibit such discretized concentration of outflow, as evidenced by the presence of geysers and springs rather than diffuse outflow everywhere above the magmatic intrusion. The martian valley networks are characterized by low drainage densities, implying again that crustal heterogeneities may localize discharge.

Testing this proposition requires knowledge of the amount of water necessary to erode the valley networks, the total amount of water available to hydrothermal systems, and the actual hydrothermal discharge produced. An estimate of the required water volume for valley erosion may be made from values of areal coverage, drainage density, valley cross-section, and sediment-to-water ratio. Using a map of drainage densities (Carr and Chuang, 1997) we estimate the total area covered by valley networks to be about  $1.4 \times 10^7 \text{ km}^2$ . Since we estimated earlier that only one quarter of the valley networks may preserve direct interaction with hydrothermal systems, we use a reduced effective area of  $3.6 \times 10^6 \text{ km}^2$ . Carr and Chuang (1997)

calculated a globally averaged drainage density of  $0.0032 \text{ km}^{-1}$ . The product of effective area and drainage density, multiplied by typical valley width and height (5 km and 150 m respectively), result in  $8.6 \times 10^3 \text{ km}^3$  of removed material. Sediment-to-water ratios may range from 1:4 to 1:1000 (Gulick, 1998, and references therein), implying that the volume of water required to erode the valleys was between  $3.5 \times 10^4$  and  $8.6 \times 10^6 \text{ km}^3$ , equivalent to a global water layer between 0.2 and 60 m deep. These values are well below the estimate of hundreds of meters for the global crustal inventory, indicating that discharge from the valleys had a negligible impact on the global water budget. They further imply that discharged water need not have been recharged to the crust.

The total hydrothermal discharge produced is computed as follows. First, we assume that each magma chamber contributing to crustal formation intrudes into steady ambient temperature and pressure conditions; this is most likely if intrusions that formed the southern highlands moved between different loci rather than spreading from a single location (Grimm, 2000). In this way, the discharge contribution from a single intrusion is just that of its equivalent HYDROTHERM model. we assume further that the crust covering the area occupied by valley networks (as calculated above) is eventually built up to a depth of 20 km by magma chambers packed side by side and one on top of the other. we sum the total discharges from each intrusion to calculate the total mass of surface water produced. we consider only those intrusions that contribute to magnetic anomalies, discarding other intrusive events. Determining the relative contribution of individual intrusions is not possible, but the probability  $p_0$  may be used as an indicator of the appropriate fraction to be considered. Its value for a magnetic threshold of 10 nT, i.e. 0.469 (Table 2.2), is applied to all of our results.

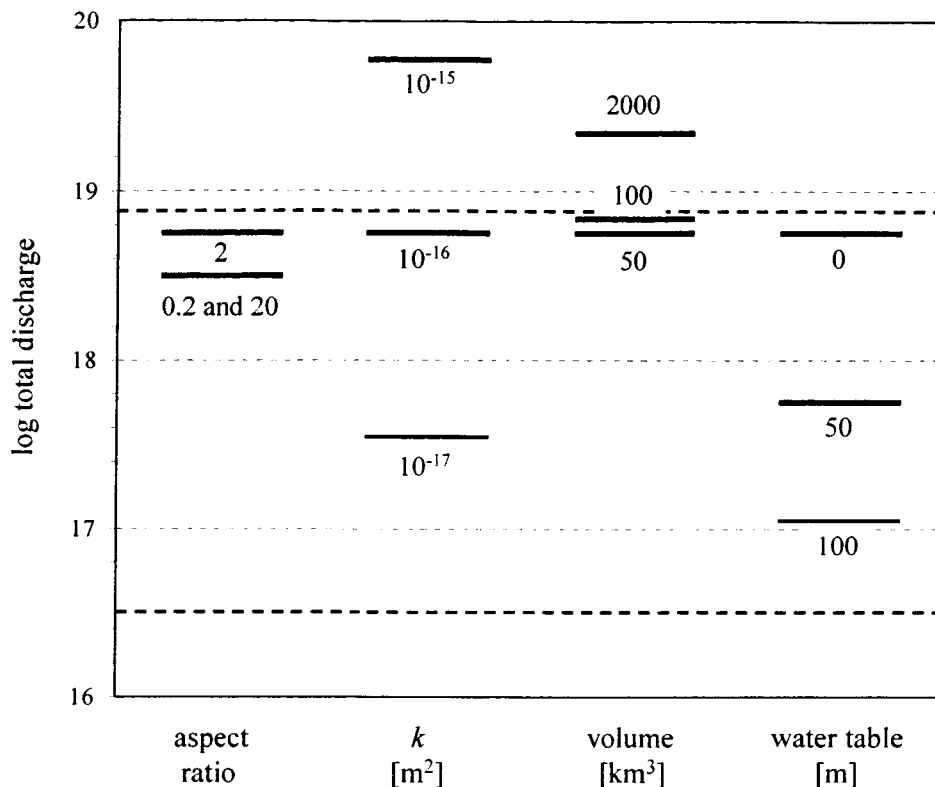


**Figure 2.11** Summary of global discharge production (by mass, in kg) for various model parameters. The two thick dashed lines indicate the bounds on the mass of water required to erode the valley networks. Represented are discharge values for different magma chamber aspect ratios, host rock permeabilities, magma chamber volumes, and for the baseline model with different assumed water table depths. Note that the baseline model ( $D/H = 2$ ,  $k = 10^{-16} m^2$ , chamber volume =  $50 km^3$ , water table depth =  $0 m$ ) appears in each vertical group of bars.

A summary of discharge production over the entire region of interest is shown for different models in Figure 2.11. The two thick dashed lines denote the bounds on total required discharge. Represented are discharge values for different magma chamber aspect ratios (all with a volume of  $50 km^3$ , host rock permeability of  $10^{-16} m^2$ ), host rock permeabilities (all chambers have  $D/H = 2$  and a volume of  $50 km^3$ ), magma chamber volumes (all chambers have  $D/H = 2$ ; host rock permeability is  $10^{-16} m^2$ ), and values for the baseline model with different assumed water table depths.

All models meet or exceed the discharge production requirements, although it should be noted that if the  $k = 10^{-17} \text{ m}^2$  model is assumed to have a water table of 100 m, its production will fall below the minimum required value. Other factors such as evaporation may further reduce the discharge available to carve valleys. The present evaporation mass flux is likely in the region of  $4 \times 10^{-8} \text{ kg.m}^{-2}.\text{s}^{-1}$  (Ingersoll, 1974), which would reduce the effective discharge by as much as an order of magnitude or more. Ice may also reduce discharge (Section 3.6). A 1 km thick layer of subsurface ice in our baseline model causes a 75% drop in total discharge. In models with other parameter values (e.g. greater magma chamber depth and smaller host rock permeability), ice may inhibit discharge more severely, if not completely.

## 2.5 Conclusions

In numerical models of martian hydrothermal systems, we explored the control on surface discharge of magma chamber depth, volume, aspect ratio, and host rock permeability and porosity. Discharge has an approximately linear relationship to magma chamber volume and host rock permeability (in the range  $10^{-17}$  to  $10^{-15} \text{ m}^2$ ). The influences of depth and aspect ratio are weaker, and that of porosity is negligible.

Some geochemical aspects of martian hydrothermal systems were considered by calculating water/rock ratios in our numerical models at various reaction temperatures. Ratios tend to be low, but sufficiently large at mean permeabilities  $> 10^{-16} \text{ m}^2$  for groundwater flow to be sustained, consistent with the expected storage of water in alteration assemblages. The presence of a short-lived vapor-dominated zone in our model with high host rock permeability ( $10^{-15} \text{ m}^2$ ) and shallow chamber depth (2 km) suggests that hydrothermal alteration processes may be responsible for the observed relative abundances of certain salts in the martian soil, although other forms of alteration should not be excluded.

Crustal formation processes which formed the magnetic anomalies observed on Mars today may have been attended by hydrothermal circulation that also provided surface water for valley network erosion. This idea is in agreement with the observed spatial correlation between magnetic anomalies and valleys and was tested further within the framework of a central hypothesis made up of two propositions. The first is that the magnetic anomalies formed as intruded crust and that the acquisition of thermoremnance occurred at relatively great depth. The second is that hydrothermal discharge attending global crustal formation processes is sufficient to provide the water necessary to carve the planet's valley networks.

we tested this hypothesis using the numerical models described above, assuming that the crust was formed by the heterogeneously spaced and timed intrusion of multiple magma chambers, each of which produced the discharge predicted by its individual numerical model. we determined that many model configurations in the explored portion of the parameter space were capable of producing sufficient water to erode those valley networks statistically related to hydrothermal circulation. In particular, modest crustal permeabilities of  $10^{-16}$  to  $10^{-15} \text{ m}^2$  can produce the discharge required to carve valleys and satisfy geochemical constraints, even in the presence of mitigating factors such as evaporation and finite water-table depth.

## CHAPTER 3

### LONG RUNOUT LANDSLIDES

#### 3.1 Introduction

Landslide features on Mars bear an unambiguous resemblance to terrestrial landslides. They occur mainly in the equatorial Valles Marineris canyon system, in both open and closed depressions (Lucchitta 1979). The aureole deposits on the lower flanks of the largest Martian shield volcano, Olympus Mons, may also be landslides (Lopes 1980, 1982), although slower processes such as gravity spreading may have been responsible for their formation (Francis and Wadge 1983, Tanaka 1985). In many Valles Marineris landslides a curved scar cut into the canyon rim indicates the site of the original failure. The scar is typically a few tens of kilometers wide and recedes a few kilometers into the canyon wall. Landslides occur in walls as high as 8 km and cover horizontal distances (runouts) as great as 80 km if unimpeded by obstacles. The volume of individual landslide deposits ranges from tens to thousands of cubic kilometers.

Of all the processes that have shaped the Valles Marineris, landsliding is among the most recent. The landslide scars are smooth and the deposits are sparsely cratered and show little evidence of deflation (Lucchitta 1992) suggesting a late Hesperian to Amazonian genesis. Slide scars cut into pre-existing spur-and-gully formations, and the slide material overlies interior deposits. There is, however, some indication that tectonic movement postdating landslide deposition has occurred along faults closely related to the formation of the Valles Marineris (Lucchitta 1979, Lucchitta *et al.* 1994). Earlier marsquakes triggered by tectonic activity may have been responsible for triggering the landslides (Caruso, 2003).

Although reentrants are generally smooth, their upper elevations are typified by dark vertical banding which, on close inspection of MOC images, is seen to consist of small, rugged spur formations, sometimes horizontally striated, that are consistent with the volcanic nature of the plateaus surrounding the Valles Marineris (Scott and Tanaka 1986). Emanating from the lower boundaries of these miniature spurs are lighter colored, linear, overlapping talus deposits blanketing the lower elevations of the scar. The influence of material strength heterogeneity on landslide dynamics is discussed below.

The landslide deposits themselves have small-scale features, some of which are difficult to explain. These include longitudinal grooves, rather than transverse ridges like those observed on terrestrial slides. Lucchitta (1979) suggested that longitudinal grooves result from differential forward velocities that can be explained by the presence of a fluid. Many large deposits, both martian and terrestrial, have runouts that imply substantially lower internal friction angles than those typical of rocky materials. Processes thought to produce long runouts typically require fluidization by water (Habib 1975, Goguel 1978) or air (Kent 1966, Shreve 1968). Arguments have been given in support of both the presence (Lucchitta 1987) and absence (McEwen 1989) of water in the Valles Marineris slides. Chaotic terrains at canyon termini, fluvial features on canyon rims (Carr, 1996; Coleman *et al.*, 2003), and the possibility of ice-related processes in interior layered deposit formation (Weitz and Parker, 2000) all point toward the past presence of water in the Valles Marineris.

The thin Martian atmosphere is unlikely to be dense enough to provide lubrication, but outgassing of carbon dioxide from the soil on failure could play an important role. Some fluidization processes do not require an actual fluid: in dispersive grain flow (Bagnold 1954), the weight of the material is supported by impacts between its constituent rock particles, whereas for acoustic fluidization

(Melosh 1979) an acoustic field transmitted through the material is sufficient to support for brief periods the static overburden pressure without requiring separation of particles.

Features of landslide morphologies may be used to infer their dynamic behavior. Rheology is an important influence on the final configuration of a landslide: given a particular runout path and initial mass configuration, it is largely the rheology that determines key features such as runout length and final deposit thickness and slope. Here we report the results of numerical models of martian landslides designed to constrain rheological parameters. Comparisons are made with terrestrial and lunar models.

## **3.2 Model**

### *3.2.1 Numerical Simulations*

we use a dynamic analysis model (DAN, Hungr 1995) which, given the runout path and initial mass profile, computes the time-varying shape and velocity distribution of the slide. DAN has been successful at modeling terrestrial landslides with a wide range of rheologies, including sand and coal failures (Hungr 1995) and, where physical parameters are not available for comparison, it successfully reproduces other numerical analyses (Hungr 1995), including that of the Madison Canyon, Montana rock avalanche (Trunk et al 1986).

A finite difference Lagrangian approach is used to track individual mass blocks as they move together down the runout path. Each slide is modeled as a single row of blocks (20 in our models) whose initial heights depend on the prescribed initial shape of the failed mass. Quantities that vary normal to the runout path are represented by their average values. For each block, the component of the gravitational force along (tangential to) the runout path works against a pressure contribution and a basal

resistance force. The pressure contribution arises from the differing heights of adjacent blocks. Material tends to shift laterally to reduce high, unstable surface slopes. The resulting communication of pressures throughout the landslide is controlled by a lateral pressure coefficient whose lower and upper bounds reflect the tensional and compressional strengths of the material respectively. The pressure coefficient has a small influence on the final profile and is not considered to be of primary importance.

The basal resistance force for each block is determined by one of several available rheologies, which include frictional, Bingham, and power law. In the frictional rheology, the basal resistance offered by a block is proportional to the normal stress it exerts on the runout path. The constant of proportionality is the friction coefficient, often expressed as the tangent of the angle of internal friction  $\phi$ , set to  $20^\circ$  in all models unless where otherwise specified. By default, DAN uses the same static and dynamic friction angles. In reality, the dynamic friction angle is less than the static value (the latter is typically around  $30^\circ$  for fractured crustal rock, Brace and Kohlstedt 1980) and may change with the velocity of the material (Jaeger and Cook 1979). Other workers (e.g., Wang 1997) have used models with dynamic friction coefficients as low as 0.6 times the static value (i.e. a static angle of  $30^\circ$  corresponds to a dynamic value of  $19^\circ$ ). There is also a dependence on clay content (Skempton 1964) that could reduce the dynamic angle by a few degrees. Small quantities of clay minerals have been observed indirectly in spectra (e.g., Soderblom 1992) and directly in the SNC meteorites (e.g., Gooding *et al.* 1991 and Treiman *et al.* 1993). Our choice of friction angle thus represents a physically plausible lower limit. The frictional law used in DAN is such that a change in friction angle will have the same affect on dynamics as a corresponding change in pore fluid pressure. A lower limit for friction angle thus

precludes the interpretation of pore pressure as artificial compensation for an exaggerated friction angle.

The basal resistance also depends on the pore-pressure coefficient  $r_u$ , defined as the ratio of pore pressure exerted by an interstitial fluid to the total normal stress at the base of the block. Pore fluid carries some of the weight of the overlying material, reducing basal friction. We stress that a given pore pressure coefficient describes conditions at the failure surface only and heterogeneities in permeability may allow other parts of the failed wall section to remain dry. Consequently, pore pressure coefficients that correspond to hydrostatic or even superhydrostatic pressures do not necessarily imply total saturation at all depths. The basal resistance is also affected by centrifugal forces, since these increase or decrease the effective normal stress according to the curvature of the path.

The Bingham rheology, used successfully to model rock avalanches (Hungr 1995, and references therein) consists of a Newtonian fluid with a finite yield strength  $\tau_0$ . Assuming that shear stress increases linearly with depth, the constitutive equation (which relates shear stress to velocity gradient) may be integrated to yield an expression for the basal resistance in terms of fluid velocity  $v$ , yield strength, and dynamic viscosity  $\mu$ . (The basal resistance is simply the shear stress at the base of the slide.) The yield strength gives rise to a solid cap which rides on top of the flow. As the deposit extends itself along the runout path, its tensile strength slows it down, causing the cap to thicken until it consumes the entire flow, bringing the deposit to a halt. This effect is exacerbated by the lowering of the cap as the deposit thins. Landslides with higher yield strengths have thicker caps and so form thicker deposits with shorter runouts.

A power law may be used to model flows in which most of the lateral shear is concentrated in a thin basal layer (Melosh 1987) such as the Blackhawk landslide in

California (Shreve 1968). The Elm landslide in Switzerland was simulated successfully by Hsu (1975) in a scaled down model using a bentonite suspension, a fluid with power law behavior (Besq *et al.* 2000). For a power law fluid, the shear stress is

$$\tau = \tau_0 + \mu \left( \frac{dv}{dz} \right)^n \quad 3.1)$$

where  $z$  is depth and  $n$  is a unitless index. In Equation 3.1, the symbol  $\mu$  does not have units of real viscosity and is called the “apparent” viscosity. we adopt  $n = 0.125$  (suggested by Melosh (1987) for acoustic fluidization) for all slides and for both fluidization processes. A value of 1 represents a Bingham fluid, while a value of 0 corresponds to a rigid sliding block. we investigated the sensitivity of runout to  $n$  for a martian slide (Slide 3 below) and found that within the range of 0 to 1, halving or doubling the value of  $n$  increases or decreases runout by 2 to 2.5 km for a slide with a runout of 72 km at  $n = 0.125$ . The uncertainty in our choice of  $n$  is thus largely immaterial.

we consider next a general fluidization process in which the slide is frictional on failure but becomes fluidized when sufficiently energetic, behaving more like a power law fluid. Lucchitta *et al.* (1992) explicitly suggests such a rheological transition. As noted above, pore pressure may be specified explicitly in the frictional rheology. With the power law, however, water content is implicit and its influence is assumed to manifest itself through the determination of yield strength and apparent viscosity.

A special case of general fluidization is acoustic fluidization (Melosh 1979), which can occur without the presence of a liquid or gas and whose frictional stage may thus be associated with zero pore pressure. When acoustic waves of sufficient strength are transmitted elastically through the individual constituents of the landslide material, intra-particle rarefactions produce short periods of decreased overburden

pressure, temporarily reducing basal resistance. The acoustic field builds up to the required strength some time after the initial failure, so fluidization does not occur immediately. Although acoustic fluidization may be possible in the presence of an interstitial fluid, we address here the case of dry material only. This is, in fact, the fundamental distinguishing feature of this rheology and since it includes no explicit dependence on the acoustic processes described above, it may encompass other processes in which frictional and power law behaviours occur in the absence of fluid pressure, if others indeed exist.

For clarity we note that the general and acoustic fluidization processes are not modal rheologies, but sequential combinations of two rheologies: frictional and power law. In general, the yield strength and apparent viscosity of the power law stage for a particular slide will not be the same for acoustic fluidization and general fluidization. The values of these parameters depend on the position at which the frictional rheology ends and the power law begins, and also on the velocity and stress distribution of the material at the transition. Transitions occurring further along the runout path have a frictional stage ending with different velocities, and the power law stage must thus have a different yield strength and/or viscosity in order to conserve runout.

Inputs common to all rheologies include unit weight  $\gamma$ , volume yield rate  $E$  (a measure of material deposition or entrainment, described below), and the lower and upper bounds of the lateral pressure coefficient. Unit weight was taken to be 10.00 kN.m<sup>-3</sup> for martian slides, 26.44 kN.m<sup>-3</sup> for terrestrial slides, and 4.371 kN.m<sup>-3</sup> for lunar slides, corresponding in all cases to a density of 2700 kg.m<sup>-3</sup>.

### 3.2.2 Landslide Geometry

Landslide deposit volume  $V$  was estimated for martian slides by summing  $1/32$  by  $1/32$  degree Mars Global Surveyor (MGS) MOLA elevation data over the area covered by the material (Viking images were used to determine the location of deposit boundaries). For these calculations, the base of the deposit was assumed to be horizontal and its elevation was inferred from the surrounding canyon floor, or matched to the toe of the deposit. Our method of calculating volumes differs from previous approaches (e.g., McEwen 1989) which used the scar geometry to estimate the initial volume of the failed section of canyon wall. Since the configuration of the pre-slide wall is unknown there is considerable uncertainty in measuring volume this way; a direct measurement of the final deposit volume is likely to be more accurate.

we assumed initially that volume was conserved during the slide event (i.e. no net deposition or entrainment of material). Approximate measurements of scar width  $W$ , scar slope  $\alpha_1$ , and typical nearby wall slope  $\alpha_2$  allowed us to infer a suitable initial configuration for the failed material, with the required volume (Figure 3.1). Our use of volume as the primary measurement used to reconstruct the initial configuration is in line with experimental evidence (Hsu 1975) showing that volume, rather than geometry, has the stronger influence on runout. Nonetheless, the initial configuration was adjusted to match the shape of the unfailed wall adjacent to the landslide scar, where possible. Similarly, the runout path was shaped according to nearby wall and floor geometry. The coordinate system (Figure 3.1) was positioned such that the back edge of the top surface of the initial shape was at  $x = 0$ . The vertical coordinate represents elevations relative to the MOLA datum.

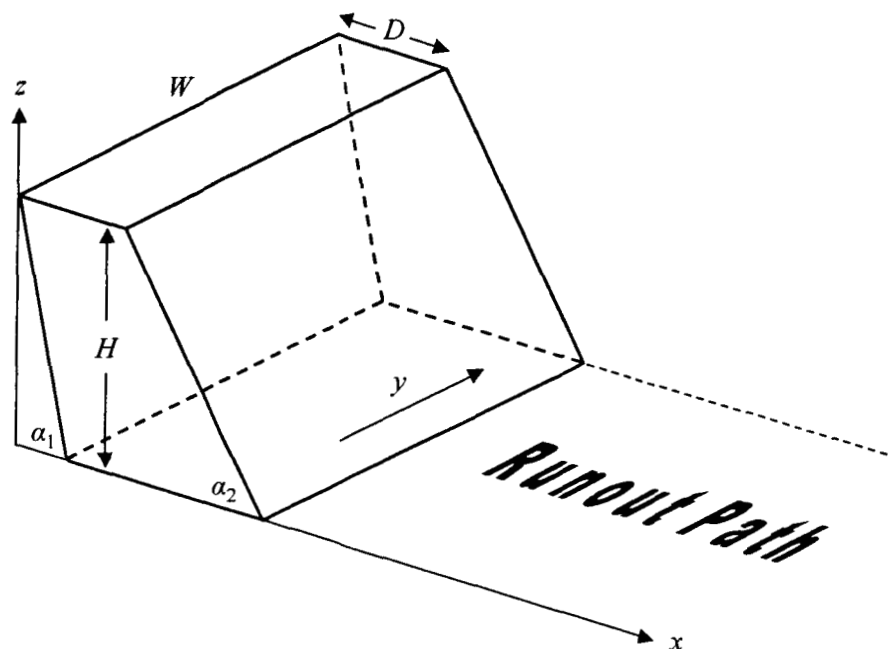


**Figure 3.1** Conceptual model of initial landslide shape. Symbols correspond to those defined in the text. Runout occurs in the positive  $x$  direction.

MOLA data were used to obtain vertical cross-sections of the landslide deposits along the direction of motion (all cross-sections mentioned henceforth refer to this plane). These were compared to DAN results to assess the suitability of the chosen rheological parameter values. Values were iteratively adjusted and the model rerun until a suitable final profile was achieved.

In DAN, different sections of the runout path may be assigned different rheologies. we took advantage of this feature to simulate general and acoustic fluidization. The dynamics of the transition from frictional to power law is not well established and we chose the bottom of the initial steep section of the runout path as the default transition point. The transition position was varied about this point from model to model depending on the characteristics of the flow (such as velocity) and structural features observed in the final deposit profile (such as abrupt decreases in

slope). Rather than an abrupt change in rheology, this transition should be seen as the point at which the power law rheology becomes better than the frictional rheology at describing the motion.

The conceptual model of landslides described thus far is somewhat limited by its essentially two-dimensional nature since changes in runout path width (dimension  $y$  in Figure 3.1) may influence the final cross-section of the deposit. In most cases, the landslide scar is curved in the cross-slope direction, i.e. each contour line is crescent-shaped. (In the downslope direction the scars, where exposed, are remarkably linear). This trend, which supposedly continues into the buried parts of the scars, suggests that material converges during the initial, steep part of its journey. On reaching the level, unconfined canyon floor, most of the energy in the slide has been channeled directly forward, resulting in a toe which travels further than the laterally spreading material on either side. The resulting deposit is shaped like an arrowhead pointing in the direction of motion. Despite lateral spreading, the average final deposit width is frequently smaller than the average initial width. Indeed, initial cross-sectional areas of the slides studied here are frequently smaller than final cross-sectional areas (Table 3.1), implying an average decrease in width in order to conserve volume. One can specify the required deposit width at each point along a DAN runout path. This feature is intended to simulate the effects of a laterally confining channel and is thus suitable for the curved landslide scar in our models. Unconfined spreading is best modeled by fixing the path width on the canyon floor to match the observed deposit.

Another way to account for changes in cross-sectional area is to relax constraints on volume conservation. Landslides typically accumulate new material during the initial downhill phase. In DAN, one can specify the desired amount of entrainment or deposition over segments of the runout path. Individual block volume is updated at

each time step as follows (Hungar and Evans 1997)

$$V_j = V'_j + E\Delta s \frac{V'_j}{V} \quad (3.2)$$

where  $V$  is the total slide volume,  $V'_j$  and  $V_j$  are the old and new volumes of the  $j$ th block, respectively, and  $\Delta s$  is the displacement of the  $j$ th block during the time step. Parameter  $E$  is a volume per unit runout path length and specifies how much material is deposited or entrained (depending on its sign). If the entire slide passes over a segment of the runout path with length  $a$  and entrainment rate  $E$ , the total change in volume is given approximately by  $aE$ . we assigned a finite entrainment rate to the initial, steep section of the runout path, and a value of zero elsewhere. Values of  $E$  for our models range from  $10^4$  to  $10^7 \text{ m}^3 \cdot \text{m}^{-1}$  depending on the initial volume of the slide and the required change therein.

slide number	H (km)	$H/L_f$ (unitless)	$\alpha_1$ (°)	D (km)	initial cross-sectional area (km <sup>2</sup> )	final cross-sectional area (km <sup>2</sup> )
1	1.1	0.112	19.0	0.26*	0.17	0.15
2	8.0	0.173	24.2	8.6	74	120
3	7.7	0.0980	24.2	8.6	67	84
4	5.0	0.0966	14.1	4.0	27	26
5	4.5	0.122	26.4	0.47	1.9	2.2
6	5.6	0.107	16.4	3.1	16	17
7	7.3	0.101	22.0	7.4	64	105
8	10	0.0145	3.31	86*	720	720
9	2.4	0.273	24.8	0.022	0.048	0.048

**Table 3.1** Information inferred from vertical cross-sections parallel to the direction of motion. In some Valles Marineris slides, the initial mass was modeled after nearby unfailed canyon wall and the value for  $\alpha_2$  represents an average, rather than an exact, value. Depth values with an asterisk indicate the average value for a wedge-shaped initial shape.

we ran models in which changes of cross-sectional area were produced exclusively by either width or volume variations, or a combination of both. In the last case, measurements of the landslide geometry were used where possible to constrain the width variations, and volume variations were adjusted to account for the

remaining change in cross-sectional area. The models presented here are exclusively of this last kind, although we note that models with only one kind of variation did not produce significantly different results.

### 3.3 Results

we present detailed models of a terrestrial landslide, six Valles Marineris landslides, part of the Olympus Mons aureole, and a lunar landslide. Four of the Valles Marineris slides have been described in detail by Lucchitta (1979) and we refer to her landslide numbering scheme for easy reference. Images of Slides 1 to 9 are shown in Figure 3.2, and initial and final deposit dimensions are given in Tables 3.1 and 3.2.

slide number	$V$ (km <sup>3</sup> )	horizontal coverage (km <sup>2</sup> )	$L_r$ (km)	$L_f$ (km)	$W$ (km)	$\alpha_1$ (°)
1	0.283	15	2.5	9.8	1.7	15.3
2	2100	1500	5.5	79	29	25.9
3	1700	1600	5.5	72	26	24.4
4	67	1300	3.8	51	26	32.5
5	14	170	6.7	26	7.1	26.4
6	460	2000	13	58	29	16.4
7	1300	1000	9.0	60	33	22.0
8	36,000	420,000	160	690	500	25.9
9	0.200	21	5.0	8.8	4.2	24.8

**Table 3.2** Landslide deposit dimensions. Values for the terrestrial slide (1) were calculated from maps and cross-sections from Shreve (1968), values for martian slides were measured from MOLA data, and values for the lunar slide (9) were calculated from data and cross-sections from Howard (1973).

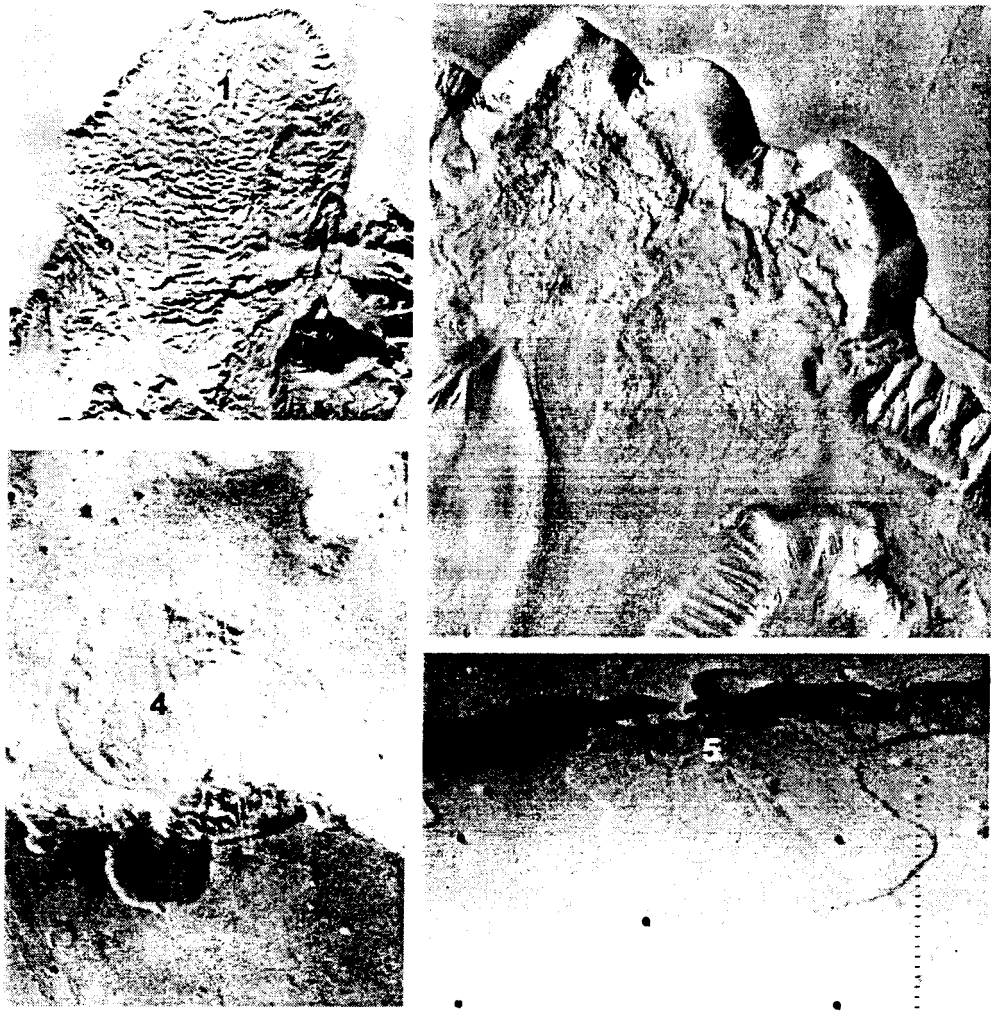


**Figure 3.2(a)** Images of landslides 1 through 5 discussed in the text.

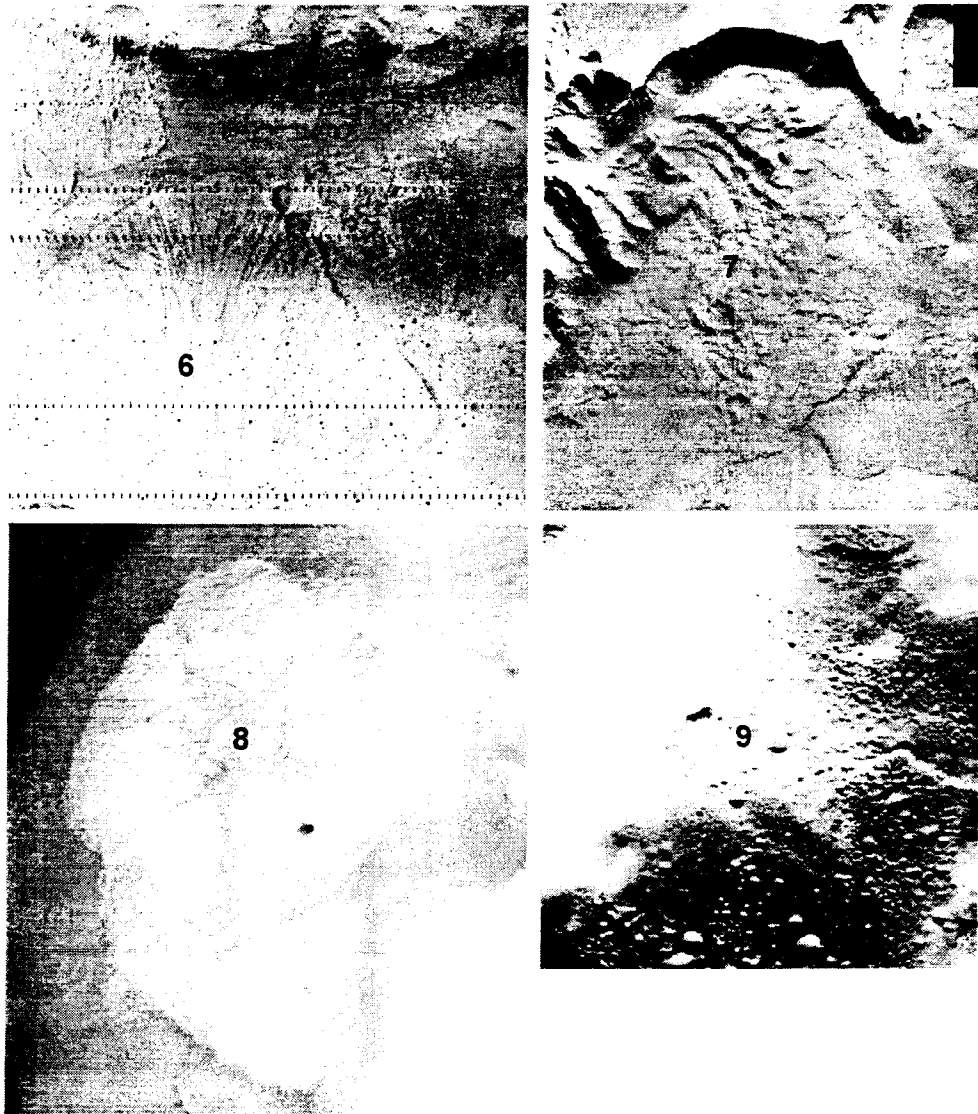


**Figure 3.2(b)** Landslides 6 through 9. Images of Valles Marineris slides (in both parts of this figure) are from the Viking missions, while the Blackhawk image (Slide 1) is from the U.S. Department of Agriculture, the Olympus Mons aureole image (Slide 9) is a bitmap generated from 1/32 by 1/32 degree MOLA data (brightness is proportional to elevation), and the Apollo 17 landslide image (Slide 9) is from NASA.

*Slide 1.* The California Blackhawk landslide (Figure 3.2a) is a terrestrial example of a long-runout landslide (Shreve 1968). With  $V = 0.28 \text{ km}^3$ , it is the smallest slide modeled here. Detailed profiles (Shreve 1968) provided useful information on the shape of the runout path. The lack of an abrupt change in angle between canyon wall and floor typical of Valles Marineris slides makes a wedge-shaped initial mass more appropriate for the Blackhawk slide than the block shape of Figure 3.1.

The general fluidization and Bingham models produce equally satisfactory results (Figure 3.3). The rock mass does not fail frictionally when dry and thus the starting conditions for acoustic fluidization are not met. The factor of safety ( $FS$ ), defined as the ratio of resisting to driving forces, has an average value of 1.33 (failure is expected to occur at  $FS \leq 1$ ), although local values of  $FS$  may be lower (Záruba and Mencil 1982). Therefore the slide may be considered only marginally stable for a friction angle of  $20^\circ$ . A more appropriate measure of failure probability in the context of acoustic fluidization is the highest friction angle that still produces movement at the toe of the initial shape:  $18.9^\circ$  for this model, probably close enough to the baseline value (given its uncertainty) that acoustic fluidization cannot be ruled out altogether if a suitable explanation can be found for such a low friction angle.

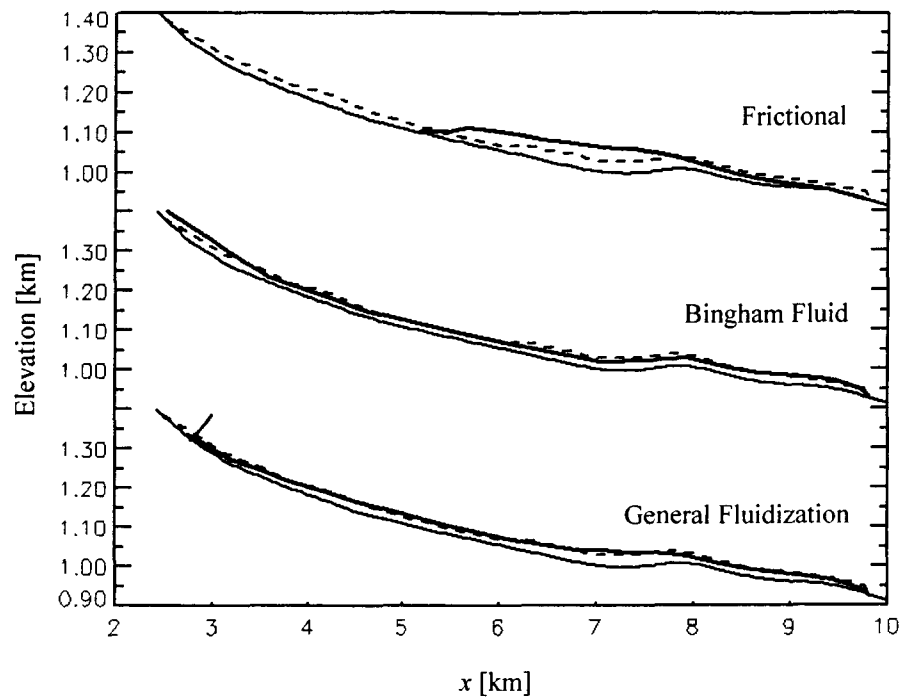


**Figure 3.3** DAN results for Slide 1, the Blackhawk landslide. In each panel, the dashed line is the final profile (measured from *Shreve* (1968) data) and the thin black line is the inferred runout path. The heavy line represents the DAN results using the rheology indicated. The short line at right angles to the runout path in the general fluidization panel marks the position at which the frictional rheology switched over to power law.

A pore-pressure coefficient of 0.27 corresponds to hydrostatic pressure (with rock density of  $2700 \text{ kg.m}^{-3}$  and water density of  $1000 \text{ kg.m}^{-3}$ ), so the values of 0.65 and 0.31 (Table 3.3) required for the frictional and general-fluidization models, respectively, are superhydrostatic. Experiments conducted by *Iverson et al.* (1997) show that on failure, pore pressures may increase by as much as 100 % due to soil compaction. Such an increase raises the pore-pressure coefficient to 0.42, above that required for the general-fluidization model that best matches this slide. Fluid at lithostatic pressure has  $r_u = 0.5$ , so values in excess of this limit are physically impossible, ruling out the viability of purely frictional dynamics for this slide.

slide number	Frictional	Bingham			General Fluidization	Acoustic Fluidization		
	$r_u$	$\tau_0$ (kPa)	$\mu$ (kPa.s)	$\tau_0$ (kPa)	$\mu$ (kPa.s)	$r_u$	$\tau_0$ (kPa)	$\mu$ (kPa.s)
1	0.65	24.5	10	13.5	5.0	0.31	-	-
2	0.56	870	200	135	20	0.49	245	20
3	0.47	790	50	49.5	10	0.35	157	20
4	0.58	265	40	79.0	50	0.29	-	-
5	0.58	75.0	20	21.8	5.0	0.00 ( $\phi = 22.8^\circ$ )	21.8*	5.0*
6	0.71	170	40	65.5	10	0.48	-	-
7	0.58	525	200	145	50	0.41	146	50
8	0.94	50.0	20	49.2	5.0	0.98	-	-
9	0.41	0.50	0.30	1.8	0.50	0.00	1.8*	0.50*

**Table 3.3** Summary of DAN results. Rheologies other than general fluidization produced unequivocal best-fits for only 2 of the 9 slides, and these are indicated by asterisks. The frictional phases of all slides had  $\phi = 20^\circ$ , except where indicated, and for acoustic fluidization  $r_u = 0$  in all cases. Where no data for acoustic fluidization are given, this rheology did not cause the initial mass to fail.

we define rear runout  $L_r$  as the minimum  $x$ -coordinate of the final deposit configuration and front runout  $L_f$  as the maximum  $x$ -coordinate. The rear runout of all Bingham slides is zero because the tapered upper end of the initial mass is, in general, too thin to produce stresses above the yield value. The relative motion of the lower portion of the initial mass thus produces a thin, stretched tail. In DAN, this causes the rear elements of the slide to lengthen significantly and the tail may not always be smoothly resolved – models are run with higher resolutions where necessary.

*Slide 2.* One of the largest landslides considered here, Slide 2 (Figure 3.2a) is situated against the north wall of Ophir Chasma. Three distinct deposits are visible below this wall and Slide 2 is the furthest west. All three deposits have clearly defined tails, but further along their lengths they overlap and are difficult to distinguish. They are, nonetheless, good examples of unconfined long runout landslides. Slide 2 has a front runout of 79 km, a distance ten times that of the initial height of the failed material (Table 3.2).

The frictional and general fluidization rheologies provide comparable fits to the final configuration (Figure 3.4). General fluidization produces better toe and tail shapes, but is less accurate between  $x = 20$  and 40 km. Required pore pressures in both models are high ( $r_u = 0.49$  and 0.56 for the frictional and general-fluidization, respectively); the small difference between the two does, however, span the lithostatic value, perhaps marginally favoring the general fluidization model. Note that the position of the transition from frictional to power law for general fluidization was chosen in this case to coincide with an abrupt decrease in profile slope. The transition position for the acoustic fluidization rheology is, however, further back along the runout path since the initial frictional stage is less energetic without pore pressure and reaches its maximum velocity sooner.

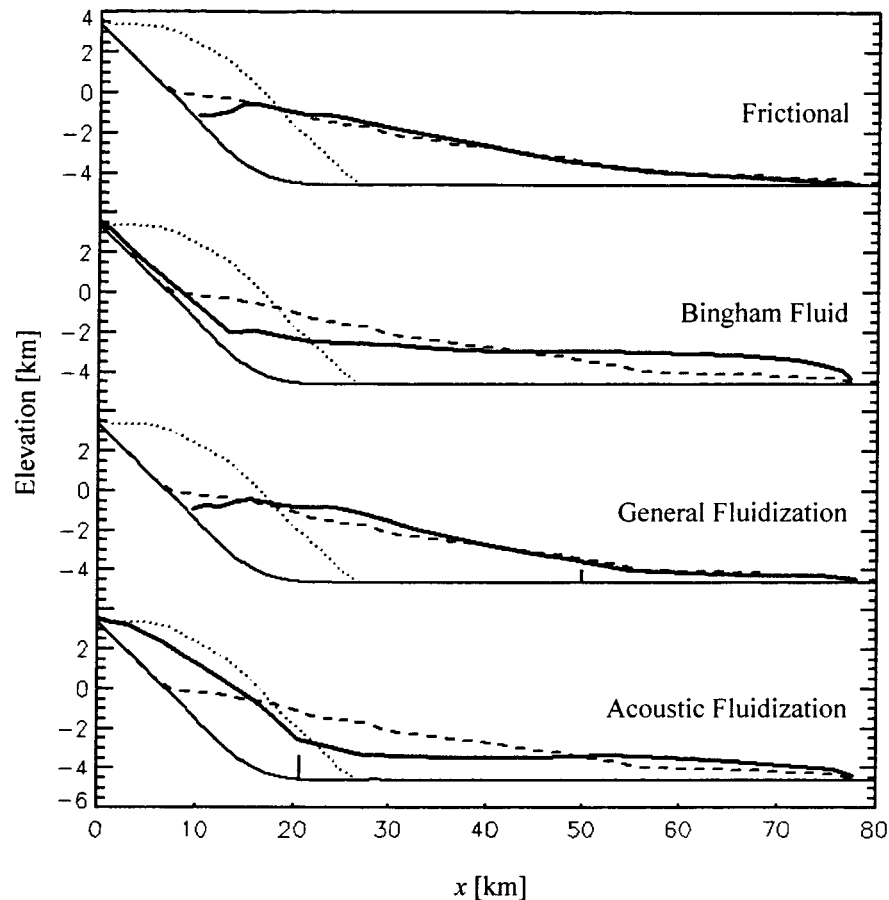


**Figure 3.4** DAN results for Slide 2. The observed final profile (dashed line) is measured from MOLA data. The dotted line is the initial shape of the landslide mass. Note that the runout path and initial shape have rounded corners, a result of DAN's spline routine which generates only smooth curves. Acoustic fluidization is a special case of general fluidization (pore pressure is zero in the frictional stage).

*Slide 3.* This landslide is the furthest east of the North Ophir Chasma slides (Figure 3.2a). Like Slide 2, the scar in the wall of the chasm is clearly contrasted with its surroundings, as is the tail of the deposit, and most deposit dimensions are similar to those of Slide 2 (see Table 3.2). Although both the frictional and general-fluidization rheologies match much of the profile (Figure 3.5;  $x = 20 - 55$  km), only the latter matches the slide tail and the long, thin runout to  $x = 72$  km. Furthermore,

significantly lower pore pressure is required for general fluidization compared to friction ( $r_u = 0.35$  vs.  $0.47$ ). Note that the position of the transition from frictional to power law in the general-fluidization model was also chosen here to coincide with an abrupt decrease in profile slope.

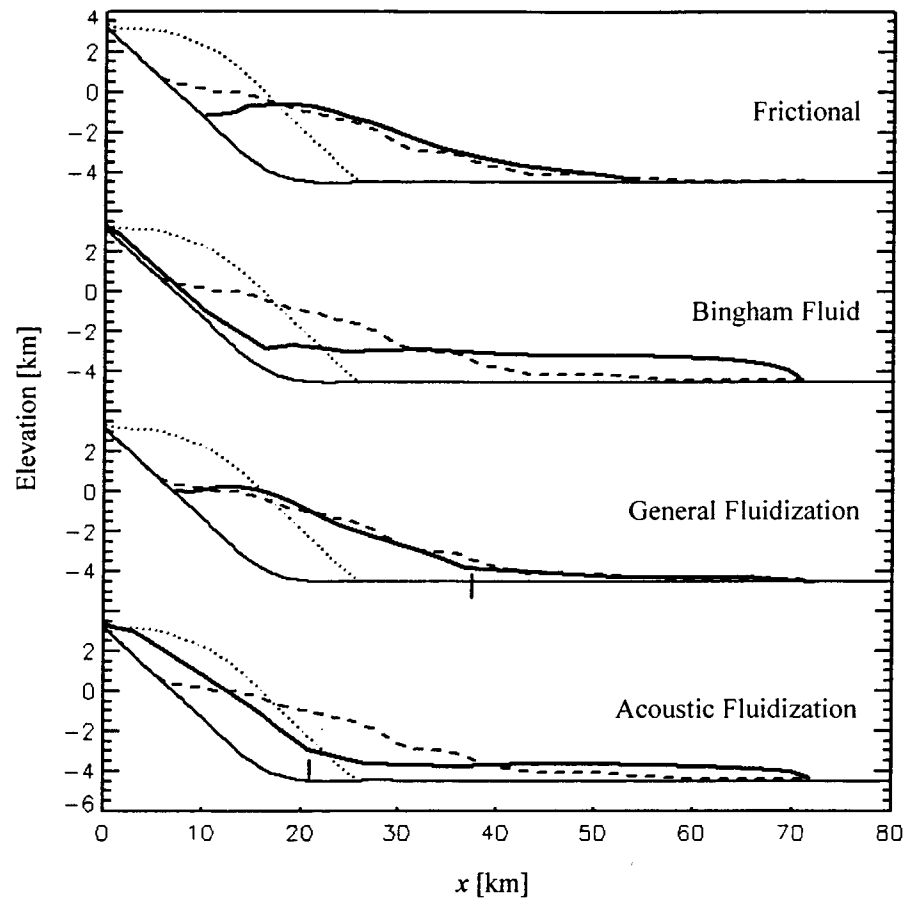


**Figure 3.5** DAN results for Slide 3.

*Slide 4.* This relatively small landslide (number 1 in Lucchitta 1979) is located against the south wall of Gangis Chasma. It is the only slide of those considered here for which MGS Mars Orbiter Camera (MOC) data are available. An image covering the length of the slide (Figure 3.6) reveals detailed structure, including the scar

features described above. The deposit has longitudinal ridges and grooves, and transverse ripple-like structures reminiscent of a turbulent fluid.

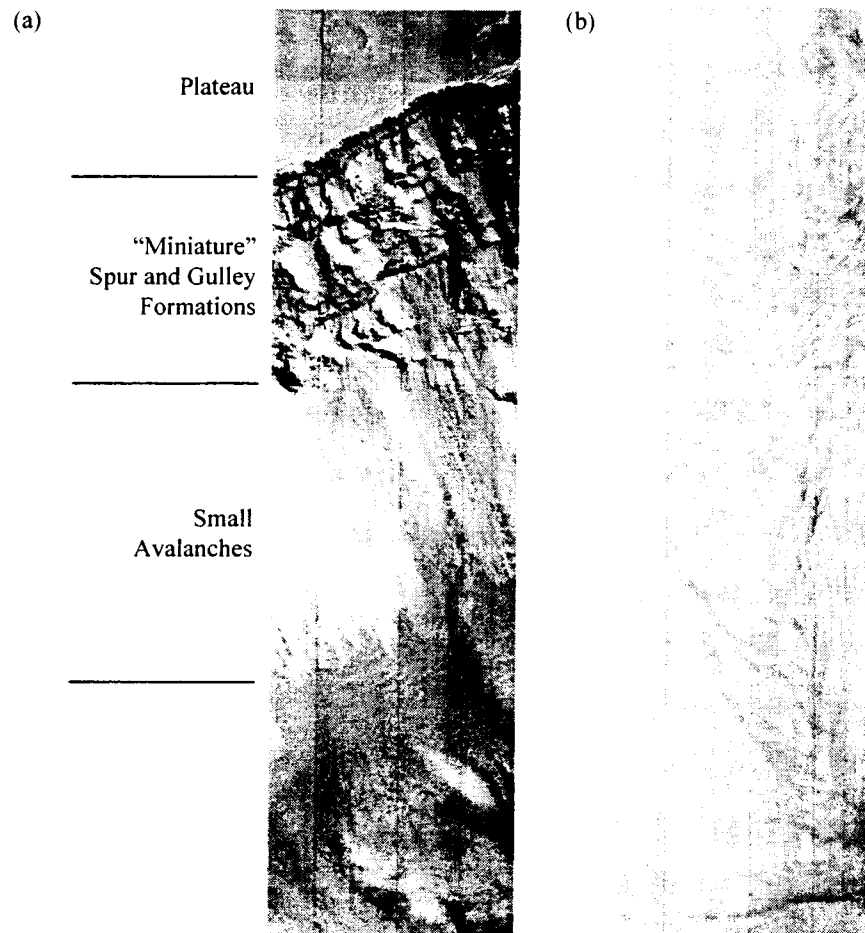


**Figure 3.6** Two parts of a MOC image (M07/03026) oriented along the length of Slide 4. Each part is just under a tenth the length of the original image (whose footprint is visible in Figure 2a). Image width covers approximately 1.5 km. (a) Landslide reentrant with dark upper layer and light talus slopes below. (b) Transverse, ripple like structures reminiscent of turbulent flow. Although the contrast in the entire image has been stretched, the two strips have not been stretched relative to each other.

General fluidization produces the best fit (Figure 3.7) with only modest pore pressure (Table 3.1). The Bingham fluid reproduces the bulbous toe shape, but fails to mimic the tail. Because the structure of the runout path is somewhat simplified, the

apparent deepening of the deposit near the toe might also be interpreted as a constant thickness deposit overlying a bulge in the runout path. Despite the steep initial slope of the runout path, acoustic fluidization does not initiate failure. This is because much of the material lies initially over the level section of the runout path and its weight does not contribute to the downslope driving force. The highest friction angle that produces motion in the toe of the initial shape is  $14.5^\circ$ , significantly less than the baseline value.

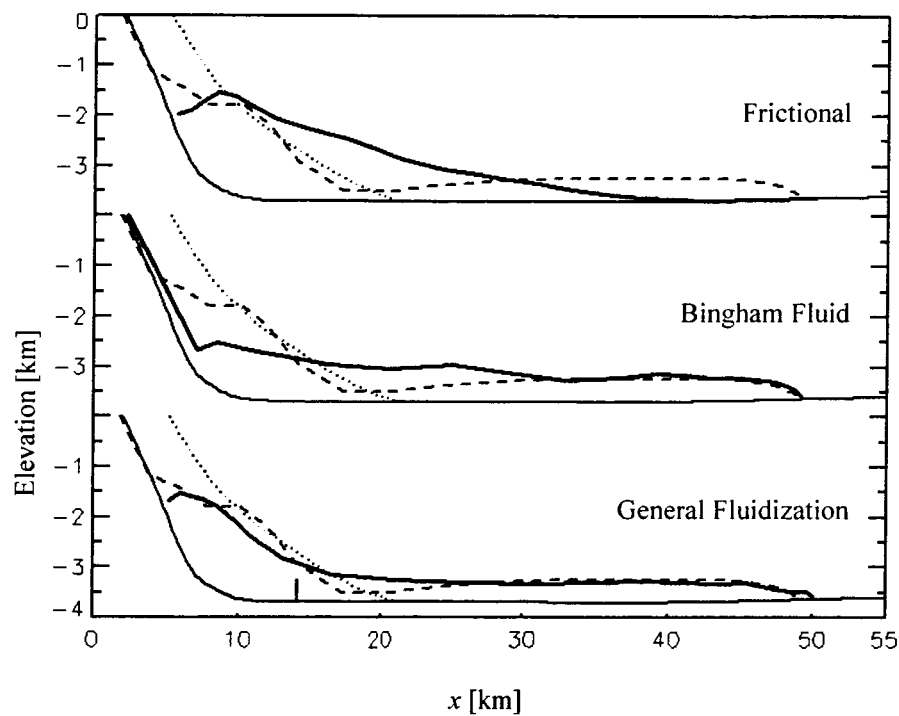


**Figure 3.7** DAN results for Slide 4.

Since the initial and final cross-sectional areas are very similar (Table 3.1), the decrease in area caused by the great degree of widening of the slide (Figure 3.2a) has to be compensated by a high ( $10^7 \text{ m}^3 \cdot \text{m}^{-1}$ ) entrainment rate, which may imply that the canyon wall in this region is weaker than that of the other slides.

*Slide 5.* Situated against the north wall of the eastern reaches of Gangis Chasma, Slide 5 (number 8 in Lucchitta 1979) is the smallest Martian landslide modeled ( $V = 14 \text{ km}^3$ ). The shape of the deposit toe is influenced by its contact with another slide emanating from the opposite canyon wall (Figure 3.2b and 3.8). Consequently it is not surprising that none of the rheologies, except perhaps the Bingham fluid (which was run with 30 slide elements to improve tail resolution), reproduces the narrow hump at the deposit toe. Overall, the acoustic fluidization rheology provides a comparably accurate fit; note that the friction angle had to be increased to  $22.8^\circ$  from the baseline value of  $20^\circ$ . The initial height  $H$  (Table 3.1) of the failed material is not significantly less than that of other Martian landslides, but because the deposit volume is so small, the depth  $D$  of the deposit (Figure 3.1; Table 3.1) is also small. This gives rise to a greater rear runout, hence the reduced need for pore pressure that allows acoustic fluidization to model this slide successfully. In the available Viking images of Slide 5 no obvious scar is visible on the canyon wall and  $H$  was thus chosen to correspond to the full height of the wall, a rule of thumb supported by observations of most other large scale Valles Marineris slides.

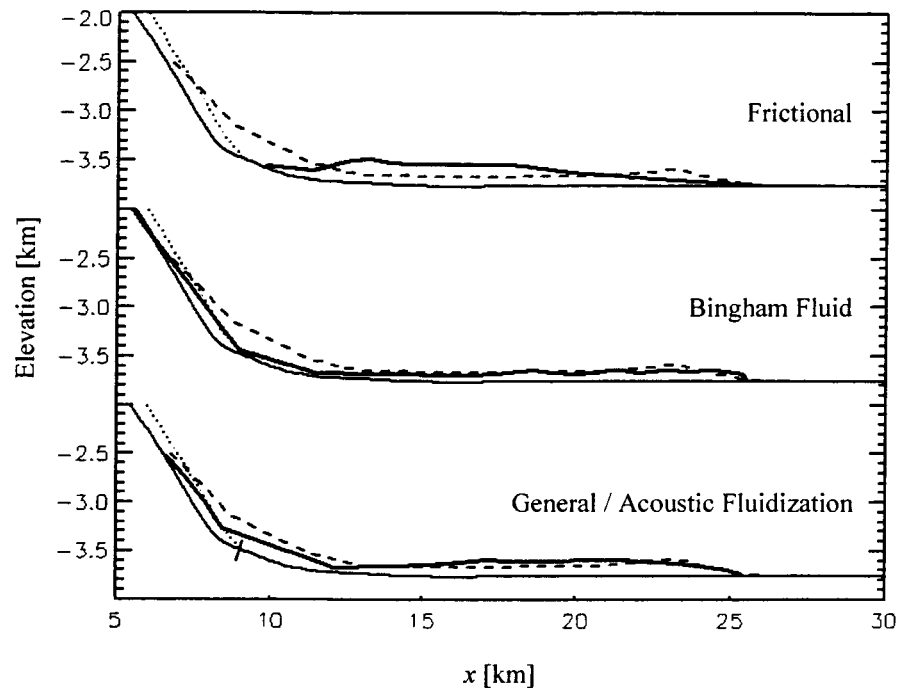


**Figure 3.8** DAN results for Slide 5. The best-fit was acoustic fluidization: introduction of pore pressure made the results less accurate, hence the coincidence of optimized acoustic and general fluidization results.

*Slide 6.* This landslide (Figure 3.2b; number 9 in Lucchitta 1979) is located at the west end of Coprates Chasma. It is a relatively small slide, with a distinctively level, square tail (Figure 3.9). This may be due to the wholesale slipping of the topmost section of the original mass. DAN does not account for the motion of large rigid blocks so the main priority of Slide 6 models was to match front runout. None of the models produces a satisfactory fit. Acoustic fluidization does not initiate failure; the highest friction angle that produces motion in the toe of the initial shape is  $16.3^\circ$  ( $FS = 1.24$ ).

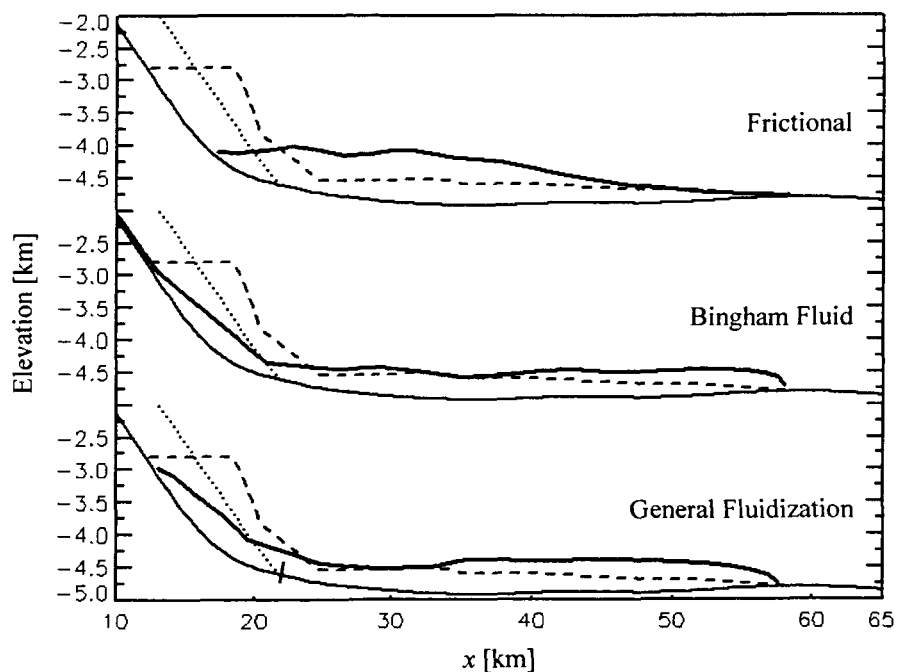


**Figure 3.9** DAN results for Slide 6.

*Slide 7.* Located against a west facing wall in the region between Ophir and Melas Chasma, this slide (Figure 3.2b; number 11 in Lucchitta 1979) is similar in volume and dimension to the north Ophir Chasma slides (Table 3.2), but has a shorter runout. General fluidization, which produces the best fit (Figure 3.10), thus requires a

high yield strength (145 kPa). The required pore-pressure coefficient (0.41) is between hydrostatic and lithostatic values. The frictional rheology also yields a good fit to this profile but requires superlithostatic fluid pressure ( $r_u = 0.56$ ).

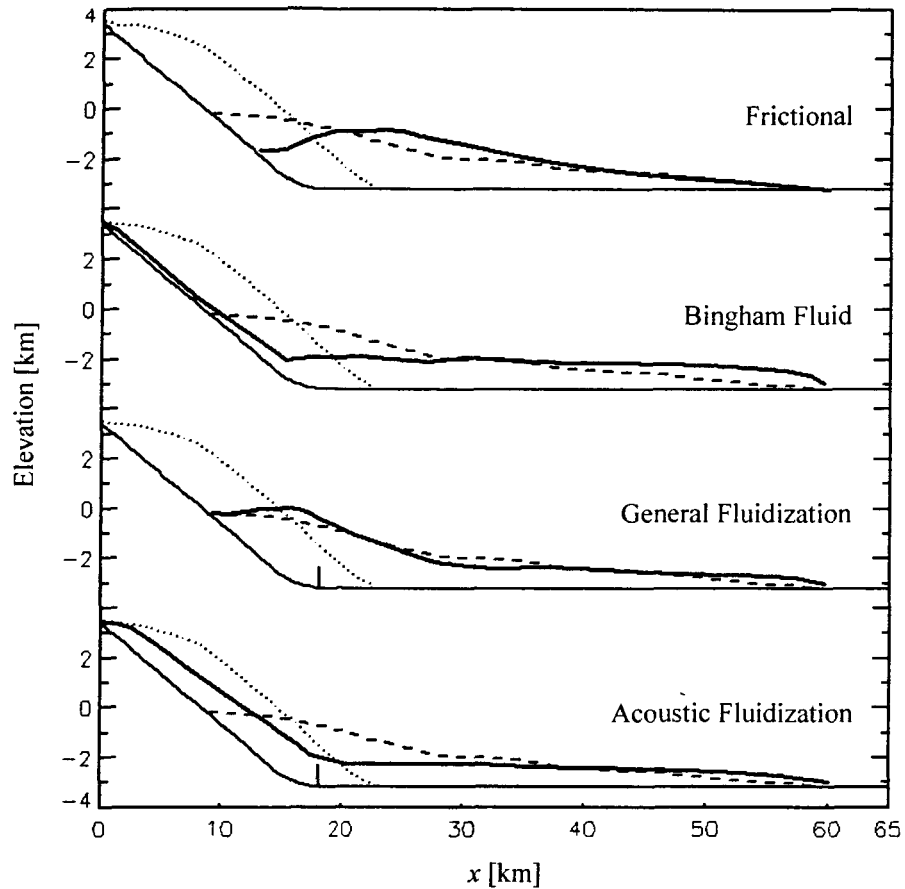


**Figure 3.10** DAN results for Slide 7.

*Slide 8.* we ran a model of the westward facing Olympus Mons aureole deposit. In a bitmap generated from MOLA data (Figure 3.2b), where each picture element has a brightness proportional to its elevation, the deposit can be seen overlying a darker (and therefore lower elevation) deposit. The scarp near the tail of the deposit is assumed to be the landslide scar, and the initial mass is wedge-shaped in order to

simulate the pre-slide shield topography. Post-emplacement plains and surface deposits covering the rear of the aureole make it difficult to infer the deposit configuration in this region, and we thus assume a uniform deposit thickness. Three different profiles were constructed in order to get an overall picture of the aureole topography. The runout path dips towards Olympus Mars proximally, and away from it distally, agreeing with observations by Francis and Wadge (1983). Neither frictional, Bingham, nor general-fluidization models produce particularly good fits (Figure 3.11) and most notably the required pore-pressure coefficients must exceed 0.9 to achieve the 690 km front runout. Failure is not initiated for the dry frictional precursor to acoustic fluidization:  $FS = 2.10$  and the highest friction angle that produces motion in the toe of the initial shape is  $3.8^\circ$ . we conclude that the Olympus Mons aureole is not a landslide deposit but the result of an alternative process such as gravity spreading (Tanaka, 1985).

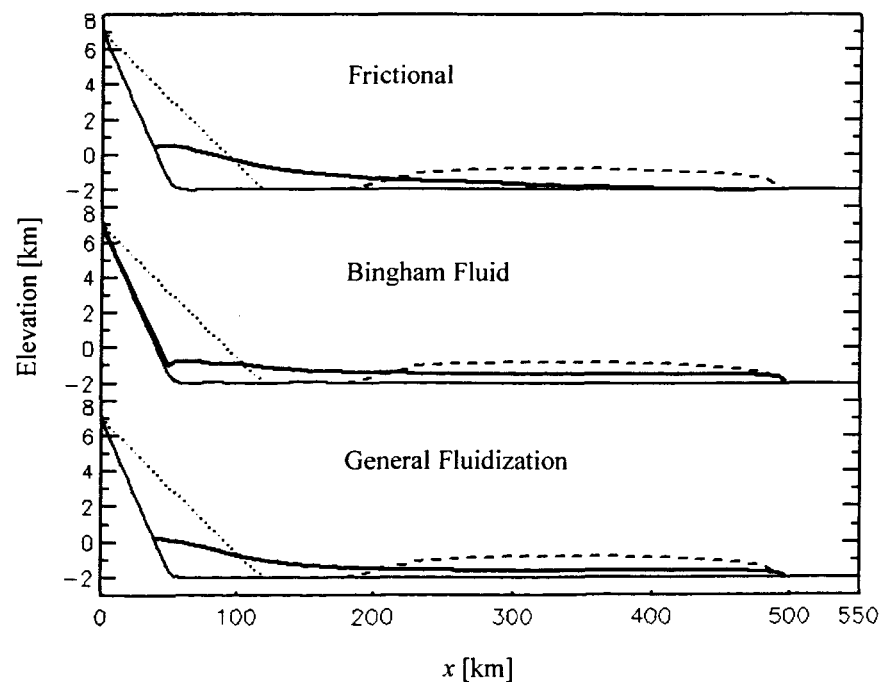


**Figure 3.11** DAN results for Slide 8, the northern Olympus Mons aureole deposit.

*Slide 9.* we modeled a large lunar landslide near the Apollo 17 landing site whose volume is similar to that of the Blackhawk slide (Table 3.2). Although detailed topographic data is unavailable, approximate rear and front runouts (5.0 and 8.8 km) and estimates of average proximal and distal deposit thicknesses (20 and < 10 m) are known (Howard 1973). Since no obvious scar is visible, we assumed that the landslide material initially covered the full height of the mountain massif down which it slid. we did not include width or volume variations in this model. The initial shape is very shallow: with  $D = 22$  m the depth normal to the runout path is only  $22 \sin 24.8^\circ = 8.9$  m (Table 3.1). Since the lunar regolith is 5 to 10 m deep (Quaide and Oberbeck 1973) it is unlikely that bedrock failure was involved.

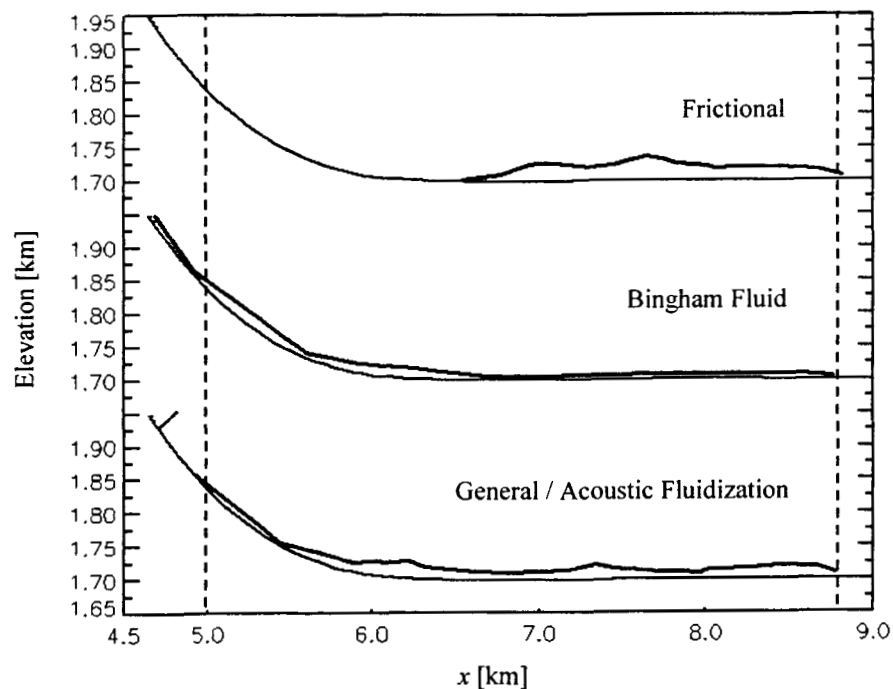


**Figure 3.12** DAN results for Slide 9, the Apollo 17 landslide. No measured final profile is available, but the known required rear and front runouts are marked with vertical dashed lines.

Acoustic fluidization produces the most accurate combination of rear and front runouts (Figure 3.12). This conforms to the clear requirement that lunar landslide “fluidization” must proceed in the absence of a fluid. The introduction of even small pore pressures produces a longer rear runout than required. The frictional rheology requires substantial fluid pressure to achieve the desired front runout ( $r_u = 0.41$ ), confirming the need for a fluidizing process to describe its dynamics.

The small depth of the initial shape requires low yield strengths to promote failure. A simple sliding-block model can be used to estimate yield strength (e.g., McEwen 1989):

$$\tau_0 = \rho g d \sin \beta$$

where  $\rho$  is density,  $g$  is gravitational acceleration,  $d$  is the deposit toe thickness, and  $\beta$  is the slope of the runout path at the deposit toe. Applying appropriate values of these variables, including a slope of  $5^\circ$  (a reasonable upper limit) and a toe depth of 10 m, we obtain a yield strength upper bound of 3.8 kPa, which compares well with values from DAN models (Table 3.3).

As a result, the Bingham rheology produces a deposit thinner than the estimate from Howard (1973) of 10 to 20 m. On the other hand, the frictional rheology produces a short, bunched deposit with a maximum depth of 50 m. Only acoustic fluidization produces the desired depths.

we repeated the simulation with  $H$  reduced to half its original value. With the initial shape occupying only the lower half of the mountain slope, depth  $D$  was doubled to conserve volume. Despite the lower potential energy of the initial mass, acoustic fluidization remained the best rheology. Higher yield strengths were required to maintain the same runout (1.20 kPa for the Bingham rheology and 1.27 kPa for acoustic fluidization).

### 3.4 Discussion and Conclusions

#### 3.4.1 Best overall rheology

The general fluidization rheology is the obvious best-fit for Slides 3 and 4 and can be considered a comparable best-fit for Slides 1, 2, and 7. None of the selected rheologies produces good fits for Slides 6 and 8, which we attribute to the effects of large, discrete blocks and a non-landslide origin, respectively. Acoustic fluidization is the best-fit for Slide 9. For Slide 5 the Bingham rheology is clearly superior to general fluidization, but this slide is compromised by longitudinal confinement.

The advantages of general fluidization can be described by considering the shortcomings of the other rheologies. The frictional rheology has a friction angle ( $20^\circ$ ) close to the failure angle  $\alpha_1$  in many cases (Table 3.2). This limits the reach of the slide, producing small rear and front displacements. Lower friction angles would produce greater runouts but the current choice already constitutes a physically reasonable minimum. Instead, large pore pressures are required to achieve the desired runouts and these frequently exceed the likely maximum (corresponding to  $r_u = 0.42$  as described above). With the exception of the fluidization rheologies in the Olympus Mons aureole model, only the frictional rheology requires superlithostatic pore pressures ( $r_u > 0.5$ ), emphasizing the inability of this rheology to explain long runout landslides (Cleary and Campbell 1993).

The frictional profiles are typified by a linear decrease in deposit thickness in the positive  $x$  direction (if pore pressure is zero, the surface of the deposit comes to rest at the friction angle of the material). Indeed, some of the observed deposit surfaces (e.g. Slides 2, 3, and 7) have linear sections, suggesting that the governing rheology does, at times, exhibit frictional behavior, pointing towards the use of two-stage fluidization processes such as those considered here.

The Bingham rheology consistently fails to produce the correct tail shape, even when model resolution is increased. Toes are frequently too deep, indicating that the yield strength is greater than values calculated directly from deposit thickness (McEwen 1989). Actual yield strengths are likely to be smaller, probably similar to the power law yield strengths obtained by the general fluidization rheology.

The general fluidization parameter values are mostly reasonable, although yield strength and apparent viscosity values are difficult to judge, being poorly constrained (viscosity is probably between 10 and 1000 kPa.s in dry sand, Goetz and Melosh 1980). The pore-pressure coefficient has an average value of 0.40, a physically plausible value given additional pressurization due to soil compaction (Iverson *et al.* 1997). There are at least four potential scenarios in which geologically recent martian landslide formations were lubricated:

1. As noted in the introduction, pore pressures in DAN models refer to conditions at the failure surface and are not representative of the entire deposit. Thus, for a fluid to promote greater runouts, it is not necessary for the initial material to be saturated at all depths, especially for power-law fluidization rheologies in which shear is concentrated in a basal layer. The top 300 to 500 m of near equatorial crust is expected to have been desiccated over the duration of current atmospheric conditions (Fanale *et al.* 1986, Clifford 1993). Since most martian slides have an initial depth of a few kilometers (Table 3.1), a substantial part of their mass may have been saturated with ice at the time of failure. The frictionally dissipated energy produced during the slide event is, however, unlikely to be sufficient to melt ice for lubrication. The energy produced per unit time, per unit mass is  $v g \sin(\alpha_1) F S$  where  $v$  is the depth-averaged downslope velocity of the slide (Iverson *et al.* 1997). we integrated this energy over time for each slide element in dry frictional DAN models and found that on the order of 1 kJ/kg is produced by material on the initial, steep section of the

runout path. For ice at 0 °C, 334 kJ/kg is required for melting, so the supply is two orders of magnitude too small.

2. Alternatively, water may have been present in the liquid phase prior to failure. A cryosphere confining an underlying saturated aquifer, as suggested by Carr (1979) and Clifford (1993), might have a base shallow enough to fall above the landslide failure zone. Reasonable present-day values of crustal thermal conductivity ( $2.0 \text{ W.m}^{-1}.\text{K}^{-1}$ ) and geothermal heat flux ( $30 \text{ mW.m}^{-2}$ ) suggest a melting point depth of 2.3 km at the equator, assuming that melting occurs at 252 K, a likely value given pressure and solute effects (Clifford, 1993). Higher heat flux estimates (e.g.  $45 \text{ mW.m}^{-2}$  from Toksöz 1978) yield depths as low as 1.5 km, within the depth of most Valles Marineris landslides. Notably, of the Valles Marineris slides modeled, only Slide 5 has a depth less than 3 km, and acoustic fluidization is its most successful rheology.

The recent formation of a near-surface water-related gully feature at only 27° latitude (Malin and Edgett 2000) supports the idea of a water table only a few hundred meters deep, but this feature does not preclude the existence of an underlying cryosphere. Other sapping features have been placed contemporaneously with the landslides (Peulvast *et al.* 2001), and near-equatorial outflow channel drainage may have continued well into the Amazonian (Gulick 2001), supporting the idea of water in the Tharsis region at the time of landsliding.

3. If lakes existed in the Valles Marineris (Carr 1996, Lucchitta *et al.* 1994), water may have infiltrated into the walls, providing sufficient pore pressure for later landslide fluidization. Although our principal argument here is for the presence of a fluid for lubrication purposes, water in this scenario might also have been partially responsible for the failure itself. If the Valles Marineris drained in a relatively short period (e.g., via the catastrophic outflow channels in the case of open depressions, and by flow through permeable aquifers in the case of closed depressions) leaving

lacustrine deposits which correspond (at least in part) to the interior layered deposits of the present day, then the newly exposed canyon walls, no longer under pressure from a large body of water and still highly saturated, would be unstable, resulting in widespread landsliding. Lucchitta *et al.* (1994) suggested that the Valles Marineris spur-and-gully formations may have formed subaqueously. They would thus have formed prior to the landslides while the lakes were still in place. This scenario is then in agreement with the observed relative ages of the landslides, spurs and gullies, and the interior layered deposits. Problems with this means of landslide emplacement include the ability of the crust to hold water for a sufficiently long period. With a length scale on the order of 10 km, and a permeability of  $10^{-17} \text{ m}^2$  (a likely crustal lower bound, Harrison and Grimm 2002), a 1 myr period would be available for water-lubricated landslide formation (this is the time scale for diffusive drainage of fluid from an initially saturated aquifer 10 km thick). This is a reasonable lower bound only, and it is likely that landsliding occurred over a longer period (given the sometimes large differences in deposit age, Lucchitta 1979), requiring unreasonably low permeabilities.

4. In the absence of water,  $\text{CO}_2$  may have been a suitable fluidizing agent.

Hoffman (2000) proposed a “white Mars” in which  $\text{CO}_2$  is the principal fluid at work in the catastrophic flood channels which open into the northern highlands.

Depressurization of subsurface  $\text{CO}_2$  liquid causes it to flash into the gaseous phase and mix broken landslide material into a turbulent cloud of dust, rocks, ice, and gas (Hoffman, 2000). Continual degassing of liquid from the landslide mass provides an ongoing source of lubrication. Hsu (1975) simulated the terrestrial Elm landslide with a mixture of silt and dry ice whose degassing did indeed produce long runouts.

we conclude this section by mentioning some aspects of landslide dynamics that may contribute to long runouts but are not simulated in DAN. The rear of many of the

Martian deposits contain unbroken segments of the original landslide mass that have slumped or rolled down the runout path, possibly producing greater rear runout than material composed of uniformly sized small-grained particles. In most cases, these blocks are not sufficiently isolated from smaller grained particles to justify their exclusion from DAN models, with the exception of Slide 6 whose tail has a large level section, indicating that the upper part of the initial mass slipped in one piece down the failure plane. The dynamical influence of large blocks, and possibly other phenomena, may mean that actual pore pressures are somewhat less than those predicted by DAN models, although they are likely to remain non-zero. This effect will be offset by the increase in required pore pressures if higher friction angles are found to be more appropriate.

### *3.4.2 Other Rheologies*

The Bingham rheology produces the best results for Slide 1. A yield strength of 24.5 kPa and a viscosity of 10 kPa.s are, however, significantly smaller than the values used to model rock avalanches (300 kPa and 40 kPa.s respectively, Hungr 1995).

Acoustic fluidization produces the best results for slides 5 and 9. Although these slides are unique in having relatively small values of  $D$ , models of Slide 9 with twice the value of  $D$  (and half the value of  $H$ ) yield the same rheology ranking, indicating that the suitability of acoustic fluidization is determined by other factors such as runout slope.

A geometrical feature of significance in Slides 4 and 8 (and to a lesser extent in slides 2, 3, and 7) is a large initial “footprint”. The part of the initial mass which rests on the horizontal canyon floor does not contribute to the downhill force that promotes movement, leading to shorter runouts which must be compensated by higher pore

pressures or lower yield strengths. Although Slide 4 has a large footprint, its runout path is steeper than that of the other slides, resulting in a relatively good performance by acoustic fluidization.

The long runout of the Olympus Mons aureole is comparable only to submarine landslides, such as those near Hawaii (Moore 1964) which depend on a high degree of lubrication. The shoreline of a northern hemisphere ocean, if one existed at the time of failure, would probably have had a mean elevation of about  $-3800$  m (Head et al 1999) with excursions as high as  $-2000$  m at Tharsis (due to subsequent uplift of the region), which only just coincides with the lowest parts of the aureole deposit. Complete submersion would have required sea levels as high as  $7000$  m. The improbability of submarine formation and the extreme values of many of the DAN parameters suggest that the mode of emplacement was something other than catastrophic landsliding. Favorable alternatives include ice-lubricated gravity spreading (Tanaka 1985), a low strain-rate process that may have acted over a period as long as 1 myr. Spreading may have occurred predominantly along a decoupling zone lubricated by ice that possibly originated from earlier lateral spreading of hydrothermal waters driven by volcanic activity within Olympus Mons (Tanaka 1985).

### 3.4.3 Gravity Effects

The ratio  $H / L_f$  is a useful, although not perfect, measure of the extent to which a landslide runout is “long”. McEwen (1989) and Hsu (1975) provide  $H / L_f$  vs. volume data for Mars and the earth, respectively (Figure 3.13).  $H / L_f$  decreases with volume, meaning that larger landslides have longer runouts relative to their initial height. Also of note is the offset between the Martian and terrestrial trends, evidence that the rheology governing the slides cannot be purely frictional. For a given set of parameter

values, frictional slides produce a constant  $H/L_f$  value independent of  $V$  and gravitational acceleration because the basal resistance scales with gravity and volume and therefore with the downslope acceleration. For the Bingham rheology and the power law part of the fluidization rheologies, the basal resistance does not scale with the downslope acceleration because it is based on a gravity- and volume-independent yield strength. The result is a dependence of  $H/L_f$  on volume and the emergence of separate  $H/L_f$  trends for different gravity environments.

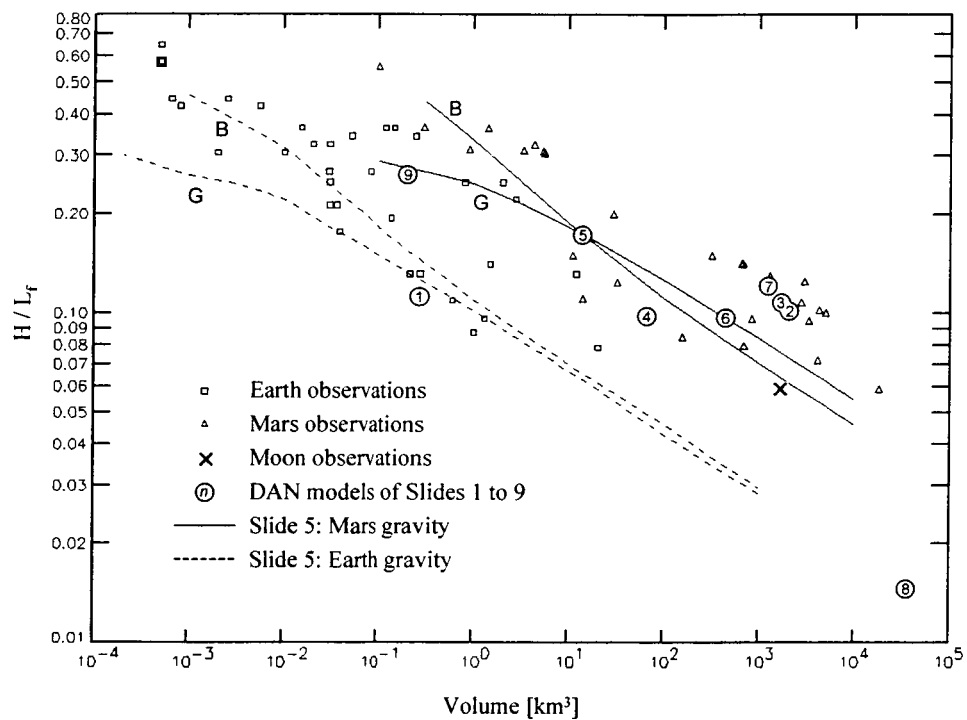


**Figure 3.13** Observed trends in ratio  $H/L_f$  vs.  $V$  for Valles Marineris (McEwen (1989)) and terrestrial and lunar landslides (Hsu (1975)). Values for Slides 1 to 9 are shown with numbered circles. Slides 2 and 3 correspond to two of McEwen's data points but do not coincide exactly with them because of differing volume measurements. Curves generated by simplified DAN models of Slide 5 with varying volume under both terrestrial and martian gravity demonstrate the ability of the Bingham (B) and general fluidization (G) rheologies to mimic the observed trends.

McEwen (1989) recognized the need for a gravity independent yield strength (see also Dade and Huppert 1998) and in Figure 3.13 his point is demonstrated by a set of

DAN models of varying volume, run with both the Bingham and general fluidization rheologies in martian and terrestrial gravity. A uniform width, zero entrainment version of the Slide 5 DAN model was scaled spatially to obtain slides of different volumes but identical aspect ratio ( $D/H$ ). The rheological parameter values that produced the required front runout in the original scale were used for all other scales on both planets, reflecting the assumption that yield strength and viscosity are independent of gravitational acceleration. Slide 5 has a fairly low yield strength: experiments with higher yield strength slides (such as Slide 2) show that the curves in Figure 3.12 shift upwards together without significantly changing their offset. Note that the symbol representing Slide 5 (Figure 3.13) falls over the intersection of the two solid curves at  $V = 14 \text{ km}^3$ , implying that both sets of rheological parameters were chosen so that  $L_f$ , and therefore  $H / L_f$ , coincide at the original scale.

The Bingham and fluidization rheologies reproduce the first-order features of the observed trends extremely well. The general fluidization curves level out with decreasing volume because the efficiency of the power law stage decreases (the yield strength remains constant while the thickness of the deposit decreases), and the frictional stage becomes the dominant influence on runout. This departure reflects the fact that fluidization is unlikely to occur at low volumes (relative to a specific gravitational acceleration). The suitability of the Bingham rheology is also somewhat restricted: it does not initiate failure for volumes below about  $0.2 \text{ km}^3$  for Martian slides and  $0.001 \text{ km}^3$  for terrestrial slides. It must be remembered that all the curves in Figure 3.13 were generated with one set of rheological parameter values. It is physically unlikely, however, that every martian landslide can be described by the same parameter values. There will be a dependence on grain size, rock or soil density, fracture distribution, and other local phenomena. Parameter variations are also evident in the DAN results, although these may be exacerbated by the simplified

nature of the model that excludes small scale, unobservable variations in failure geometry, and other second order effects. Overall, Figure 3.13 provides further support for McEwen's claim of a gravity independent yield strength, and extends it to general and acoustic fluidization, processes which include the frictional rheology (which alone cannot account for the observed trends).

The west Olympus Mons aureole (Slide 8, Figure 3.13) lies well below the Bingham and general fluidization trends for Mars. This reflects its unusually long runout (hence low  $H/L_f$ ) which our rheologies were only able to reproduce with high pore pressures and/or low yield strengths. The Blackhawk landslide (Slide 1) is noticeable as the only data point lying close to the terrestrial trend, as expected. Its position relative to the curves generated by Slide 5 parameter values is a combination of lower yield strength (which lowers  $H/L_f$ ) and higher aspect ratio (which raises  $H/L_f$ ) than Slide 5. The Apollo 17 landslide (Slide 9) lies between the terrestrial and martian trends in Figure 3.13. Because the moon has the lowest gravitational acceleration of the three bodies, its landslides might be expected to lie above the martian trend (vertically separated by about 2.3, the ratio of martian and lunar gravities); however Slide 9 falls below this trend. At least two factors may have affected its value of  $H/L_f$ : 1) impacts responsible for the initial failure may have contributed energy to the subsequent motion, resulting in longer runouts than expected (this may have affected other lunar slides close to impact craters, such as the Tsiolkovsky landslide (Wu *et al.* 1972, Guest 1971, Figure 3.13), and 2) the slide is probably an avalanche of regolith material (which is as deep as 15 m in places, Quaide and Oberbeck 1973) and not a bedrock landslide.

## CHAPTER 4

### OUTFLOW CHANNELS

#### 4.1. Introduction

On Mars, the best evidence for groundwater flow probably lies in the outflow channels, structures larger than any terrestrial flood-related features, with lengths and widths on the order of hundreds of kilometers (Sharp and Malin, 1975; Carr, 1996). Two-thirds of all outflow channels are located around the Tharsis rise, with almost all of these debauching into Chryse Planitia (19/30 and 16/19, respectively, using the tabulation of Clifford and Parker, 2001). The source-region structure of the channels suggests the release of groundwater following the local disruption of a frozen cryosphere (Carr, 1979). Circum-Chryse outflow formation began some time after the end of heavy bombardment 3.8 Gyr ago (Tanaka, 1992; Carr, 1996) continuing to the end of the Hesperian 2.9 to 3.3 Gyr ago (Hartmann and Neukum, 2001; see Clifford and Parker, 2001). Flow may have been catastrophic (Baker and Milton, 1974), with flooding lasting from a few days (e.g. Carr, 1996) to years (Williams and Phillips, 2000; de Hon *et al.*, 2003), possibly in several episodes (Scott and Dohm, 1990; Williams and Phillips, 2000).

A fully consistent description of outflow channel formation remains elusive primarily because of the difficulty in explaining the large volumes of water involved and the required flow rates. At least  $6 \times 10^6 \text{ km}^3$  (Carr, 1996) are thought to have passed through the circum-Chryse channels; however, such estimates require specification of the volume of water required to remove a unit volume of sediment (the sediment-to-water ratio), but this parameter is poorly constrained. Komar (1980) suggests values as high as 0.67 for the large outflows such as Kasei, whereas de Hon

et al. (2003) suggest values as low as  $10^{-4}$  for smaller channels such as Maumee and Vedra Valles.

Estimated flow rates range from  $3 \times 10^6$  m<sup>3</sup>/s (Williams *et al.*, 2000) to  $10^{10}$  m<sup>3</sup>/s (Carr, 1996; Mosangini and Komatsu, 1998). The lower values in this range might be explained by Darcy flow through a porous medium under high pressures. Carr (1979) considered the disruption of a cryosphere due to lithostatic pore pressures, showing that permeabilities as high as  $3 \times 10^9$  m<sup>2</sup> are required to achieve flow rates of  $10^6$  m.s<sup>-1</sup>. Such permeabilities are comparable to the highest measured terrestrial values (Robertson, 1974) and are about an order of magnitude greater than typical high permeability rocks such as Hawaiian volcanics (Davis, 1969). Because Darcy flow through a porous medium of moderate permeability and porosity might not be able to sustain such high flow rates (Head *et al.*, 2003), water drawn from distal parts of the aquifer might have to be stored in a local, highly permeable “buffer” or reservoir ready to deliver high flow rates. The most likely candidates are the Valles Marineris, which may have held ice-covered lakes (Squyres, 1989; Lucchitta *et al.*, 1994), possibly containing enough water to explain the required discharge volumes. Alternatively, the detailed analysis of channel geometry with high resolution images (e.g. Williams and Phillips, 2003) may continue to suggest lower flow rates than previously thought, obviating the need for a local reservoir.

While the local geologic and hydrologic properties of the outflow source regions are complex and still largely unknown, the regional-to-global aspects of outflow formation - which are controlled by the interaction between groundwater flow, storage, recharge, and discharge - are easier to address. In particular, we look at the role of groundwater flow in circum-Chryse outflow channel formation, starting with the work of Clifford (1993), and Clifford and Parker (2001), henceforth named C&P, who present a hydrologic model explaining outflow channel and south polar cap

formation. The model starts during the Noachian with a relatively warm atmosphere and high geothermal heat flux ( $95 \text{ mW}\cdot\text{m}^{-2}$ , C&P), conditions that allow unconfined groundwater flow. The inevitable result, according to C&P, is net groundwater flow toward the low elevations of the northern hemisphere, where an ocean develops. During the late Noachian the atmosphere begins to thin and cool, the northern ocean starts to freeze, and ice sublimates from its surface, moving to the south pole where it condenses as ice onto a polar cap. The subsequent growth of the cap causes the local melting isotherm to rise until it intersects the crustal surface. At this stage, the base of the cap begins to melt and water seeps into the crust, forming a groundwater mound which drives flow toward lower latitudes, raising global water table levels and providing a source for the outflow channels. Meanwhile, the cooling atmosphere is accompanied by the development of a cryosphere which becomes thick enough to confine the global aquifer and, when locally disrupted, gives rise to catastrophic outflows.

Here we defer analysis of Noachian conditions and focus on Hesperian groundwater dynamics. We test the C&P south pole recharge model and an alternative source of groundwater recharge and hydraulic head for the circum-Chryse outflows: Tharsis.

Tharsis has been the primary center of volcanism throughout Martian history and many workers argue for a causal relationship between Tharsis volcanism and outflow channel formation (Masursky, 1986; Tanaka and Chapman, 1990; Head and Wilson, 2001; Chapman and Tanaka, 2002). Heat may have thinned the cryosphere (Tanaka *et al.*, 2002), perhaps melting it through in places (Wilson and Head, 2002). McKenzie and Nimmo (1998) go further to suggest that dike intrusions were responsible for the formation of the Valles Marineris and attendant cryosphere melting and outflow discharge.

The role of equatorial volatiles in outflow formation extends to the atmosphere and centers around variations in the planetary obliquity (tilt of rotation axis relative to the ecliptic). The current value of  $25^\circ$  leads to average annual temperatures about 60 K warmer in the tropics than at the poles. However, the obliquity varies periodically on a scale of about 0.1 Myr (Ward, 1992) and is thought to have reached values as high as  $60^\circ$  (Laskar and Robutel, 1993; Touma and Wisdom, 1993). The effects of high obliquity on climate are profound and include the development of a cold equatorial zone in which surface ice is perennially stable (Jakosky and Carr, 1985; Mischna *et al.*, 2003; Haberle *et al.*, 2003; Richardson and Wilson, 2002). It has been suggested that equatorial ice could, at high obliquity, be sourced by water sublimated from the poles (Jakosky and Carr, 1985; Coleman and Dinwiddie, 2003; Coleman *et al.*, 2003; Mischna *et al.*, 2003; Mischna, personal communication; Mellon *et al.*, 1997; Haberle *et al.*, 2000) and be preferentially deposited over regions of high topographic elevation (Mischna *et al.*, 2003) in analogy to the earth. The low latitude and high elevation of the Tharsis rise make it a good candidate for precipitation at high obliquity. Indeed, much evidence of mid- to high-latitude ice remains today, including shallow subsurface traces detected by the Mars Odyssey Gamma Ray Spectrometer (Boynton *et al.*, 2002), ice-rich layered deposits from recent ice ages (Mustard *et al.*, 2001 and 2003), and gullies possibly formed by melting snow transported from polar to mid-latitudes during high obliquity (Christensen, 2003). Ice-related features are also observed at low-to mid-latitudes and include rootless cones indicative of volcano-ice interactions (Greeley and Fagents, 2001), rampart craters (Allen, 1979), and glacial landforms flanking volcanic edifices (Head and Marchant, 2003).

In the sections ahead we bring to light problematic aspects of the C&P model, and we infer from the evidence given above that groundwater recharge over Tharsis

constitutes a preferable alternative to South Pole recharge. We support our argument with numerical simulations that test and compare both models.

## 4.2. Model

### 4.2.1 MODFLOW-2000

We simulate saturated groundwater flow with MODFLOW-2000 (Harbaugh *et al.*, 2000), a recent version of the well-established model of the United States Geological Survey. The code performs three-dimensional transient groundwater simulations, solving the governing equations for porous media flow on a discrete finite-difference grid. Because thermal effects are ignored, a complete description of the behavior of the system is possible with a single partial differential equation in the hydraulic head  $h$ :

$$\nabla \cdot (\mathbf{K} \cdot \nabla h) + Q = S_s \frac{\partial h}{\partial t} \quad (4.1)$$

where  $\mathbf{K}$  is the hydraulic conductivity tensor,  $Q$  comprises sources and sinks,  $S_s$  is the specific storage of the porous medium, and  $t$  is time. The hydraulic conductivity, which in the models of this work is generally heterogeneous (but isotropic), is related to other properties of the porous medium and its fluid as follows

$$\mathbf{K} = \frac{\mathbf{k} \rho g}{\mu} \quad (4.2)$$

where  $\mathbf{k}$  is the permeability of the medium,  $\rho$  is the fluid density ( $1000 \text{ kg.m}^{-3}$ ),  $g$  is the Martian gravitational acceleration ( $3.71 \text{ m.s}^{-2}$ ), and  $\mu$  is the dynamic viscosity of

the fluid ( $10^{-3}$  Pa.s). The source term  $Q$  consists of surface recharge and drainage, described in detail below.

Permeability, while isotropic, varies with depth according to globally assimilated terrestrial measurements (Manning and Ingebritsen, 1999), and is scaled to the Martian environment by multiplying depth by the ratio of Martian and terrestrial gravitational accelerations (C&P,  $g_M/g_E = 3.7/9.8$ ):

$$\log k = -12.65 - 3.2 \log z \quad (4.3)$$

where  $z$  is the depth in km.

We consider two porosity relationships. The first, used by C&P, is Athy's Law (1930) scaled from lunar seismic data (Binder and Lange, 1980):

$$n = n_0 \exp(-z/2.82). \quad (4.4)$$

where  $n_0$  is the surface porosity.

The second relationship is based on the Kozeny-Carman equation (Ingebritsen and Sanford, 1998) which relates porosity and permeability. We use the following version modified for vesicular basalts (Saar and Manga, 1999):

$$k = An^4$$

where  $A = 8.9 \times 10^{-7} \text{ m}^2$  contains information regarding the tortuosity, shape, and specific surface area of vesicular basalt porosity. Using the porosity-depth

relationship of Equation 4.3, we have

$$\log n = -1.650 - 0.8 \log z . \quad (4.5)$$

The specific storage coefficient  $S_s$  in Equation 4.1 controls, under confined conditions, the volume of water released from the aquifer due to compression of the rock matrix per unit increase in hydraulic head. For water released under unconfined conditions, the porosity of the rock must be taken into account and the storage formulation is best expressed in terms of the storativity:

$$S = S_y + bS_s . \quad (4.6)$$

Here  $b$  is the thickness of the saturated portion of the aquifer and  $S_y$  is the specific yield (that part of the pore space that can be drained, and therefore approximately equal to the porosity). Commonly the specific yield is used on its own under unconfined conditions (Fetter, 1994) since it is generally much larger than  $bS_s$  - this is the approach MODFLOW-2000 adopts.

#### *4.2.2 Boundary Conditions*

The elevation of the upper model boundary corresponds to the roof of the Martian aquifer, and depends both on the topography and the cryosphere thickness. The topography is taken from Mars Global Surveyor MOLA data and therefore assumed to be that of Mars at present, with minor modifications. This assumption can be cast as a statistical argument, that the hypsogram of Mars during the past is approximately that of the present (C&P). However, there is direct evidence that the bulk of the Tharsis rise was in place by the end of the Noachian (Phillips et al., 2001), and

therefore the overall topography of Mars has changed very little since then. We remove the large Amazonian shield volcanoes (Olympus Mons, Tharsis Montes, Alba Patera, Elysium Mons) because their high elevations would artificially influence Hesperian hydraulic heads. Cryosphere thickness is determined by the surface temperatures and geothermal heat flux being simulated, and on an assumed melting temperature of 252 K (C&P). The lower model boundary is 8.5 km below the surface, corresponding to the depth of pore space compaction assumed by C&P, determined by a porosity of 1% in Equation 4.4. The alternative relationship of Equation 4.5, however, falls more steeply than Equation 4.4, reaching 1% at 2.7 km, so for models using this porosity relationship we relax the somewhat conservative threshold of C&P, maintaining a depth of 8.5 km, corresponding to a compaction porosity of  $n = 0.4\%$ . Integration of hydraulic conductivity with depth in an aquifer with a 3 km thick cryosphere (the average thickness for latitudes between  $-30^\circ$  and  $30^\circ$  in model 2) shows that 91% of the flow in the tropics is expected to occur in the top 8.5 km of crust, so the flow here will not be affected by the presence of the compaction threshold. At the poles, the thicker cryosphere results in a smaller fraction (50%) of the total flow above a depth of 8.5 km, and the compaction threshold will thus have a moderate effect on the local flow.

All models have six layers whose thicknesses increase with depth, allowing the steep gradient of the permeability and porosity at shallow depths to be modeled accurately while keeping the number of layers, and thus the computational overhead, small. The models are cast in an equal-area sinusoidal projection to conserve mass and reduce distortion at the poles. Areal coverage of each finite difference cell is  $2800 \text{ km}^2$ .

The left and right model boundaries follow a longitude of  $180^\circ$  (East) along which the only major topographical variation is the dichotomy boundary whose steepest

gradient is oriented approximately S-N, making this longitude a suitable artificial no-flow boundary as flow lines will tend to align with it.

We assume that the Valles Marineris crust is in thermal equilibrium with the atmosphere and therefore has a cryosphere thickness similar to that of the nearby crust, i.e. we do not allow leakage of water through the Valles Marineris walls to produce lakes. The model is transient and run for 900 Myr, corresponding to the period between the end of heavy bombardment (3.8 Gyr, Tanaka *et al.*, 1992) and the lower bound on the Hesperian-Amazonian boundary (2.9 Gyr, Hartmann and Neukum, 2001). Initial head is taken to correspond to the aquifer surface, representing an abrupt end to the Noachian with instantaneous freezing of the cryosphere.

Source Region	Source Volume $10^4 \text{ km}^3$	Associated Valleys	Additional Volume $10^4 \text{ km}^3$	Total Volume $10^4 \text{ km}^3$	Total Water Volume* $10^4 \text{ km}^3$
1. Aram Chaos	2.8	-	-	2.8	4.20
2. Aromatum Chaos	4.5	Shabaltana	-	4.5	6.75
3. Aureum-Arsinoes Chaos	13.2	Simud, Tiu	27.2	40.4	60.6
4. Echus Chasma	53.5	Kasei	36.9	90.4	136
5. Hydaspis Chaos	4.5	Tiu	8.7	13.2	19.8
6. Hydraotes Chaos	11.7	Simud, Tiu	11.7	23.4	35.1
7. Iani Chaos	3.2	Ares	9.5	12.7	19.1
8. Juventae Chasma	3.8	Maja	3.3	7.1	10.7
9. Margaritifer Chaos	2.3	-	-	2.3	3.45
				Total:	296

\* Sediment-water ratio = 0.67

**Table 4.1.** Outflow sources used in MODFLOW models, and their associated valleys, with the approximate volume of material removed from each.

The regional surface recharge is a free parameter and is applied at a rate of  $2 \times 10^{-10}$  m/s (6.3 mm.yr<sup>-1</sup>) for all models, corresponding to estimated south polar ice cap basal melting rates of C&P. Recharge elevation coincides with the Martian surface, a consequence of local cryosphere melting due either to the insulation of an overlying ice sheet, or the proximity of volcanic heat sources (see Discussion). Excess recharge is free to drain from the model. Water is also allowed to exit through those parts of the upper model boundary corresponding to the circum-Chryse outflow channel sources. We assume that discharge occurs because of a disruption in the cryosphere and that water is consequently released from the aquifer at an elevation corresponding to the pre-disruption cryosphere base. We model the largest nine outflow channel sources: Juventae Chasma, Echus Chasma, Margaritifer Chaos, Iani Chaos, Aram Chaos, Hydaspis Chaos, Hydraotes Chaos, Aureum-Arsinoes Chaos, and Aromatum Chaos (Table 4.1, Figure 4.1). The volume of material removed from each source region and its associated outflow channel(s) is taken from Carr (1996). The volume of water required to transport this material is determined by the sediment-volume ratio. Komar (1980) applied to the large outflow channels a set of well-known terrestrial criteria for determining the grain size of different types of stream load. He concluded that the outflow channel morphology, coupled with the effects of the reduced Martian gravity on water and grain-settling velocities, produced sediment loads in the region of 40% by volume (equivalent to a volumetric sediment-water ratio of 0.67), similar to values reported for rivers in the semi-arid southwestern United States (Beverage and Culbertson, 1964). We thus adopt a sediment-water ratio of 0.67 (Table 4.1), but consider it an upper limit. Later we present scaling relationships that estimate outflow discharge given smaller values.

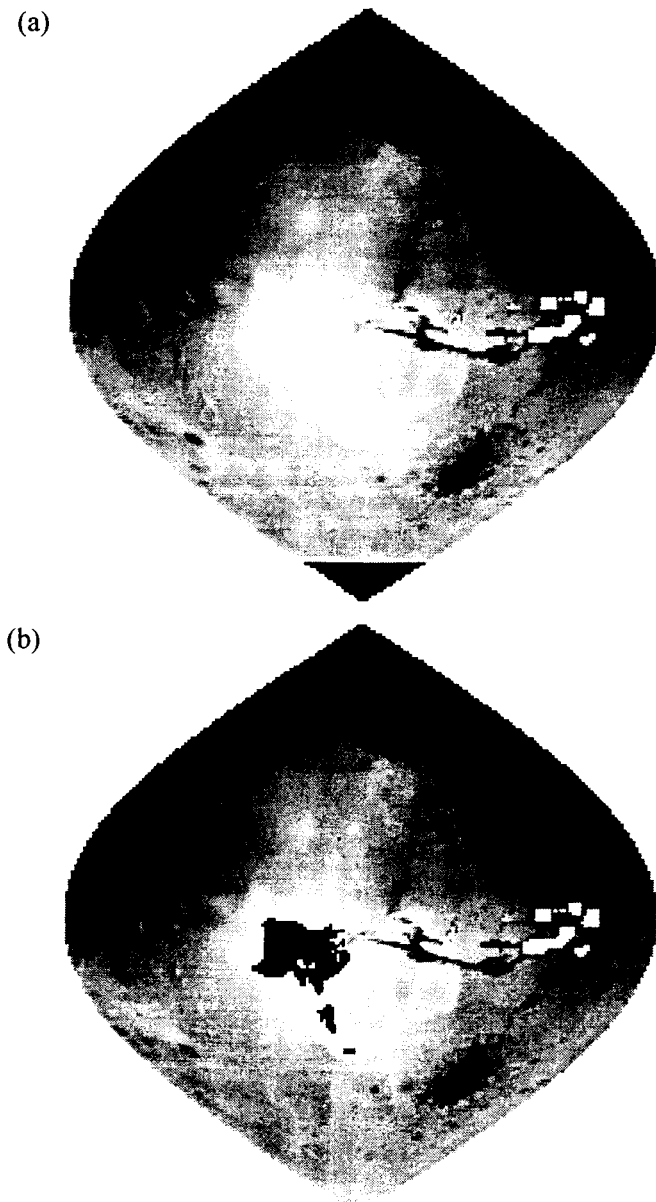


**Figure 4.4** Model topography cast in an equal-area sinusoidal projection spanning longitudes from 180° W to 0°, and all latitudes. (a) South Pole and (b) Tharsis recharge regions are shown in black and modeled outflow channel sources are shown in white.

We adopt a conservative approach in determining discharge requirements, modeling the main chaos regions but only two Chasmata, specifically Echus and

Juventae, from which sediment was carried along single obvious channel pathways (Kasei and Maja Valles, respectively). We do not include water required to remove material from the other large Chasmata since it is unclear what proportions of this water were distributed to particular outflow channels and through the aquifer between chasmata. We thus account for about half ( $3 \times 10^6 \text{ km}^3$ , Table 4.1) the total discharge estimated to have passed through the circum-Chryse outflow channels, a small decrease considering the orders of magnitude uncertainty in sediment-water ratio.

All outflow sources are assumed to begin discharging simultaneously at the start of the model. This simplification, while not entirely physically realistic, measures the ability of the recharge region to provide the necessary discharge to a fully active Chryse outflow region. It also provides some insight into the interaction between outflow sources and how water is shared between them.

#### *4.2.3 Recharge and Thermal Properties*

We examine three models, each with a different combination of thermal properties and recharge location. In our nominal South Pole recharge model (model 1) we adopt the C&P cryosphere thickness derived from an estimate of  $95 \text{ mW.m}^{-2}$  for the Hesperian heat flux (Figure 4.2), which in turn was derived from a parameterized-convection global thermal model (Stevenson *et al.*, 1983). Annually averaged surface temperatures correspond to insolation at the current obliquity and vary from 154 K at the pole to 210 K at the equator. Porosity varies with depth according to Equation 4.4, with a surface value of 20% (C&P). Surface recharge occurs everywhere within 750 km of the south pole (C&P, Figure 4.1) and since basal melting precludes the presence of a cryosphere beneath the ice cap, recharge is applied to the crustal surface.

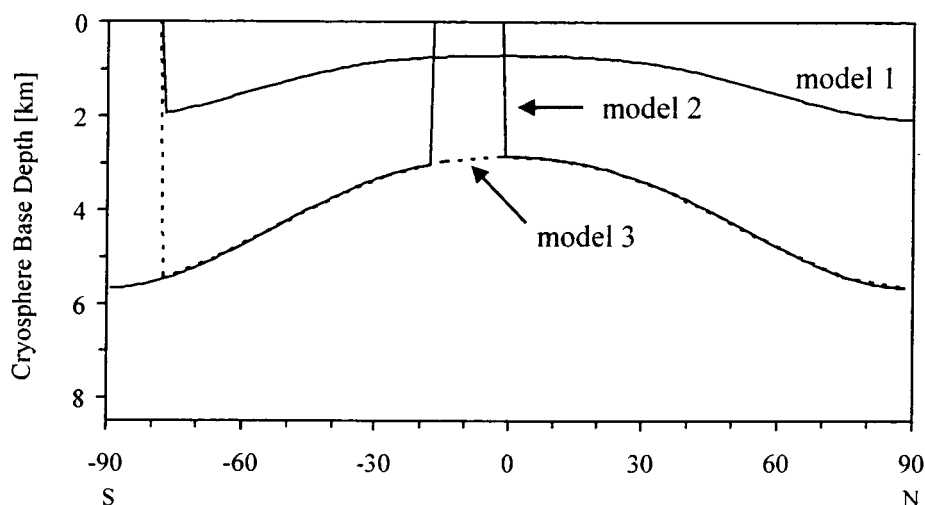


**Figure 4.5** Latitudinal dependence of cryosphere base depth for the hydrologic and thermal conditions adopted in models 1, 2 and 3. The region of zero cryosphere thickness in models 1 and 3 represents basal melting of a polar ice cap, which requires the melting isotherm to reach the surface. In model 2, zero cryosphere thickness (whose lateral extent in this plot corresponds to a longitude of  $245^\circ$ ) is achieved by basal melting or volcanic heating (see Discussion). The effects of the adiabatic lapse rate in models 2 and 3 are not shown here, since they depend on topography. The lower model boundary corresponds to a depth of 8.5 km in all models.

Our Tharsis Recharge model (model 2) tests the ability of Tharsis recharge to provide outflow channel discharge, including more conservative assumptions than in model 1. It covers the same hemisphere as the nominal model, with the same lateral discretization. The assumed Hesperian heat flow of  $30 \text{ mW.m}^{-2}$  is the mean value derived by McGovern *et al.* (2002) based on gravity-topography relationships. Cryosphere thickness is thus greater than in model 1 (Figure 4.2). Annual average surface temperatures are assumed to be the mean of values at  $25^\circ$  and  $60^\circ$  obliquity and are thus somewhat lower at the equator and higher at the pole than at present, leading to smaller latitudinal variations in cryosphere thickness. We also include an adiabatic lapse rate of  $2.5 \text{ K.km}^{-1}$  (Zurek *et al.*, 1992) making higher elevations

slightly cooler. Porosity varies with depth according to Equation 4.5. Recharge is applied to Tharsis elevations above 6000 m (Figure 4.1), since the areal coverage of the topography above this elevation is approximately the same as the South Pole recharge area (about  $1.5 \times 10^6 \text{ km}^2$ ), allowing a more balanced comparison of model results.

In our alternative South Pole model (model 3), we test South Pole recharge given the surface temperatures and geothermal heat flux of the Tharsis Recharge model.

### 4.3. Results

#### *4.3.1 Nominal South Pole Recharge Model*

Instantaneous outflow channel discharges from model 1 (Figure 4.3) show that all outflow sources are able to expel the required volume of water by about 403 Myr, the lower bound on the duration of outflow activity (Figure 4.4a). Fulfillment of discharge requirements appears to support south pole recharge, but comparison with an identical model in which no recharge occurs shows almost the same results (gray curves in Figure 4.3). In fact, South Pole recharge contributes negligibly to outflow discharge: it is principally the high-lying Tharsis province that empties its initial groundwater inventory into the outflow channels, and the relatively thin cryosphere allows it to do so in the short time observed. Only the high assumed sediment-water ratio makes this possible: smaller values would increase the discharge requirement, whereupon contributions from South Pole recharge would be essential. However, the result that South Pole recharge contributes negligibly to outflow discharge over 400 Myr at the modeled permeability, holds regardless of sediment-water ratio.

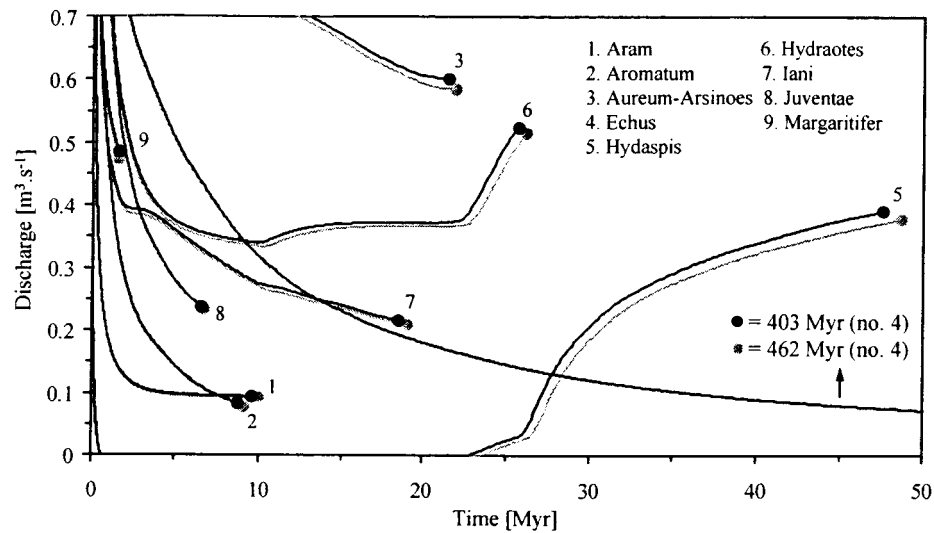


**Figure 4.6** Instantaneous discharges from the nine outflow channel sources of model 1. Source numbering corresponds to Table 4.1. The results of an identical model in which no recharge is applied, are shown by the gray curves.

We note that the individual outflows sources interact strongly: when one source completes its required flow and is shut off, its groundwater supply is diverted to the remaining active outflows, which experience surges in discharge. Only the Echus Chasma source remains active after 50 Myr, and the hydraulic head at 400 Myr (Figure 4.4a) reflects the dominance of this source on the flow pattern.

It is useful to consider the results of this model scaled to different values of some key parameters. First, there is great uncertainty in the sediment-water ratio estimates that are so fundamental to water-volume calculations. We suggest that this ratio is bounded from below by crustal permeability and outflow discharge duration.

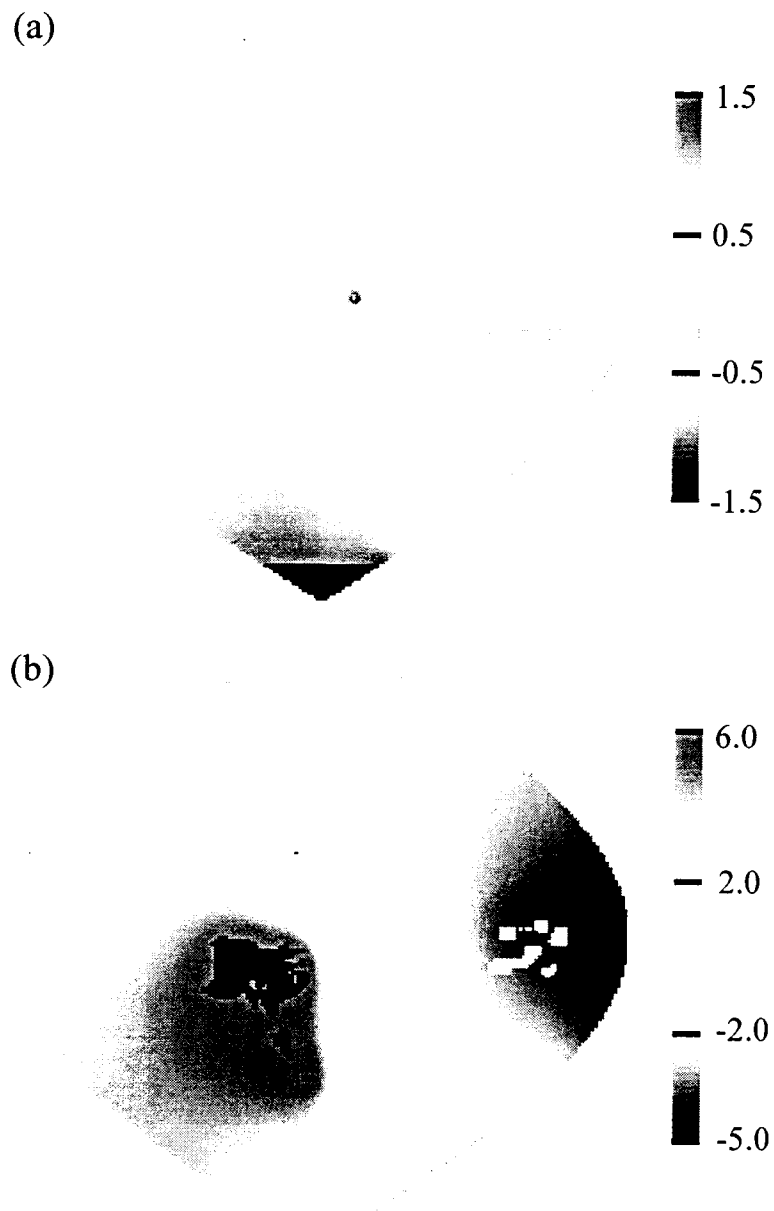


**Figure 4.4** Hydraulic head distribution at 400 Myr in (a) model 1 and (b) model 2. Outflow activity ceases at approximately this time in both models. Recharge zone and outflow sources are shown in black and white, respectively. Scale bars are in km.

Specifically, we know that the circum-Chryse outflows occurred from the late Noachian to the late Hesperian, with an upper bound of about 900 Myr. A preliminary

estimate of the lower bound on sediment-water ratio is therefore that value which allows the outflows to fulfill their discharge requirements in exactly 900 Myr. The analysis can be broadened by repeating the process for a range of viable permeabilities. Manning and Ingebritsen (1999) suggest limits of  $10^{-17}$  and  $10^{-14} \text{ m}^2$  for the mean continental permeability between 1 and 10 km depth, and we scale these to the Martian environment ( $2 \times 10^{-16}$  and  $2 \times 10^{-13} \text{ m}^2$ ). By comparison, Harrison and Grimm (2002) derived a minimum permeability for the Martian crust of  $10^{-17}$ - $10^{-16} \text{ m}^2$  by comparing the requirements for hydrothermal alteration to numerical models of hydrothermal circulation. Rate of discharge can be scaled with complete accuracy only by the time-intensive process of rerunning the model for each permeability value. We assume instead that model 1 instantaneous discharge rates summed over all nine outflows and averaged over the duration of outflow activity (400 Myr in the model) apply to every model of the same permeability, regardless of its duration. (This approach can be interpreted as an assumption of steady state conditions under which instantaneous discharge rates are constant with time and therefore the same regardless of model duration.) We assume further that this time-averaged discharge rate then scales linearly with permeability in the same way as instantaneous rates, as required by Darcy's Law.

In Figure 4.5a, the results are shown in a plot of permeability vs. sediment-water ratio. The dot represents model 1 - its permeability value ( $1.0 \times 10^{-14} \text{ m}^2$ ) as calculated by averaging over all aquifer cells in the model corresponds to an outflow activity duration of 400 Myr. Only those points within the shaded region are physically permissible since they fall below the upper bound on sediment-water ratio (0.67), between the bounds on permeability, and they correspond to total discharge that is complete within 900 Myr. The minimum sediment-water ratio, corresponding to a permeability of  $2 \times 10^{-13} \text{ m}^2$  and a time of 900 Myr, is 0.015, is about two orders

of magnitude higher than ratios inferred for the relatively small outflow channels Maumee and Vedra Valles (de Hon *et al.*, 2003).

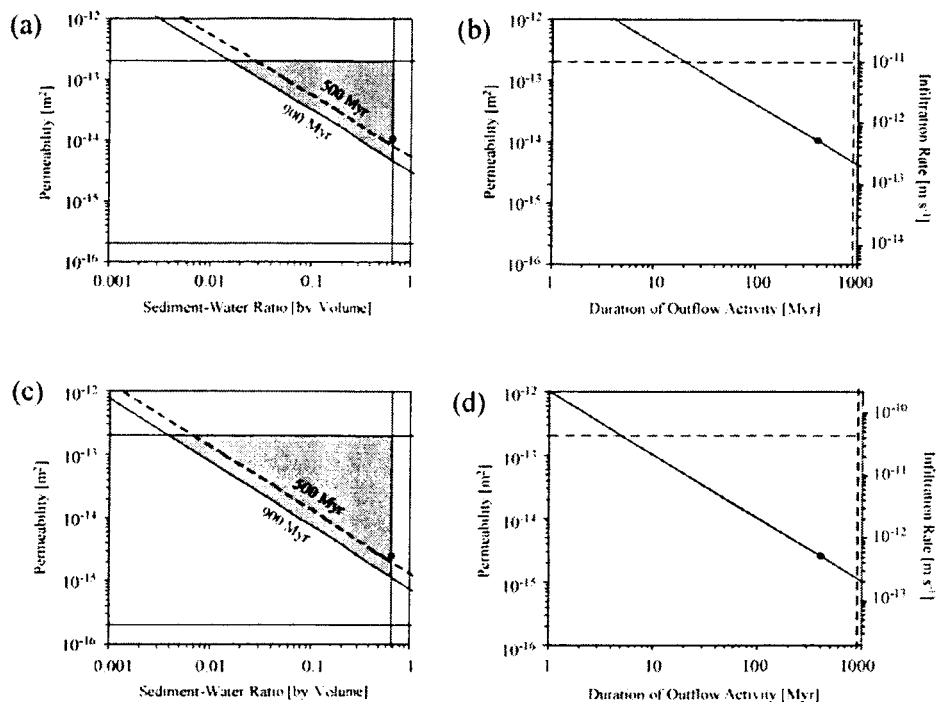
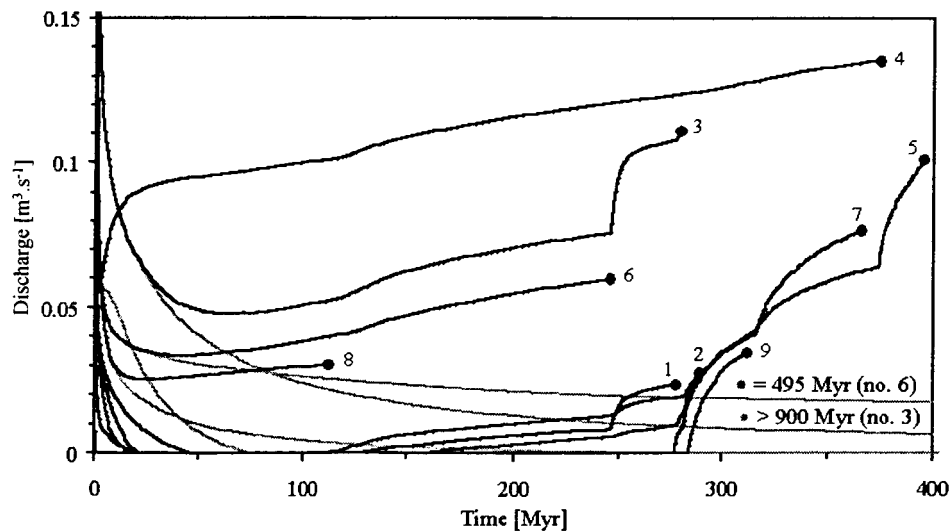


Figure 4.5 (a) Scaling of model 1 average permeability and sediment-water ratio. Bounds discussed in the text limit points to the gray region. (b) Scaling of model 1 average permeability and outflow activity duration. (c) Same as (a) but for model 2. (d) Same as (b) but for model 2.

Next, we consider the influence of recharge rate. When model 1 is rerun with applied recharge rates as low as  $10^{-12}$   $\text{m.s}^{-1}$ , the outflow discharge is the same as that of the nominal model with its applied value of  $2 \times 10^{-10}$   $\text{m.s}^{-1}$ . Clearly only a small fraction of the applied recharge is infiltrating into the aquifer. Although C&P use  $2 \times 10^{-10}$   $\text{m.s}^{-1}$  as a suggested infiltration rate, we see that the aquifer is not capable of conducting this much water. The actual infiltration rate will be similar in magnitude to the average discharge rate, which in model 1 is about  $5 \times 10^{-13}$   $\text{m.s}^{-1}$  (calculated

from the average flux of  $0.23 \text{ m}^3 \cdot \text{s}^{-1}$ , assuming all outflow drains are active). Model 1 is thus operating in a regime in which large perturbations in the recharge rate have no effect on infiltration - only changes in permeability will change the infiltration rate. We thus look at a range of average permeabilities, estimating the duration of outflow activity using the same assumption concerning time-averaged discharge rate (and therefore infiltration rate) made with our sediment-water ratio calculations. The result (Figure 4.6b) is a linear decrease in outflow duration with infiltration rate and permeability (the dot again represents model 1). Outflow activity with a duration of exactly 900 Myr is achieved with an average permeability of  $5 \times 10^{-15} \text{ m}^2$  (compare with the model 1 average value of  $1.0 \times 10^{-14} \text{ m}^2$ ) and an infiltration rate of  $2 \times 10^{-13} \text{ m} \cdot \text{s}^{-1}$ . A minimum outflow activity duration, 13 Myr, is imposed by the upper bound on permeability ( $2 \times 10^{-13} \text{ m}^2$ ), and corresponds to a recharge rate of  $1 \times 10^{-11} \text{ m} \cdot \text{s}^{-1}$ , still less than the applied recharge rate.



**Figure 7.6** Instantaneous discharges from the nine outflow channel sources of model 2. Source numbering corresponds to Table 4.1. The results of an identical model in which no recharge is applied, are shown by the gray curves.

#### 4.3.2 Tharsis Recharge Model

Instantaneous outflow channel discharges from model 2 (Figure 4.6) show that Tharsis recharge is capable of producing the required output within 396 Myr. This is remarkable given that the average aquifer permeability is about 4 times smaller than that of model 1, principally because of the greater model 1 cryosphere thickness. This disadvantage is overcome by the proximity and elevation of Tharsis recharge which produces high hydraulic head gradients that start early and are sustained indefinitely. Nonetheless, some outflows finish later than in the nominal model. Comparison with a model in which no recharge is applied (gray curves in Figure 4.6) reveals substantially smaller discharges, with one outflow source (Aureum-Arsinoes, Table 4.1) still active after 900 Myr. The need for recharge is also observed in the total amount of water initially available in the aquifer, namely  $5.4 \times 10^5 \text{ km}^3$ , less than the total required outflow channel discharge (Table 4.1).

The interaction between sources is similar to that observed in model 1, with the addition of a gradual increase in all discharges. This occurs as recharge slowly raises the hydraulic head of the region (as predicted by C&P for South Pole recharge; compare with gray curves, Figure 4.6), increasing the relative drawdown of the outflow channels. For model 1 South Pole recharge, this effect is not noticeable during the 400 Myr of outflow activity.

We look again at the lower bound on sediment-water ratio. The minimum permissible sediment-water ratio in this model is 0.0038 (Figure 4.5c), corresponding to a permeability of  $2 \times 10^{-13} \text{ m}^2$  and a time of 900 Myr. This is approximately one order of magnitude smaller than the lower bound for model 1 and only one order of magnitude higher than ratios for Maumee and Vedra Valles (de Hon *et al.*, 2003). The results of Figures 5a and 5c encapsulate quantitatively the advantage of Tharsis recharge over South Pole recharge. The former is capable of producing approximately

the same time-averaged outflow discharge rate as the latter, even though average aquifer permeability is about four times smaller (ratio of spatially averaged permeabilities =  $1.0 \times 10^{-14} / 2.6 \times 10^{-15} = 3.8$ ).

Considering a range of infiltration rates (Figure 4.5d, note that the ordinate range is different to Figure 4.3b) reveals that outflow activity lasting exactly 900 Myr is achieved with an average permeability of  $1 \times 10^{-15} \text{ m}^2$  and an infiltration rate of  $2 \times 10^{-13} \text{ m.s}^{-1}$ . The minimum outflow activity duration is 3.2 Myr, corresponding to an infiltration rate of  $4 \times 10^{-11} \text{ m.s}^{-1}$ , still less than the applied recharge rate. The results of Figures 5b and 5d again quantify the advantage of Tharsis recharge, although in slightly different terms. With equal infiltration rates for Tharsis and South Pole recharge, the duration of outflow activity is approximately the same despite the large difference in average permeability.

Finally, we look at our choice of recharge (precipitation) area. For a variety of average infiltration rates and permeabilities, we plot in Figure 4.7a the recharge area required to assure the same flux as model 2 ( $0.24 \text{ m}^3.\text{s}^{-1}$ ). The lower and upper bounds on permeability ( $2 \times 10^{-16} \text{ m}^2$  and  $2 \times 10^{-13} \text{ m}^2$ ) place respective upper and lower bounds on recharge area, namely  $2 \times 10^{13} \text{ m}^2$  and  $2 \times 10^{10} \text{ m}^2$ . The upper bound corresponds to an area almost half that of the tropical band within  $30^\circ$  of the equator (vertical dashed line, Figure 4.7a) and therefore somewhat larger than the Tharsis rise. We discuss below the conditions under which recharge might infiltrate the aquifer only through some fraction of the applied area.

#### *4.3.3 Alternative South Pole Recharge Model*

In the first 500 Myr of model 3, the outflow sources do not (with the exception of the large Aureum-Arsinoes chaos region, Table 4.1) expel much more water than in an identical model with no recharge (Figure 4.8). No source achieves its total required

output before 500 Myr, and only two finish before 900 Myr. Again, it is mainly the drainage of Tharsis that provides water to the outflows, but with model 2 hydrologic and thermal properties this reservoir is not sufficient, as already pointed out in the results for model 2.

For the Aureum-Arsinoes chaos region, the reduced Tharsis inventory means a noticeable relative discharge contribution from South Pole recharge (compare the black and gray curves for outflow source 3 in Figure 4.8). However, absolute discharge is over an order of magnitude less in model 3 than in model 1, and Aureum-Arsinoes reaches its discharge requirements in 800, rather than 22 Myr.

We make some important observations regarding cryosphere thickness. Consider model 1 hydrologic properties with an improved Hesperian heat flux estimate of  $30 \text{ mW.m}^{-2}$  (McGovern *et al.*, 2002). The resulting south pole cryosphere thickness is between 6.5 to 8 km (for melting temperatures ranging from 252 K to 273 K), bringing into question the degree of aquifer connectivity. If porosities are low enough, it is possible for parts of the cryosphere to occupy the entire uncompacted depth of the crust, thereby blocking the lateral flow of groundwater. We calculate latitude-dependent aquifer thickness under this scenario for a range of surface porosities, in order to quantify aquifer connectivity.

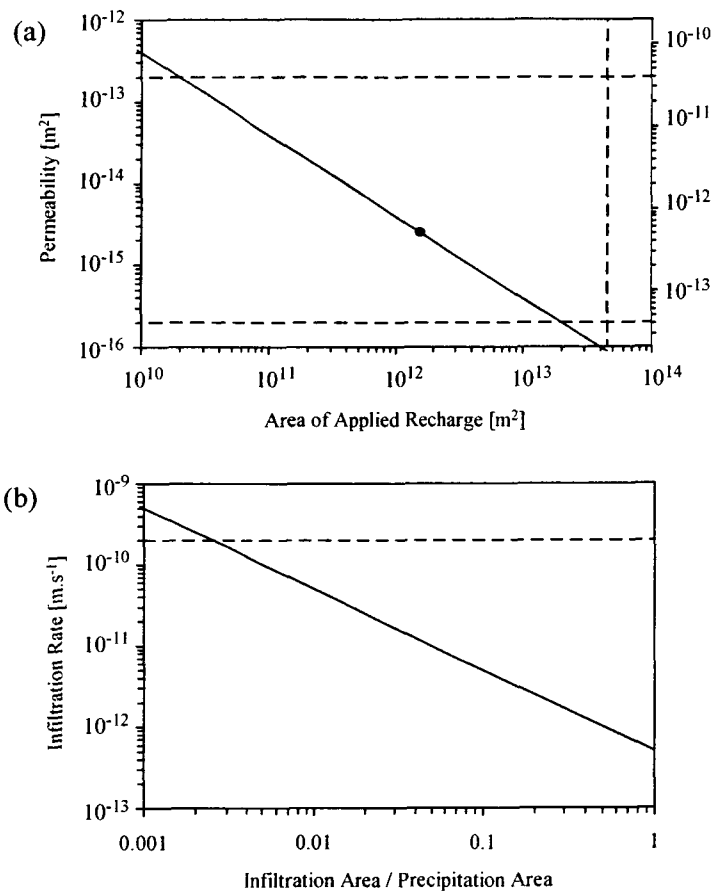


**Figure 4.7** (a) Average permeability and infiltration rates required to maintain the model 2 flux through a range of applied recharge areas. The dot represents model 2. (b) Infiltration rate required to maintain a model 2 outflow activity duration of 396 Myr given a range of reductions in infiltration area with respect to precipitation area. The applied recharge rate of model 2 is indicated by the dotted line. Where the two lines cross, all applied recharge infiltrates the aquifer (i.e. no surface runoff). Infiltration rates above the dotted line are thus impossible to deliver unless the applied recharge is increased.

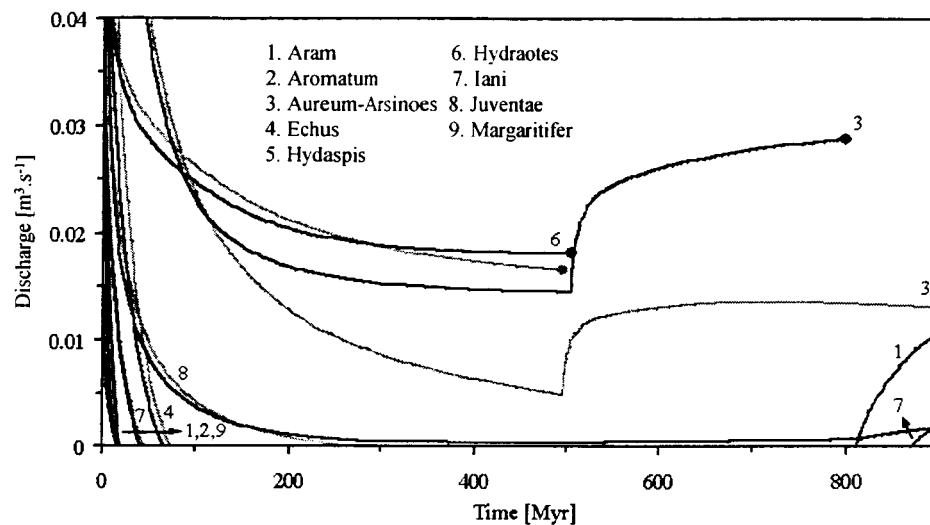


**Figure 4.8** Instantaneous discharges from the nine outflow channel sources of model 3. Source numbering corresponds to Table 4.1. The results of an identical model in which no recharge is applied are shown by the gray curves.

For all surface porosities, the southern hemisphere aquifer is thinnest near the edge of the polar cap at about  $-77^\circ$  latitude (Figure 4.9; note that no cryosphere is present under the south pole ice cap due to basal melting). In the low heat flow model (Figure 4.9b), surface porosities lower than about 10% result in zero aquifer thickness at this latitude, obstructing the northward flow of basal meltwater. This result demonstrates the importance of high surface porosity and geothermal heat flux in model 1 (Figure 4.9a). Hypothetically, if the cryosphere were to grow due to a decrease in surface temperatures, the flow of South Pole recharge would be cut off from the outflow channels while any equatorial recharge would remain connected. As a caveat, we note that the true Martian compaction depth is not known to any great accuracy. If compaction occurs at porosities lower than 1%, then South Pole recharge would be cut off at higher surface porosities.

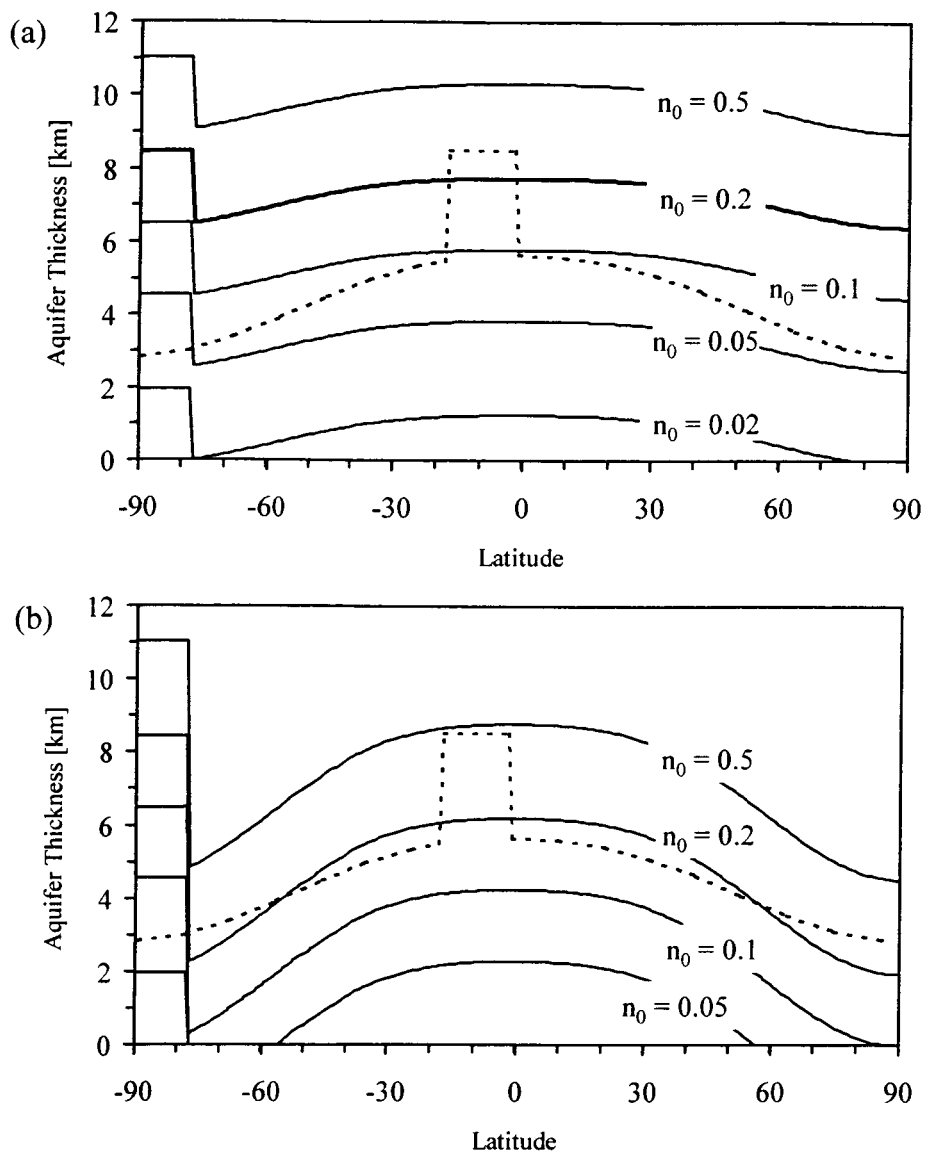


**Figure 4.9** Aquifer thickness as determined by the porosity of Equation 4.4 given a variety of surface values  $n_0$ , and South Pole recharge. In (a) the assumed geothermal heat flux is  $95 \text{ mW.m}^{-2}$  (the bold line corresponds to the  $n_0$  of C&P), in (b) it is  $30 \text{ mW.m}^{-2}$ . In both panels, the aquifer thickness determined by the porosity of Equation 4.5, with Tharsis recharge, is shown (dotted) for comparison. The indicated lateral extent of cryosphere melting for Tharsis recharge corresponds to a longitude of  $245^\circ \text{ E}$ .

#### 4.4 Discussion

We elaborate on some problematic aspects of the C&P South Pole recharge model and then describe the alternative of Tharsis recharge, which may occur through the melting of an ice sheet analogous to South Polar basal melting (C&P), or by direct infiltration of precipitation into parts of the aquifer whose cryosphere has melted due to volcanic heating.

##### *4.4.1 Problematic aspects of the Nominal South Pole Recharge Model*

The C&P South Pole recharge model requires a groundwater aquifer with a high degree of global connectivity, with pressures having to communicate across distances as great as 5000 km from south pole to equator. C&P invoke a decrease in outflow source elevation with time as evidence of a falling global water table. This argument is not supported by the formation process of the Amazonian channels, which may have been different from that of the Noachian and Hesperian channels (Car, 1996), nor is it supported statistically - the Amazonian channels are small in number and are spatially concentrated on the north and northwest flanks of Elysium Mons. With no strong evidence of global connectivity, the possibility of regional heterogeneity in Martian crustal permeability and porosity remains. Such conditions would drastically reduce the already marginal role of South Pole recharge in outflow channel activity (as predicted by model 1).

Second, the C&P model has difficulty explaining the provision of water to the highest outflow channels, which sometimes exceed the elevation of the south pole (Carr, 2002; Coleman *et al.*, 2003). C&P argue that hydraulic head can rise above the level of the south pole topography when the polar cap confines the aquifer, but this is not physically possible, as the head cannot rise above the maximum recharge

elevation. C&P's comparison to a recharge well is inappropriate because the latter provides external mechanical energy to force water into the ground. The Chryse outflows require more water than is initially available in the high elevation Tharsis aquifer (given the improved hydrologic and thermal conditions of model 2) and the South Pole region is too low to recharge these regions.

#### 4.4.2 Tharsis Recharge: Ice Sheet with Basal Melting

As precipitation accumulates to form a growing ice sheet, the melting isotherm that defines the lower boundary of the cryosphere rises, releasing melted ice into the aquifer. Once the ice sheet reaches a thickness comparable to the pre-existing cryosphere, the melting isotherm reaches the ice sheet itself, basal melting begins, and proceeds at a rate approaching the precipitation rate. Our Hesperian model of Tharsis recharge has an equatorial cryosphere thickness, and thus an implied ice sheet thickness, of 2 km. If the precipitation rate is equal to the applied recharge rate of  $2 \times 10^{-10} \text{ m.s}^{-1}$ , such a sheet would accumulate in 0.3 Myr, shorter than an obliquity cycle. The general climate model of Mischna *et al.* (2003), which starts from a steady state solution at the current obliquity, takes 30 yr to accumulate a total mass of  $3 \times 10^{16} \text{ kg}$  within  $30^\circ$  of the equator after obliquity is changed to  $60^\circ$ . This accumulation rate ( $7 \times 10^{-10} \text{ m.s}^{-1}$ ) is linear and, if sufficient water were available (as it would be from cyclical outflow discharges during the Hesperian), would build a 2 km ice sheet in only 0.09 Myr, roughly the duration of an obliquity cycle.

Even if deposition rates are not this high, it is likely that ice could remain at the tropics during short periods of unfavorable obliquity, allowing accumulation to continue during subsequent favorable periods. Mustard *et al.* (2003) describe obliquity cycles with amplitudes as high as  $35^\circ$  that produced a 1.7 Myr ice age that ended only 0.4 Myr ago. They argue that ice would continue to accumulate at mid-

latitudes throughout this ice age, with only small losses during the traverses through low obliquities between cycle maxima.

Additionally, the presence of a thick ( $> 3$  km) polar ice sheet today implies that (non-ice age) sheet growth is not destroyed every 0.1 Myr, so ice has been preserved through unfavorable obliquities by the presence of lag deposits or some other mechanism. Indeed, observations of ice-related processes on the flanks of several of the Tharsis volcanoes (Tanaka, 1985; Head and Marchant, 2003; McGovern *et al.*, 2003) and elsewhere at low latitudes (Boynnton *et al.*, 2002; Mustard *et al.*, 2001 and 2003; Christensen, 2003; Greeley and Fagents, 2001) testify to ice preservation processes at low latitudes also. A comparison of polar and low-latitude atmospheric conditions reveals that tropical summer temperatures at low obliquities would be a few 10's of degrees lower than south polar summer temperatures at high obliquities (Ward, 1992; Mischna *et al.*, 2003; Haberle *et al.*, 2003). Retention of ice at the tropics during high obliquity is thus expected to be more efficient than retention at the poles during low obliquity (Herkenhoff and Murray, 1990; Vasavada *et al.*, 2000).

#### *4.4.3 Tharsis Recharge: Local cryosphere melting*

There exists an alternative recharge pathway at Tharsis, if the ice sheet is not regionally thick enough to induce basal melting. Volcanic activity during the Hesperian may have heated significant fractions of the Tharsis crust, resulting in a thin cryosphere (Tanaka *et al.*, 2002) that at some points may have disappeared altogether (Wilson and Head, 2002). High heat fluxes from local intrusions would thus obviate the need for an ice sheet, allowing precipitation to infiltrate (at least on a local scale) directly into exposed parts of the aquifer. The disadvantage of this form of recharge is that infiltration will not occur at all places experiencing precipitation – only some fraction of the precipitation area will experience recharge. In order to

places bounds on the scale of this reduction, consider a variant of model 2 in which precipitation falls over the same region as before, but infiltrates only through that fraction corresponding to the parts with melted cryosphere. The outflows will have to remain active for a longer period in order to fulfill their discharge requirements. As calculated above, the average infiltration rate that leads to an outflow activity duration of 900 Myr is  $2 \times 10^{-13} \text{ m.s}^{-1}$ . The ratio of this rate and the model 2 rate ( $5 \times 10^{-13} \text{ m.s}^{-1}$ ) thus approximates the lower bound on the ratio of infiltration and precipitation areas, namely 0.4. Put differently, infiltration must occur over at least 40% of the model 2 precipitation area for discharge requirements to be met.

If instead we demand that the total flux of water into the aquifer remains at a constant value of  $0.24 \text{ m}^3.\text{s}^{-1}$  (and therefore that outflow activity duration remains at 396 Myr), we can calculate the precipitation rate required for a given ratio of infiltration-precipitation area (Figure 4.7b). The dotted line represents the applied recharge of  $2 \times 10^{-10} \text{ m.s}^{-1}$ , and for points on the solid line above this threshold, infiltration cannot be delivered at the indicated rate unless the applied recharge is increased. However, by assuming that permeability scales with infiltration as before, its upper bound ( $2 \times 10^{-13} \text{ m}^2$ ) limits the infiltration rate to  $4 \times 10^{-11} \text{ m.s}^{-1}$  (Figure 4.5d), which does not exceed the applied recharge of model 2. This maximum infiltration rate corresponds to an infiltration-precipitation area ratio of 1.3%, or a total area of melted cryosphere only  $19600 \text{ km}^2$ .

#### 4.4.4 Other Outflow Channels

Finally, we make some remarks concerning outflow channels not belonging to the circum-Chryse group. These include Dao, Reull, and Harmakhis Valles on the northeast rim of Hellas Planitia; Ma'adim and Mangala Valles in the Amazonis Planitia; and the Amazonian channels on the northern and northwestern flanks of

Elysium Mons. Only Ma'adim and Mangala Valles do not lie close to volcanic centers. Mangala Valles issues from a graben that likely disrupted the local cryosphere. Recent work suggests that Ma'adim Vallis formed due to catastrophic overflow of a paleo-lake (Irwin *et al.*, 2002) and therefore might not conform to the model of groundwater discharge from the cryosphere.

#### 4.5 Conclusions

C&P explain the delivery of water to the outflow channels by the communication of confined pore fluid pressures across a globally connected aquifer from a South Polar recharge zone northwards to the tropics, where water discharges through a disruption in the cryosphere and erodes the circum-Chryse outflows. We performed numerical simulations to test both this hypothesis and an alternative in which the aquifer is recharged over the Tharsis rise, and therefore is not required to be globally connected. Our conclusions follow.

1. In a nominal model with hydrologic and thermal properties assumed by C&P, South Pole recharge contributes little to outflow discharge. The assumed permeability results in fulfillment of discharge requirements only because the high sediment-water ratio allows the entire discharge volume to be supplied by water drained from the Tharsis aquifer. At lower sediment-water ratios, the weak contribution of South Pole recharge will not be able to produce required discharges in the allotted time unless permeabilities are increased.

2. In a model with improved, yet more conservative properties, Tharsis recharge is able to meet discharge requirements in approximately the same time as the nominal South Pole model. In this case, recharge is an essential contributor to outflow discharge, asserting a strong, sustained influence.

3. South Pole recharge with the improved properties of the Tharsis recharge model performs worse than the nominal model, with only 2 of the 9 modeled outflows completing their discharge requirements in 900 Myr.

Simple linear scaling of our Tharsis recharge model results indicates that for average permeabilities as high as  $2 \times 10^{-13} \text{ m}^2$ , the minimum sediment-water ratio that allows discharge requirements to be met in the maximum allowed time of 900 Myr, is 0.0038. Alternatively, with a high sediment-water ratio (0.67) and high permeability, the region over which recharge occurs could be as small as  $2 \times 10^4 \text{ km}^2$ . If the recharge region remains at the assumed value of  $1.5 \times 10^6 \text{ km}^2$ , high permeabilities might allow discharge requirements to be met in only 3.2 Myr.

We argue that recharge through Tharsis occurs at high obliquity when ice is perennially stable in the tropics. Infiltration of water into the aquifer may take place in at least two ways:

1. Basal melting of an ice sheet. In analogy to the melting of a South Polar ice cap (C&P), we suggest that the insulating effects of an accumulating ice sheet might raise the melting isotherm to intersect with the base of the sheet, resulting in the steady infiltration of meltwater into the Tharsis aquifer, from whence it flows down a steep hydraulic head gradient to the outflow channels.

2. Local cryosphere melting. The presence of volcanic activity in Tharsis throughout the Hesperian suggests that the melting isotherm may have locally and temporarily risen to the surface, allowing the direct infiltration of precipitation.

## CHAPTER 5

### CONCLUSIONS

we conclude this work with a summary of essential results, a brief analysis of key unsolved issues influencing my conclusions, and a description of factors necessary to improve the accuracy of my calculations.

#### 5.1 Valley Networks

Hydrotherm discharge attending crustal formation processes may have been sufficient to supply the erosional requirements of the ancient Southern Highlands valley networks that correlate spatially with crustal magnetic anomalies. This result is supported by numerical calculations of groundwater convection due to the intrusion of a magma chamber. The nominal model of a  $50 \text{ km}^3$  chamber in host rock of permeability  $10^{-16} \text{ m}^2$  provides enough discharge, when building that part of the crust covered by the valley networks, to fall within the bounds of the water volume required for valley erosion. Larger chambers, possibly more appropriate to the martian environment, produce even more discharge than the nominal model. Factors producing a reduction in discharge include evaporation and, more importantly, water table elevation.

Discharge requirements place a lower bound on host rock permeability of  $10^{-17} \text{ m}^2$ , while alteration requirements suggest a minimum of  $10^{-16} \text{ m}^2$ . We note that discharge requirements depend on the sediment-water ratio, which for the valley networks might range from  $10^{-3}$  to 0.25.

## **5.2 Long Runout Landslides**

Numerical simulations of martian landslides with a variety of material rheologies suggest that long runout landslides in the Valles Marineris may have resulted from the fluidization of the falling debris due to pore fluid pressure. A fluidization rheology which partitions failure into an initial frictional stage and a final power law stage, produces landslide runouts that match observed profiles in five of seven martian landslides modeled. Frictional sliding applied to the entire duration of failure only reproduces long runouts with unrealistically high pore pressures and, along with other rheologies such as Bingham flow, cannot reproduce certain aspects of the final profile, such as the toe height and rear displacement.

Pore pressures required by our fluidization rheology are high, but physically tenable. The equatorial location of the landslides implies that cryosphere thickness may have been low enough to allow the stable presence of pore water in the failure zone, which in the largest landslides is a few kilometres below the surface.

Simulations of an Olympus Mons aureole indicate that it is unlikely to be the product of catastrophic landsliding since unrealistically high pore pressures are required for all rheologies. Formation processes suggested by other workers do, however, require the action of water or ice.

## **5.3 Outflow Channels**

Clifford and Parker (2001) suggest that the confined Hesperian aquifer was recharged at the South Pole in order to stimulate global groundwater leading to outflow channel formation. My suggestion that recharge over Tharsis at high obliquity is a more efficient means of driving outflow discharge is strongly supported by numerical simulations that compare the two recharge scenarios. For the chosen

crustal permeability, South Pole recharge has a weak effect on outflow discharge during the supposed period of formation (at most 900 Myr), whereas Tharsis recharge dominates discharge production throughout the duration of outflow activity.

As with valley networks, the discharge requirements depend on sediment-water ratio, which for our models is assumed to be at a maximum value of 0.67. Smaller sediment-water ratios require a greater volume of discharge through the outflow channels, which can be accommodated in the allowed time if permeability is increased. Simple scaling relations show that a reasonable maximum (average) permeability of  $2 \times 10^{-13} \text{ m}^2$  allows a sediment-water ratio as low as 0.4% for outflow discharge fed by Tharsis recharge.

#### **5.4 Historical Relationship Between Landforms and Environment**

The relative timing of valley networks, long runout landslides, and outflow channels is shown in Figure 5.1, along with crustal heat fluxes and cryosphere thicknesses assumed by C&P and myself (Chapter 4).

There is still some debate regarding Noachian atmospheric conditions. Surface runoff implied by valley network formation seems to suggest temperatures above freezing, but younger Amazonian valleys, such as those on Alba Patera, probably formed under cold atmospheric conditions similar to those of the present. If the Noachian atmosphere was indeed cold, an explanation of the sapping morphology of the valley networks must incorporate the effects of a cryosphere on the order of 1 km thick (Figure 5.1). As shown in Chapter 2, hydrothermal discharge is capable of melting through such a cryosphere with a significant, but not crippling reduction in surface discharge. Warm hydrothermal discharge might remain in the liquid phase long enough to cause significant erosion, as suggested by the Alba Patera valleys. The

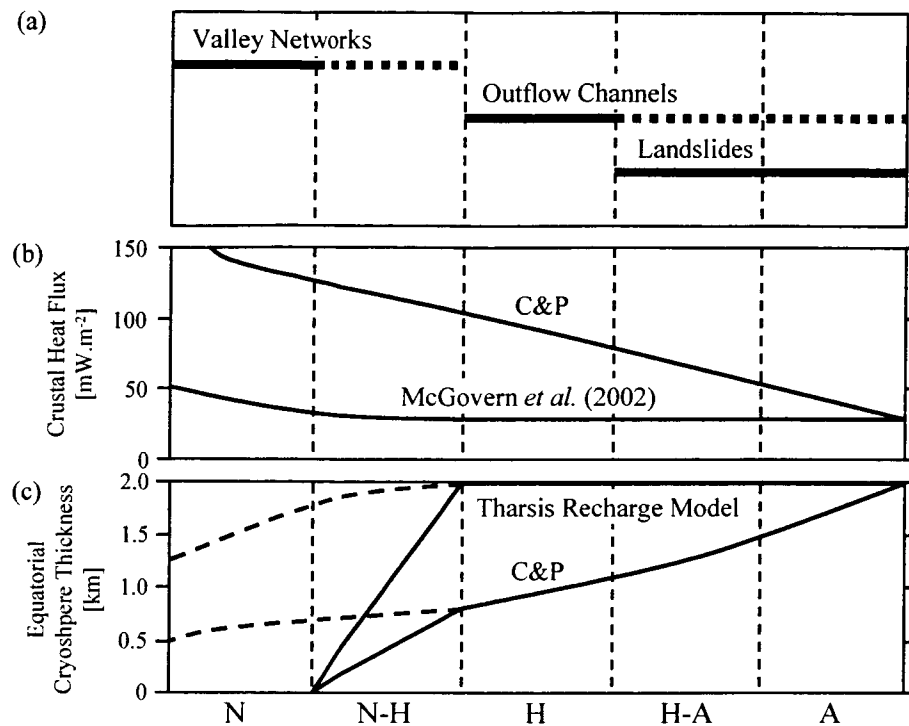


**Figure 5.1** (a) Relative timing of valley networks, outflow channels, and long runout landslides. Dashed lines indicate decreased production of the indicated landform. (b) Crustal heat fluxes assumed by C&P, and calculated by McGovern *et al.* (2002). The latter curve represents approximately the lowest values calculated by McGovern *et al.* (2002). Hesperian values correspond to those used in models 1 and 2 of chapter 4. (c) Equatorial cryosphere thicknesses result from the crustal heat fluxes of (b), and from surface temperatures corresponding to an obliquity of 25° (“C&P”), and to an average of obliquities between 25° and 60° (“Tharsis Recharge Model”). The linear increase over the N-H epoch is a response to the depletion of an assumed thick, warm Noachian atmosphere. A thin, cold Noachian atmosphere gives rise to the dashed curves.

argument for hydrothermally driven discharge is in fact stronger under cold atmospheric conditions, since alternatives involving precipitation, which would be in solid form, are unlikely to produce runoff. At best, precipitation would contribute to valley network formation by infiltrating into locally melted parts of the cryosphere (in

analogy to Tharsis recharge during the Hesperian) and mixing with hydrothermally circulating groundwater.

Figure 5.1 shows a decline in valley network production during the late Noachian and early Hesperian. Ostensibly this decline is due to the development of a cryosphere following the depletion of a warm Noachian atmosphere (Carr, 1996). If the Noachian atmosphere was cold and dry, a decline in valley network formation might still occur in response to waning crustal formation (and therefore hydrothermal activity), although it may not be as rapid.

Uncertainty in the role of groundwater arises from apparently incompatible inferences drawn from mineral assemblages in the Valles Marineris. An analysis of infrared MGS TES data by Staid *et al.* (2001) indicates the presence of unaltered olivine, implying persistently dry conditions. The deposit is not mentioned explicitly by other workers (e.g. Hoefen and Clark, 2001; Clark *et al.*, 2002) but other deposits, mostly in ancient terrain (e.g. Terra Meridiani, Syrtis Major, southern Acidalia Planitia, and Terra Tyrrhena; Hoefen and Clark, 2001) give rise to the same conclusion: a dry early Mars (Christensen *et al.*, 2001a). Also detected in the Valles Marineris are deposits of crystalline gray hematite, a product of aqueous alteration. The hematite is closely associated with the interior layered deposits (Christensen *et al.*, 2001b) and implies the long-term presence of liquid water on a local scale. Groundwater flow in the Valles Marineris is also indicated by morphological aspects of the interior deposits, and by long runout landslides, and its influence is suggested indirectly by inter-chorasma groundwater features (Carr, 1996) and the proximity of the outflow channels.

An apparently paradoxical picture thus emerges of continuously dry conditions coexisting with regions of local water stability. Further analysis of the olivine deposits, especially in the Valles Marineris, is required, and must take into account

the degree of alteration, which is difficult to detect with the available infrared data (Kraft *et al.*, 2002).

With regard to long runout landslides, note that the equatorial cryosphere thickness (Figure 5.1) is never greater than 2 km, supporting my suggestion that the failure-zones of Valles Marineris landslides may have been saturated with water.

### 5.5 Future Improvements

The acceleration in our understanding of water on Mars, as alluded to in the Introduction, is a continually developing process. There are still several gaps in our knowledge of Martian aquifer conditions that in this work occasionally translate into uncertainties in quantitative results. Groundwater simulations cannot accurately model a real physical environment if little is known about the nature of its permeability and porosity. To date, hydrologic properties of the Martian aquifer have been based on extrapolations from terrestrial data, which are themselves incomplete and difficult to interpret. Further measurements of the Martian environment would increase our understanding of both the porosity structure (e.g. seismic data) and the present location of ice and groundwater (e.g. radar).

The weak constraints on sediment-water ratio in valley network and outflow channel formation also need to be addressed. Detailed analysis of channel and bedform morphologies, coupled with improved knowledge of the size, distribution, and history of the water inventory of Mars, would tighten these constraints.

## BIBLIOGRAPHY

- Acuña, M. H., J. E. P. Connerney, N. F. Ness, R. P. Lin, D. L. Mitchell, C. W. Carlson, J. McFadden, K. A. Anderson, H. Reme, C. Mazelle, D. Vignes, P. Wasilewski, and P. A. Cloutier, Global distribution of crustal magnetization discovered by the Mars Global Surveyor MAG/ER experiment, *Science*, 284, 790-793, 1999.
- Allen, C. C., Areal distribution of Martian rampart craters, *Icarus*, 39, 111-123, 1979.
- Anderson, R. C., J. M. Dohm, M. P. Golombek, A. F. C. Haldemann, B. J. Franklin, K. L. Tanaka, J. Lias, B. Peer, Primary centers and secondary concentrations of tectonic activity through time in the western hemisphere of Mars, *J. Geophys. Res.*, 106, E9, 20563-20586, 2001.
- Athy, L. F., Density, porosity, and compaction of sedimentary rocks, *American Association of Petroleum Geologists' Bulletin*, 14, 1-24, 1930.
- Bagnold, R. A., Experiments on a gravity-free dispersion of large solid spheres in a Newtonian fluid under shear, *Proc. Royal Soc. Lon. A*, 225, 49-63, 1954.
- Baker, V. R., *The channels of Mars*, University of Texas Press, Austin, Texas, 1982.
- Baker, V. R., Water and the martian landscape, *Nature*, 412, 228-236, 2001.
- Baker, V. R. and D. J. Milton, Erosion by catastrophic floods on Mars and Earth, *Icarus*, 23, 27-41, 1974.
- Baker, V. R., M. H. Carr, V. C. Gulick, C. R. Williams, and M. S. Marley, Channels and valley networks, in *Mars*, 493-522, Univ. of Ariz. Press, Tucson, 1992.
- Banderdt, W. B. and A. Vidal, Surface drainage on Mars, 32<sup>nd</sup> LPSC, #1488, 2001.
- Besq, A., P. Monnet, and A. Pantet, Flow situations of drilling muds: effects of thixotropic property, *Proc. 6th Triennial Int. Sym. on Fluid Cont. Meas. and Vis.*, #063, 2000.

- Beverage, J. P., and J. K. Culbertson, Hyperconcentrations of suspended sediment, *J. Hydraul. Div., Proc. Amer. Soc. Civil Eng.*, HY6, 117-128, 1964.
- Binder, A. B. and M. A. Lange, On the thermal history, thermal state, and related tectonism of a moon of fission origin, *J. Geophys. Res.*, 85, 3194-3208, 1980.
- Blasius, K. R., J. A. Cuts, J. E. Guest, H. Masursky, Geology of the Valles Marineris: First analysis of imaging from the Viking Orbiter 1 primary mission, *J. Geophys. Res.*, 82, 4067-4091, 1977.
- Bonacina, C., Comini, G., Fasano, A., and Primicero, M., Numerical solution of phase-change problems, *Int. J. Heat Mass Transfer*, 16, 1825-1832, 1973.
- Boynton, W. V., W. C. Feldman, S. W. Squyres, T. H. Prettyman, J. Brückner, L. G. Evans, R. C. Reedy, R. Starr, J. R. Arnold, D. M. Drake, P. A. J. Englert, A. E. Metzger, we. Mitrofanov, J. we. Trombka, C. d'Uston, H. Wänke, O. Gasnault, D. K. Hamara, D. M. Janes, R. L. Marcialis, S. Maurice, we. Mikheeva, G. J. Taylor, R. Tokar, C. Shinohara, Distribution of hydrogen in the near surface of Mars: Evidence for subsurface ice deposits, 297, 5578, 81-85, 2002.
- Brace, W. F. and D. L. Kohlstedt, Limits on lithospheric stress imposed by laboratory experiments. *J. Geophys. Res.*, 85, 6248-6252, 1980.
- Brakenridge, G. R., The origin of fluvial valleys and early geologic history, Aeolis Quadrangle, Mars, *J. Geophys. Res.*, 95, 17289-17308, 1990.
- Burnett, M.S., D. W. Caress, and J. A. Orcutt, Tomographic imaging of the magma chamber at 12 ° 50 'N on the East Pacific Rise, *Nature*, 339, 206-208, 1989.
- Carr, M. H., Formation of Martian flood features by release of water from confined aquifers, *J. Geophys. Res.*, 84, 2995-3007, 1979.
- Carr, M. H., *Water on Mars*, Oxford University Press, New York, 1996.
- Carr, M. H., Elevations of water-worn features on Mars: Implications for circulation of groundwater, *J. Geophys. Res.*, 107, E12, DOI 10.1029/2002JE001845, 2002.

- Carr, M. H. and J. W. Head, Oceans on Mars: An assessment of the observational evidence and possible fate, *J. Geophys. Res.*, 108, E5, DOI 10.1029/2002JE001963, 2003.
- Carr, M. H., and F. C. Chuang, martian drainage densities, *J. Geophys. Res.*, 102, 9145-9152, 1997.
- Caruso, P. A., Seismic triggering mechanisms of large-scale landslides, Valles Marineris, 34<sup>th</sup> LPSC, #1525, 2003.
- Cathles, L. M., A. H. J. Erendi, and T. Barrie, How long can a hydrothermal system be sustained by a single intrusive event?, *Econ. Geol.*, 92, 766-771, 1997.
- Chapman, M. G. and K. L. Tanaka, Related magma-ice interactions: Possible origins of chasmata, chaos, and surface materials in Xanthe, Margaritifer, and Meridiani Terrae, Mars, *Icarus*, 155, 324-339, 2002.
- Christensen, P. R., Formation of recent Martian gullies through melting of extensive water-rich snow deposits, *Nature*, 422, 6927, 45-48, 2003.
- Christensen, P. R., V. E. Hamilton, S. W. Ruff, J. L. Bandfield, R. V. Morris, R. N. Clark, The mineralogy of the Martian surface: Results from the MGS Thermal Emission Spectrometer, *AGU Fall Meeting*, #P41A-05, 2001a.
- Christensen, P. R., R. V. Morris, M. D. Lane, J. L. Bandfield and M. C. Malin, Global mapping of Martian hematite mineral deposits: Remnants of water-driven processes on early Mars, *J. Geophys. Res.*, 106, E10, 23873-23885, 2001b.
- Clark, R. N., T. Hoefen, J. Moore, Martian olivine global distribution and stratification using spectral feature mapping of Mars Global Surveyor Thermal Emission Spectrometer data, 34<sup>th</sup> DPS Meeting, 34, p. 838, 2002.
- Cleary, P. W. and C. S. Campbell, Self-lubrication for long-runout landslides: examination by computer simulation, *J. Geophys. Res.* 98, 21911-21924, 1993.

- Clifford, S. M., A model for the hydrologic and climatic behaviour of water on Mars, *J. Geophys. Res.* 98, 10973-11016, 1993.
- Clifford, S. M. and T. J. Parker, Hydraulic and thermal arguments regarding the existence and fate of a primordial Martian ocean, 30<sup>th</sup> LPSC, #1619, 1999.
- Clifford, S. M. and T. J. Parker, The evolution of the Martian hydrosphere: Implications for the fate of a primordial ocean and the current state of the northern plains, *Icarus*, 154, 40-79, 2001.
- Coleman, N. M. and C. L. Dinwiddie, Groundwater recharge in an epoch of climax lakes in the Valles Marineris, Mars, 34<sup>th</sup> LPSC, #1399, 2003.
- Coleman, N. M., C. L. Dinwiddie, and K. Casteel, High channels on Mars indicate Hesperian recharge at low latitudes, 6<sup>th</sup> Int. Conf. Mars, #3071, 2003.
- Collins, S. A., The Mariner 6 and 7 pictures of Mars, NASA SP-263, 1971.
- Connerney, J. E. P., M. H. Acuña, P. J. Wasilewski, N. F. Ness, H. Rème, C. Mazelle, D. Vignes, R. P. Lin, D. L. Mitchell, and P. A. Cloutier, Magnetic lineations in the ancient crust of Mars, *Science*, 284, 794-797, 1999.
- Dade, W. B. and H. E. Huppert 1998. Long-runout rockfalls, *Geology*, 26, 9, 803-805.
- Davis, S. N., Porosity and permeability of natural minerals, in *FlowThrough Porous Media* (ed. R. J. M. de Wiest), 53-89, Academic Press, New York, 1969.
- de Hon, R. A., P. A. Washington, and C. J. Thibodeaux, Excavation time for the Vedra and Maumee Channels (Mars) by application of equilibrium sediment transport theory, 34<sup>th</sup> LPSC, #1178, 2003.
- Delaney, P. T., Rapid intrusion of magma into wet rock: groundwater flow due to pore pressure increases, *J. Geophys. Res.*, 87, 7739-7756, 1982.
- Dunne, T., Formation and controls of channel networks, *Prog. Phys. Geography*, 4, 211-239, 1980.

- Fanale, F. P., J. R. Salvail, A. P. Zent, S. E. Postawko, Global distribution and migration of sub-surface ice on Mars, *Icarus*, 67, 1-18, 1986.
- Farmer, J., Hydrothermal systems on Mars: an assessment of present evidence, in *Evolution of hydrothermal ecosystems on Earth (and Mars?)*, Wiley, Chichester (Ciba Found. Symp. 202), 273-299, 1996.
- Fetter, C. W., *Applied hydrogeology*, Macmillan College Publishing Company, New York, 1994.
- Francis, P. W. and G. Wadge, The Olympus Mons aureole: formation by gravitational spreading. *J. Geophys. Res.* 88, 8333-8344, 1983.
- Goetz, P. and H. J. Melosh, Experimental observation of acoustic fluidization in sand, *Eos Trans. AGU*, 61, 373, 1980.
- Goguel, J., Scale-dependent rockslide mechanisms, with emphasis on the role of pore fluid vaporization, *Rockslides and Avalanches*, 1, 693-705, 1978.
- Gooding, J. L., S. J. Wentworth, and M. E. Zolensky, Aqueous alteration of the Nakhla meteorite, *Meteoritics*, 26, 135-143, 1991.
- Greeley, R. and S. A. Fagents, Icelandic pseudocraters as analogs to some volcanic cones on Mars, *J. Geophys. Res.*, 106, E9, 20527-20546, 2001.
- Griffith, L. L., and E. L. Shock, Hydrothermal hydration of martian crust: illustration via geochemical model calculations, *J. Geophys. Res.*, 102, 9135-9143, 1997.
- Grimm, R. E., Magnetic lineations on Mars: formation by Noachian crustal accretion or depletion?, Lunar And Planetary Science Conference XXXI Abstract, #2056, 2000.
- Grimm, R. E. and K. P. Harrison, A parochial view of groundwater flow on Mars, 34<sup>th</sup> LPSC, #2053, 2003.
- Guest, J. E., Geology of the farside crater Tsiolkovsky, in *Geology and physics of the moon* (Fielder G., Ed), Elsevier, Amsterdam, 93-103, 1971.

- Gulick, V. C., Magmatic intrusions and a hydrothermal origin for fluvial valleys on Mars, *J. Geophys. Res.*, 103, 19,365-19,387, 1998.
- Gulick, V. C., Origin of the valley networks on Mars: a hydrological perspective. *Geomorphology*, 37, 241-268, 2001.
- Haberle, R. M., C. P. McKay, J. Schaeffer, M. Joshi, N. A. Cabrol, E. A. Grin, Meteorological control on the formation of Martian paleolakes, 31<sup>st</sup> LPSC, #1509, 2000.
- Haberle, R. M., J. R. Murphy, J. Schaeffer, Orbital change experiments with a Mars general circulation model, *Icarus*, 161, 66-89, 2003.
- Habib, P., Production of gaseous pore pressure during rock slides, *Rock Mech.*, 7, 193-197, 1975.
- Harbaugh, A. W., E. R. Banta, M. C. Hill, and M. G. McDonald, MODFLOW-2000, The U.S. Geological Survey modular ground-water model – user guide to modularization concepts and the ground-water flow process, Open-file Report 00-92, 2000.
- Harrison, K. P. and R. E. Grimm, Controls on Martian hydrothermal systems: Application to valley network and magnetic anomaly formation, *J. Geophys. Res.*, 107, E5, DOI 10.1029/2001JE001616, 2002.
- Harrison, K. P. and R. E. Grimm, Rheological constraints on Martian landslides, *Icarus*, 163, 2, 347-362, 2003.
- Hartmann, W. K., and G. Neukum, Cratering chronology and the evolution of Mars, *Space Sci. Rev.*, 96, 165-194, 2001
- Hauck, S. A. and R. J. Phillips, Thermal and crustal evolution of Mars, *J. Geophys. Res.*, 107, E7, DOI 10.1029/2001JE001801, 2002.
- Hayba, D. O., and S. E. Ingebritsen, The computer model HYDROTHERM, a three-dimensional finite-difference model to simulate groundwater flow and heat

- transport in the temperature range of 0 to 1,200 °C, U.S. Geological Survey, Water-Resources Investigations Report 94-4045, 1994.
- Hayba, D. O., and S. E. Ingebritsen, Multiphase groundwater flow near cooling plutons, *J. Geophys. Res.*, 102, 12,235-12,252, 1997.
- Head, J. W., and L. Wilson, Mars: formation and evolution of magma reservoirs, 25<sup>th</sup> LPSC, 527-528, 1994.
- Head, J. W. and L. Wilson, Mars: geologic setting of magma/H<sub>2</sub>O interactions, 32<sup>nd</sup> LPSC, #1215, 2001.
- Head, J. W. and D. R. Marchant, Cold-based mountain glaciers on Mars: Western Arsia Mons, *Geology*, 31, 7, 641-644, 2003.
- Head, J. W., L. Wilson, and K. L. Mitchell, Generation of recent massive water floods at Cerberus Fossae, Mars by dike emplacement, cryospheric cracking, and confined aquifer groundwater release, *Geophys. Res. Lett.*, 30, 11, DOI 10.1029/2003GL017135, 2003.
- Herkenhoff, K. E. and B. C. Murray, High-resolution topography and albedo of the South Polar layered deposits on Mars, *J. Geophys. Res.*, 95, 14511-14529, 1990.
- Hoefen, T. M., and R. N. Clark, Compositional variability of Martian olivines using Mars Global Surveyor Thermal Emission spectra, 32<sup>nd</sup> LPSC, #2049, 2001.
- Hoffman, N., White Mars: a new model for Mars' surface and atmosphere based on CO<sub>2</sub>, *Icarus*, 326-342, 2000.
- Howard, K. A., Avalanche mode of motion: implications from lunar examples. *Science*, 180, 1052-1055, 1973.
- Hsu, K. J., Catastrophic debris streams (struzstroms) generated by rockfalls, *GSA Bulletin*, 86, 129-140, 1975.
- Hungr, O., A model for the runout analysis of rapid flow slides, debris flows, and avalanches, *Can. Geotech*, 32, 610-623, 1995.

- Hungr, O. and S. G. Evans, A dynamic model for landslides with changing mass. *Eng. Geol. and Env.*, 719-724, 1997.
- Hynek, B. M., and R. J. Phillips, Evidence for extensive denudation of the martian highlands, *Geology* (Boulder), 29, 5, 407-410, 2001.
- Ingebritsen, S. E., and M. L. Sorey, Vapor-dominated zones within hydrothermal systems: evolution and natural State, *J. Geophys. Res.*, 93, 13,635-13,655, 1988.
- Ingebritsen, S. E., and W. E. Sanford, *Groundwater in Geologic Processes*, Cambridge Univ. Press, 1998.
- Ingersoll, A. P., Mars: The case against permanent CO<sub>2</sub> frost caps, *J. Geophys. Res.*, 79, no. 24, 3403-3410, 1974.
- Irwin, R. P., T. A. Maxwell, A. D. Howard, R. A. Craddock, D. W. Leverington, A Large paleolake basin at the head of Ma'adim Vallis, Mars, *Science*, 296, 5576, 2209-2212, 2002.
- Iverson, R. M., M. E. Reid, and R. G. LaHusen, Debris-flow mobilization from landslides, *Annu. Rev. Earth Planet. Sci.* 25, 85-138, 1997.
- Jaeger, J. C. and N. G. W. Cook, *Fundamentals of rock mechanics*, Chapman and Hall, London, 1979.
- Jakosky B. M., and Farmer, C. B., The seasonal and global behavior of water vapor in the Mars atmosphere: Complete global results of the Viking atmospheric water detection experiment, *J. Geophys. Res.*, 87, 2999-3019, 1982.
- Jakosky, B. M. and M. H. Carr, Possible precipitation of ice at low latitudes of Mars during periods of high obliquity, *Nature*, 315, 559-561, 1985.
- Jakosky, B. M. and R. J. Phillips, Mars' volatile and climate history, *Nature*, 412, 237-244, 2001.
- Kent, P. E., The transport mechanism in catastrophic rockfalls, *J. Geol.*, 74, 79-83, 1966.

- Kieffer, H. H., Mars Consortium global maps, LPI contribution 441, 3<sup>rd</sup> International colloquium on Mars, 133-135, 1981.
- Kletetschka, G., P. J. Wasilewski, P. T. Taylor, Hematite vs. magnetite as the signature for planetary magnetic anomalies?, *Phys. Earth Planet. Inter.*, 119, 259-267, 2000.
- Kohlstedt, D. L., B. Evans, and S.J. Mackwell, Strength of the lithosphere: Constraints imposed by laboratory experiments, *J. Geophys. Res.*, 100, 17587-17602, 1995.
- Komar, P. D., Modes of sediment transport in channelized water flows with ramifications to the erosion of the Martian outflow channels, *Icarus*, 42, 317-329, 1980.
- Kraft, M. D, T. G. Sharp, A. Trueba, T. R. Diedrich, Thermal emission spectra of red, oxidized olivine: Implications for olivine on Mars, 33<sup>rd</sup> LPSC, #1964, 2002.
- Laskar, J. and P. Robutel, The chaotic obliquity of the planets, *Nature*, 361, 608-612, 1993.
- Leighton, R. B., B. C. Murray, R. P. Sharp, J. D. Allen, and R. K. Sloan, Mariner IV photography of Mars: Initial results, *Science*, 149, 627-630, 1965.
- Leighton, R. B., N. H. Horowitz, B. C. Murray, R. P. Sharp, A. G. Herriman, A. T. Young, B. A. Smith, M. E. Davies, C. G. Leovy, Mariner 6 and 7 television pictures: Preliminary analysis, *Science*, 166, 49-67, 1969.
- Longhi, J., E. Knittle, J. R. Holloway, and H. Wanke, The bulk composition, mineralogy and internal structure of Mars, in *Mars* (H. H. Keiffer, B. M. Jakosky, C. W. Snyder, and M. S. Matthews, Eds), Univ. Arizona Press, Tuscon, 184-208, 1992.
- Lopes, M. C. L., J. E. Guest, and C. J. Wilson, Origin of the Olympus Mons aureole and perimeter scarp, *Moons Planets* 22, 221-234, 1980.

- Lopes, M. C. L., J. E. Guest, K. Hiller, and G. Neukum, Further evidence for a mass movement origin of the Olympus Mons aureole, *J. Geophys. Res.* 87, 9917-9928, 1982.
- Lucchitta, B. K., Landslides in Valles Marineris, Mars. *J. Geophys. Res.* 84, 8097-8113, 1979.
- Lucchitta, B. K., Valles Marineris, Mars: Wet debris flows and ground ice. *Icarus*, 72, 411-429, 1987.
- Lucchitta, B. K., A. S. McEwen, G. D. Clow, P. E. Geissler, R. B. Singer, R. A. Schultz, S. W. Squyres. The canyon system on Mars, In *Mars* (H. H. Keiffer, B. M. Jakosky, C. W. Snyder, and M. S. Matthews, Eds) pp 453-492. Univ. of Arizona Press, 1992.
- Lucchitta, B. K., N. K. Isbell, A. Howington-Kraus, Topography of Valles Marineris: Implications for erosional and structural history, *J. Geophys. Res.*, 99, E2, 3783-3798, 1994.
- Malin, M. C., and M. H. Carr, Groundwater formations of martian valleys, *Nature*, 397, 589-591, 1999.
- Malin, M. C., and K. S. Edgett, Evidence for recent groundwater seepage and surface runoff on Mars, *Science*, 288, 2330-2335, 2000.
- Manning, C. E. and S. E. Ingebritsen, Permeability of the continental crust: Implications of geothermal data and metamorphic systems, *Rev. Geophys.*, 37, 127-150, 1999.
- Mars Channel Working Group, Channels and valleys on Mars, *Geol. Soc. Amer. Bull.*, 94, 1035-1054, 1983.
- Masursky, H., M. G. Chapman, A. L. Dial Jr., M. E. Strobell, Episodic channeling punctuated by volcanic flows in Mangala Valles region, Mars, in NASA TM-88383, 459-461, 1986.

- McCauley, J. F., Geological map of Coprates Quadrant Mars, *USGS Map we-897*, 1978.
- McEwen, A. S., Mobility of large rock avalanches: evidence from Valles Marineris, Mars. *Geology*, 17, 1111-1114, 1989.
- McGill, G. E., Crustal history of north central Arabia Terra, Mars, *J. Geophys. Res.*, 105, 6945-6959, 2000.
- McGovern, P. J., S. C. Solomon, D. E. Smith, M. T. Zuber, M. Simons, M. A. Wieczorek, R. J. Phillips, G. A. Neumann, O. Aharonson, J. W. Head, Localized gravity/topography admittance and correlation spectra on Mars: Implications for regional and global evolution, 107, E12, DOI 10.1029/2002JE001854, 2002.
- McGovern, P. J., J. R. Smith, J. K. Morgan and M. Bulmer, Olympus Mons Aureole deposits and basal scarp: structural characteristics and implications for flank failure scenarios, 34<sup>th</sup> LPSC, #2080, 2003.
- McKenzie, D. and F. Nimmo, Martian dikes, outflow channels and Valles Marineris, 29<sup>th</sup> LPSC, #1778, 1998.
- McSween, H. Y., and K. Keil, Mixing relationships in the martian regolith and the composition of globally homogeneous dust, *Geochim. cosmochim. acta*, 64, 2155-2166, 2000.
- Mellon, M. T., B. M. Jakosky, S. E. Postawko, The persistence of equatorial ground ice on Mars, *J. Geophys. Res.*, 102, E8, 19357-19370, 1997.
- Melosh, H. J, Acoustic fluidization: a new geologic process?, *J. Geophys. Res.*, 84, 7513-7520, 1987.
- Melosh, H. J, The mechanics of large rock avalanches, *Rev. Eng. Geol.*, 7, 41-49, 1987.
- Mischna, M. A., M. we. Richardson, R. J. Wilson, D. J. McCleese, On the orbital forcing of Martian water and CO<sub>2</sub> cycles: A general circulation model study with

- simplified volatile schemes, *J. Geophys. Res.*, 108, E6, DOI 10.1029/2003JE002051, 2003.
- Moore, J. G., Giant submarine landslides on the Hawaiian Ridge, *U. S. Geol. Surv. Prof. Pap.*, 501-D, 95-98, 1964.
- Mosangini, C. and G. Komatsu, Geomorphology of Kasei Valles and scale of flooding episodes, 29<sup>th</sup> LPSC, #1779, 1998.
- Mustard, J. F., C. D. Cooper, M. K. Rifkin, Evidence for recent climate change on Mars from the identification of youthful near-surface ground ice, *Nature*, 412, 411-414, 2001.
- Mustard, J. F., J. W. Head, M. A. Kreslavsky, R. E. Milliken, D. R. Marchant, Geological evidence for recent Martian ice ages, 6<sup>th</sup> Int. Conf. Mars, #3250, 2003.
- Nedell, S. S., S. W. Squyres, and D. W. Anderson, *Icarus*, 70, 409-441, 1987.
- Newsom, H. E., J. J. Hagerty, and F. Goff, Mixed hydrothermal fluids and the origin of the martian soil, *J. Geophys. Res.*, 104, 8717-8728, 1999.
- Norton, D., and Knight J., Transport phenomena in hydrothermal systems: cooling plutons, *Amer. J. Sci.*, 277, 937-981, 1977.
- Pariso, J. E., and H. P. Johnson, Do layer 3 rocks make a significant contribution to marine magnetic anomalies? In situ magnetization of gabbros at Ocean Drilling Program Hole 735B, *J. Geophys. Res.*, 98, 16,033-16,052, 1993.
- Parker, T. J., R. S. Saunders, and D. M. Schneeberger, Transitional morphology in west Deuteronilus Mensae, Mars: Implications for modification of the lowland/upland boundary, *Icarus*, 82, 111-145, 1989.
- Peulvast, J., D. Mège, J. Chiciak, F. Costard, and P. L. Masson, Morphology, evolution and tectonics of Valles Marineris wallslopes (Mars), *Geomorphology*, 37, 329-352, 2001.

- Phillips, R. J., M. T. Zuber, S. C. Solomon, M. P. Golombek, B. M. Jakosky, W. B. Banerdt, D. E. Smith, R. M. E. Williams, B. M. Hynek, O. Aharonson, S. A. Hauck, Ancient geodynamics and global-scale hydrology on Mars, *Science*, 291, 5513, 2587-2591, 2001.
- Purucker, M., D. Ravat, H. Frey, C. Voorhies, T. Sabaka, and M. Acuña, An altitude-normalized magnetic map of Mars and its interpretation, *Geophys. Res. Lett.*, 27, 2449-2452, 2000.
- Quaide, W. L. and V. R. Oberbeck, Development of the mare regolith: some model consideration, *The Moon*, 13, 27-55, 1973.
- Raffensperger J. P., and G. Garven, The formulation of unconformity-type uranium ore deposits 2. Coupled hydrochemical modeling, *Amer. J. Sci.*, 295, 639-696, 1995.
- Richardson, M. we. and R. J. Wilson, Investigation of the nature and stability of the Martian seasonal water cycle with a general circulation model, *J. Geophys. Res.*, 107, E5, DOI 10.1029/2001JE001536, 2002.
- Robertson, J. B., Digital modeling of radioactive and chemical waste transport in the Snake River Plain aquifer at the National Reactor Testing Station, Idaho, *Open File Rep. IDO-22054*, U.S. Geol. Surv., Reston, Va., 1974.
- Rye, R. O., P. M. Bethke, and M. D. Wasserman, The stable isotope geochemistry of acid sulfate alteration, *Econ. Geol.*, 87, 225-262, 1992.
- Saar, M. O. and M. Manga, Permeability-porosity relationship in vesicular basalts, *Geophys. Res. Let.*, 26, 111-114, 1999.
- Schubert, G., S. C. Solomon, D. L. Turcotte, M. J. Drake, and N. H. Sleep, Origin and thermal evolution of Mars in *Mars*, Univ. Ariz. Press, Tucson, 147-183, 1992.
- Scott, D. H. and K. L. Tanaka, Geologic map of the western equatorial region of Mars, *Miscellaneous Investigations Series*. U. S. Geological Survey, 1986.

- Scott, D. H. and J. M. Dohm, Evidence for multiple flooding episodes in Kasei Valles, Mars, 21<sup>st</sup> *LPSC*, p. 1115, 1990.
- Scott, D. H., and J. M. Dohm, Mars highland channels: an age reassessment, 23<sup>rd</sup> *LPSC*, 1251-1252, 1992.
- Shock, E. L., Hydrothermal systems as environments for the emergence of life, *Ciba Found. Symp.*, 202, 40-60, 1996.
- Shreve, R. L., The Blackhawk Landslide, *GSA Special Papers*, 1968.
- Skempton, A. W., Long-term stability of clay slopes, *Géotechnique*, 14, 77-102, 1964.
- Soderblom, L. A., The composition and mineralogy of the martian surface from spectroscopic observations. In *Mars* (H. H. Keiffer, B. M. Jakosky, C. W. Snyder, and M. S. Matthews, Eds) pp 557-593. Univ. of Arizona Press, 1992.
- Spinrad, H., G. Münch, and L. D. Kaplan, The detection of water vapor on Mars, *Astrophys. J.*, 137, 1319-1321, 1963.
- Squyres, S. W., Urey prize lecture - Water on Mars, *Icarus*, 79, 229-288, 1989.
- Staid, M. we., L. R. Gaddis, T. Titus, A new approach for mapping minerals on Mars with TES data, *AGU Fall Meeting*, #P42A-0553, 2001.
- Stevenson, D. J., T. Sphon, and G. Schubert, Magnetism and the thermal evolution of the terrestrial planets, *Icarus*, 54, 466-489, 1983.
- Tanaka, K. L., Ice-lubricated gravity spreading of the Olympus Mons aureole deposits, *Icarus*, 62, 191-206, 1985.
- Tanaka, K. L. and M. G. Chapman, The relation of catastrophic flooding of Mangala Valles, Mars, to faulting of Memnonia Fossae and Tharsis volcanism, *J. Geophys. Res.*, 95, 14315-14323, 1990.

- Tanaka, K. L., J. M. Dohm, J. H. Lias, and T. M. Hare, Erosional valleys in the Thaumasia region of Mars: hydrothermal and seismic origins, *J. Geophys. Res.*, 103, 31,407-31,419, 1998.
- Tanaka, K. L., J. A. Skinner, and M. G. Chapman, Mars: fluvial erosion driven by magmatism, *AGU Fall Meeting*, #P51B-03602002, 2002.
- Toksöz, M. N., A. T. Hsui, and D. H. Johnson, Thermal evolution of the terrestrial planets, *Moon Planets* 18, 281-320, 1978.
- Tóth, J., A theoretical analysis of groundwater flow in small drainage basins, *J. Geophys. Res.*, 68, 16, 4795-4812, 1963.
- Touma, J. and J. Wisdom, The chaotic obliquity of Mars, *Science*, 259, 5099, 1294-1297, 1993.
- Travis, B. J., N. D. Rosenberg, and J. N. Cuzzi, Geothermal heating, convective flow and ice thickness on Mars, *32<sup>nd</sup> LPSC*, #1390, 2001.
- Treiman, A. H., R. A. Barrett, and J. L. Gooding, Preterrestrial aqueous alteration of the Lafayette (SNC) meteorite, *Meteoritics*, 28, 86-97, 1993.
- Trunk, F. J., J. D. Dent, and T. E. Lang, Computer modelling of large rockslides, *Journal of the Geotechnical Division, ASCE* 112 (GE 3), 348-360, 1986.
- Turcotte, D. L. and G. S. Schubert, *Geodynamics*, John Wiley and Sons, New York, 1982.
- Vasavada, A. R., J. Williams, D. A. Paige, K. E. Herkenhoff, N. T. Bridges, R. Greeley, B. C. Murray, D. S. Bass, K. S. McBride, Surface properties of Mars' polar layered deposits and polar landing sites, *J. Geophys. Res.*, 105, E3, 6961-6970, 2000.
- Wang, J. H., On the frequency distribution of rupture lengths of earthquakes synthesized from a one-dimensional dynamical lattice model, *J. Physics of the Earth* 45, 363-381, 1997.

- Ward, W. R., J. A. Burns, and O. B. Toon, Past obliquity oscillations of Mars: The role of the Tharsis uplift, *J. Geophys. Res.*, **84**, B1, 243-260, 1979.
- Ward, W. R., Long-term orbital and spin dynamics of Mars, in *Mars* (H. H. Keiffer, B. M. Jakosky, C. W. Snyder, and M. S. Matthews, Eds), Univ. Arizona Press, Tuscon, 298-320, 1992.
- Wasilewski, P. J., H. H. Thomas, and M. A. Mayhew, The Moho as a magnetic boundary, *Geophys. Res. Lett.*, **6**, 541-544, 1979.
- Weitz, C. M. and T. J. Parker, New evidence that the Valles Marineris interior deposits formed in standing bodies of water, 31<sup>st</sup> LPSC, #1693, 2000.
- Wilhelms, D. E. and R. J. Baldwin, The role of igneous sills in shaping the Martian uplands, 19<sup>th</sup> LPSC, 355-365, 1989.
- Williams, R. M., R. J. Phillips, and M. C. Malin, Flow rates and duration within Kasei Valles, Mars: Implications for the formation of a Martian ocean, *Geophys. Res. Lett.*, **27**, p. 1073, 2000.
- Wilson, L. and J. W. Head, Tharsis-radial graben systems as the surface manifestation of plume-related dike intrusion complexes: Models and implications, *J. Geophys. Res.*, **107**, E8, DOI 10.1029/2001JE001593, 2002.
- Wilson, L. and P. J. Mouginiis-Mark, Phreato-magmatic dike-cryosphere interactions as the origin of small ridges north of Olympus Mons, Mars, *Icarus*, **165**, 242-252, 2003.
- Wu, S. S. C., F. J. Schafer, R. Jordan, G. M. Nakata, and J. L. Derick, Photogrammetry of Apollo 15 photography, in *Apollo 15 Preliminary Science Report* pp. 25-36 to 25-48. NASA SP-289, 1972.
- Záruba, Q. and V. Mencl, *Landslides and their control*, 2<sup>nd</sup> ed. Elsevier, Amsterdam, 1982.

Zuber, M. T., S. C. Solomon, R. J. Phillips, D. E. Smith, G. L. Tyler, O. Aharonson, G. Balmino, W. B. Banerdt, J. W. Head, C. L. Johnson, F. G. Lemoine, P. J. McGovern, G. A. Neumann, D. D. Rowlands, S. Zhong, Internal structure and early thermal evolution of Mars from Mars Global Surveyor topography and gravity, *Science*, 287, 5459, 1788-1793, 2000.

Zurek, R. W., J. R. Barnes, R. M. Haberle, J. B. Pollack, J. E. Tillman, C. B. Leovy, Dynamics of the atmosphere of Mars, in *Mars* (H. H. Keiffer, B. M. Jakosky, C. W. Snyder, and M. S. Matthews, Eds), Univ. Arizona Press, Tuscon, 835-933, 1992.